

INFORMATION TO USERS

This manuscript has been reproduced from the microfilm master. UMI films the text directly from the original or copy submitted. Thus, some thesis and dissertation copies are in typewriter face, while others may be from any type of computer printer.

The quality of this reproduction is dependent upon the quality of the copy submitted. Broken or indistinct print, colored or poor quality illustrations and photographs, print bleedthrough, substandard margins, and improper alignment can adversely affect reproduction.

In the unlikely event that the author did not send UMI a complete manuscript and there are missing pages, these will be noted. Also, if unauthorized copyright material had to be removed, a note will indicate the deletion.

Oversize materials (e.g., maps, drawings, charts) are reproduced by sectioning the original, beginning at the upper left-hand corner and continuing from left to right in equal sections with small overlaps. Each original is also photographed in one exposure and is included in reduced form at the back of the book.

Photographs included in the original manuscript have been reproduced xerographically in this copy. Higher quality 6" x 9" black and white photographic prints are available for any photographs or illustrations appearing in this copy for an additional charge. Contact UMI directly to order.

UMI

A Bell & Howell Information Company
300 North Zeeb Road, Ann Arbor MI 48106-1346 USA
313/761-4700 800/521-0600

**THE FLORIDA STATE UNIVERSITY
COLLEGE OF ARTS AND SCIENCES**

**FRAGMENTATION OF THE LOW ENERGY OCTUPOLE PHONON
IN ^{196}Pt AND INVERSE KINEMATICS PROTON SCATTERING
FROM THE RADIOACTIVE BEAM ^{20}O**

**By
J. KEITH JEWELL**

**A Dissertation submitted to the
Department of Physics
in partial fulfillment of the
requirements for the degree of
Doctor of Philosophy**

**Degree Awarded:
Fall Semester, 1997**

UMI Number: 9817316

UMI Microform 9817316
Copyright 1998, by UMI Company. All rights reserved.

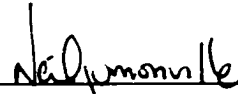
**This microform edition is protected against unauthorized
copying under Title 17, United States Code.**

UMI
300 North Zeeb Road
Ann Arbor, MI 48103

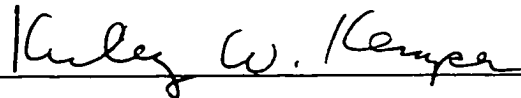
The members of the Committee approve the Dissertation of J. Keith Jewell defended on September 8, 1997.



Paul D. Cottle
Professor Directing Dissertation



Neil Jumonville
Outside Committee Member



Kirby W. Kemper
Committee Member



David Lind
Committee Member



Don Robson
Committee Member

This work is dedicated to my wife Barb, who has inspired me beyond my own expectations, and has taught me how to live fully.

ACKNOWLEDGEMENTS

Many people have contributed in various ways to this dissertation and to my graduate school experience. Regretfully, I can only acknowledge a few of them here.

First, I would like to thank my parents for their ceaseless support and encouragement in this work and everything else I've attempted.

I would like to thank Prof. Paul Cottle for serving as my advisor and mentor the last five years. He supplied me with exciting projects, showed incredible patience with my mistakes, and always looked after my best interests.

I would also like to thank Prof. Kirby Kemper for his guidance and leadership, and for his frankness in pushing me to do better. An additional thanks goes to the other members of my dissertation committee, Prof. Don Robson, Prof. David Lind and Prof. Neil Jumouville.

Thanks go to all of the people who made the experiments possible; Prof. Lewis Riley and Prof. Thomas Glasmacher, whose hard work and commitment to excellence made all the difference to our experiment at the NSCL; Powell Barber, Van Griffin, and everyone in the nuclear research machine shop and electronics rooms who had to cipher my rambling explanations of what I wanted, and then delivered it; Greg Mullens, and all the students at both FSU and MSU who selflessly spent long nights taking care of the experiments.

I would like to extend a very special thanks and my gratitude to the people who contributed not only to the work, but also to making it fun. First, I wish to thank my office mates for all the laughter and inspired conversations; Bob Kaye for all his great Storytimes; Dr. Lew Riley for his perspective on physics and life, and for his funny noises; Tim Brown, Geoff Sylvan, and Paul Cathers for enhancing my life on a daily basis. Thanks goes to all of the graduate students, past and present, who shared their time and something of themselves. I value these friendships as the best part of graduate school. Dr. Glen Johns deserves a special thanks for his late night noise and consultations, almost never about physics. Finally, I wish to thank Powell Barber for looking after me in the last few weeks, and for always thinking of the other person and never himself. He is a man worthy of emulation.

CONTENTS

| | |
|--|-------------|
| LIST OF TABLES | vii |
| LIST OF FIGURES | viii |
| ABSTRACT | xiv |
| 1 Introduction | 1 |
| 2 Theoretical Overview of Octupole States in ^{196}Pt | 10 |
| 2.1 Structure of Excited States in the $74 \leq Z \leq 80$ Mass Region | 10 |
| 2.2 Interacting Boson Model | 12 |
| 2.3 Octupole Fragmentation in the Heavy Transitional Region | 15 |
| 3 $^{196}\text{Pt}(p, p'\gamma)$ coincidence experiment | 19 |
| 3.1 Beam production | 19 |
| 3.2 Particle- γ Detection | 20 |
| 3.3 Particle- γ Electronics | 26 |
| 4 Analysis and Results of ^{196}Pt Data | 29 |
| 4.1 Previous Experimental Work on ^{196}Pt | 29 |
| 4.2 Analysis of $^{196}\text{Pt}(p, p'\gamma)$ Experiment | 37 |
| 5 Discussion of $^{196}\text{Pt}(p, p'\gamma)$ Results | 46 |
| 5.1 Octupole States in ^{196}Pt | 46 |
| 5.2 Octupole States in Other Pt Isotopes | 47 |
| 5.3 Mixed Symmetry States in ^{196}Pt | 49 |

| | | |
|-----------|--|------------|
| 6 | Theoretical Overview for $0_{g.s.}^+ \rightarrow 2_1^+$ Transition in ^{20}O | 52 |
| 6.1 | Structure of First Excited States in the $12 \leq A \leq 26$ Mass Region . . | 52 |
| 6.2 | Probe Sensitivity | 58 |
| 6.3 | Coupled Channels Calculations | 61 |
| 7 | Angular distribution measurement for ^{20}O | 64 |
| 7.1 | Beam Production | 64 |
| 7.2 | Experimental Details | 66 |
| 7.2.1 | Beam Tracking and Identification | 66 |
| 7.2.2 | FSU-MSU Charged-Particle Telescope Array | 68 |
| 7.3 | Electronics | 72 |
| 8 | Analysis and Results of $p(^{20}\text{O},p)^{20}\text{O}^*$ | 78 |
| 8.1 | Beam Tracking Correction | 78 |
| 8.2 | Proton Angular Distributions | 85 |
| 8.3 | Coupled Channels Calculations | 86 |
| 8.4 | M_n/M_p Determination | 92 |
| 9 | Discussion of ^{20}O results | 94 |
| 10 | Conclusion | 102 |
| | BIBLIOGRAPHY | 104 |
| | BIOGRAPHICAL SKETCH | 114 |

LIST OF TABLES

| | | |
|-----|--|----|
| 4.1 | Energy levels and γ -ray transitions observed in $E_p = 12.7$ MeV $^{196}\text{Pt}(p, p'\gamma)$ reaction. | 41 |
| 5.1 | Comparison of the transition strengths of the three lowest energy 3^- states in ^{196}Pt from (p, p') and (e, e') | 49 |
| 6.1 | Ratios of neutron to proton sensitivity of various probes. [Ber81] . . . | 60 |
| 8.1 | Optical model parameters for ^{20}Ne and ^{20}O | 91 |

LIST OF FIGURES

| | | |
|-----|---|----|
| 2.1 | Octupole state strength distribution. (a) ^{194}Pt modeled as an $O(6)$ nucleus, (b) ^{146}Nd modeled as a $U(5)$ nucleus, and (c) ^{168}Er modeled as an $SU(3)$ nucleus. Of the three idealized symmetries, only the $O(6)$ symmetry can reproduce the significant octupole strength in higher-lying 3^- states in the IBM-1 formalism. | 18 |
| 3.1 | Schematic of the $^{196}\text{Pt}(p, p'\gamma)$ experimental apparatus. | 22 |
| 3.2 | The TAC timing spectrum and gated particle projections. (a) The time spectrum is the total yield as a function of the time difference between a particle and γ -ray event. A peak from the prompt coincidences sits above a continuum of “chance coincidence” background. (b) Projected proton spectrum before any software gating. The first excited state is seen as a shoulder of the elastic proton peak. (c) Projected proton spectrum with the chance coincidences subtracted. The elastic peak is nearly completely suppressed, and the spectrum is dominated by the first excited state. | 25 |
| 3.3 | Diagram of the electronics. Both the signal and logic electronics are included. | 28 |
| 4.1 | Energy systematics of the 3_1^- states in the heavy transitional mass region ($74 \leq Z \leq 82$). The energies of the lowest octupole state in Hg and Pb are nearly constant around 2.6 MeV. In the Pt and Os isotopes, however, (shown respectively as triangles and inverted triangles) the energy of the lowest octupole state is nearly 1 MeV lower. | 30 |

| | | |
|-----|---|----|
| 4.2 | Energies of the low energy octupole state in the heavy transitional region. The open shapes indicate the centroid energy of the low energy octupole state, while the closed shapes are the 3_1^- state energies. | 32 |
| 4.3 | The magnitude of fragmentation is plotted against $R_{4/2}$, a structural indicator of the degree of static quadrupole deformation. The degree of fragmentation seen for the Pt isotopes is greater than that of even the most statically deformed examples of nuclei. | 34 |
| 4.4 | Proton angular distributions compared to coupled channels calculations. The similarity between 3^- and 4^+ states makes impossible an unambiguous spin assignment based on the proton angular distributions alone. | 36 |
| 4.5 | The proposed octupole candidate states in ^{196}Pt . γ -ray angular distributions allow for a $J^\pi = 3^-$ spin assignment for each state. Additionally, each state energy is, within error, consistent with one of the proposed octupole states seen in (p, p') | 38 |
| 4.6 | Abbreviated energy level decay scheme showing the states populated in the present $^{196}\text{Pt}(p, p'\gamma)$ experiment. | 40 |
| 4.7 | (a) γ -ray spectrum showing the 2245 keV γ -ray decay to the ground state and (b) the proton spectrum showing a peak from the 2245 keV state. | 43 |
| 4.8 | (a) γ -ray and (b) proton spectra showing the previously reported decay from the 2423 keV state by a 2067.6 keV γ -ray. | 44 |
| 4.9 | (a) γ -ray and (b) proton spectra showing the previously unreported decay from the 2423 keV state by a 976.7 keV γ -ray to the 3_1^- state. The subsequent decays from the 3_1^- state are also shown. | 45 |
| 6.1 | Typical energy level spacings from vibrational and rotational collective behavior | 54 |

| | | |
|-----|--|----|
| 6.2 | Known energy levels in ^{20}O | 55 |
| 7.1 | The layout of the NSCL experimental facility. The figure shows the K1200 cyclotron where the primary beam is accelerated, the A1200 mass fragment separator for production and selection of the radioactive secondary beam, and the S2 experimental vault at the tail end of the RPMS fragment separator where the $p(^{20}\text{O},p)^{20}\text{O}$ scattering experiment was performed. | 65 |
| 7.2 | A1200 mass fragment separator at the NSCL. The A1200 is used to identify and select secondary beams after fragmentation of the primary beam. | 66 |
| 7.3 | Schematic of the experimental arrangement. | 67 |
| 7.4 | Sample $\Delta E - E$ and TOF zero degree detector spectra showing the high purity of the beam. The top plot is the energy loss in the fast plastic versus the energy in the slow plastic. Only a single isotope (^{20}O) can be seen. The bottom plot is the beam TOF between the A1200 exit and the zero degree detector. The spreading of the characteristic energy loss point is caused by an unstable power supply producing fluctuations in the detector bias voltage | 69 |
| 7.5 | Positioning of the FSU-MSU charged particle telescope array. Each telescope is a three stage detector consisting of a position sensitive Si strip detector, a PIN diode, and a CsI scintillator. Telescopes 1,2 and 3, on the left side, are centered at 75° with respect to the beam axis, and telescope 4 is at 60.5° . On the right, telescopes 5,6 and 7 are centered at 70° , and telescope 8 is at 84.5° | 71 |

| | | |
|-----|--|----|
| 7.6 | Electronics diagram for the beam detectors. Electronics for PPACs 1 and 2 were identical. Gates and time starts were generated by the master electronics shown in Figure 7.8 and are not included explicitly here. | 75 |
| 7.7 | Electronics diagram for a single particle telescope. Gates and time starts were generated by the master electronics shown in Figure 7.8 and are not included explicitly here. | 76 |
| 7.8 | Diagram of the master electronics which generated event triggers and gates. The boxed number in the coincidence logic units indicates the coincidence level required between the two inputs labeled A and B. | 77 |
| 8.1 | The trajectory tracking of an arbitrary proton scattering event. The incoming beam particle with trajectory \vec{r}_{beam} is detected by the position sensitive PPACs at positions \vec{r}_1 and \vec{r}_2 and interacts with a proton in the target at position \vec{r}_{int} . The scattered proton trajectory \vec{r}_{scat} is at an angle θ_0 with respect to the optical axis and an angle θ_{scat} , the proton laboratory scattering angle, with respect to the incoming beam trajectory. For simplicity, the target is shown perpendicular to the incident beam direction. | 79 |
| 8.2 | Examples of beam tracking spectra show two dimensional position spectra for the beam measured at (a) PPAC 1 and (b) PPAC 2, (c) the projected transverse position, and (d) the z position spectra on target. | 82 |
| 8.3 | Angular correction spectra for (a) telescopes 1,2 and 3 and (b) telescopes 5,6 and 7 show the large correction needed for telescopes 1,2, and 3. The angular resolution for telescopes 5, 6, and 7, however, is on the order of the intrinsic strip width. | 83 |

| | | |
|-----|--|----|
| 8.4 | Proton laboratory kinetic energy versus scattering angle plots from telescopes 1, 2 and 3 (a) without and (b) with the beam tracking correction, illustrating the need for a scattering angle correction in order to separate the elastic and inelastic events | 84 |
| 8.5 | Comparison of actual data and calculated kinematics. (a) The collected proton scattering data displayed on the same scale as the calculated kinematics in (b). The dashed box indicates the identified inelastic events. (b) Calculated kinematic curves of energy as a function of scattering angle in the laboratory frame. The solid box shows the field of view of the telescopes. The dashed lines show the punch through energies for a proton penetrating into the next stage of the telescope. | 87 |
| 8.6 | Summed proton laboratory kinematics spectra from (a) strip 4 of telescopes 1, 2 and 3 and (b) strip 4 of telescopes 5, 6 and 7. Spectra of this kind were used in summing the cross sections to generate the angular distribution. | 88 |
| 8.7 | Angular distributions of protons scattered from the ground state and 2_1^+ state of ^{20}O . The smooth curves are coupled channel calculations using known optical model parameters from ^{20}Ne and the RMS quadrupole deformation β_2 giving the best reproduction of the inelastic cross section. | 89 |
| 9.1 | Ratios of $(M_n/M_p)/(N/Z)$ for $0_{gs}^+ \rightarrow 2_1^+$ transitions in the $12 \leq A \leq 26$ mass region. The values are extracted from comparisons of proton scattering [DeL83, Gra80, Ril:diss, deS74, Has83, Zwi83], neutron scattering [Gra80, Ols89, Ols90], and electromagnetic [Ram87] measurements. | 95 |

9.2 $(M_n/M_p)/(N/Z)$ ratios for the $0_{gs}^+ \rightarrow 2_1^+$ transitions in the $12 \leq A \leq 26$ mass region. The results from pion scattering are compared to those from nucleon scattering and electromagnetic results. The dashed lines are shell model predictions from [Bro82]. 97

ABSTRACT

The results from two separate proton scattering experiments are presented. First, we present positive identification of a $J^\pi = 3^-$ state at 2423.4(4) keV in ^{196}Pt from a $^{196}\text{Pt}(p, p'\gamma)$ reaction at 12.7 MeV performed at Florida State University. The identification, based on known proton and γ -ray angular distributions, indicates that the low energy octupole state is fragmented between at least two states. Octupole fragmentation in ^{196}Pt is discussed in terms of the $O(6)$ symmetry of the IBM. Second, we present angular distributions of protons scattered from the ground state and 2_1^+ state of the singly closed shell nucleus ^{20}O , measured in inverse kinematics at 30 MeV/A at the National Superconducting Cyclotron Laboratory. We extract the effective RMS quadrupole deformation parameter β_2 for proton scattering by comparison with a coupled channels calculation. The known electromagnetic $B(E2; 0_{gs}^+ \rightarrow 2_1^+)$ is used in conjunction with our deduction of β_2 from proton scattering to extract a ratio of neutron to proton multipole matrix elements $M_n/M_p = 2.8 \pm 0.40$ for the $0_{gs}^+ \rightarrow 2_1^+$ transition. The present value of M_n/M_p indicates a large neutron contribution to the 2_1^+ state excitation due to the closed $Z = 8$ proton shell.

CHAPTER 1

INTRODUCTION

The low energy behavior of nuclei can be categorized, in the most basic way, as either single-particle-like or collective. The single-particle description is strongly related to a shell model formalism reminiscent of descriptions applied to electron behavior in atomic systems. The emphasis of the shell model is on discrete orbits or angular momentum states successively filled by individual nucleons. The simple collective description, in contrast, relates a many-body nuclear system to a classical liquid drop shape without specifying the behavior of single nucleons. Collective models are most useful in describing the overall shape of the nucleus, and time dependent deviations from that equilibrium shape. There are not, however, clear and sharp distinctions between collective and single-particle behavior. It is now understood that most nuclei exhibit both types of behavior to varying degrees. Purely collective or single-particle descriptions represent only the extremes of a continuous variety of nuclear behavior.

The shell model description was first to gain wide acceptance in the scientific community for a number of reasons. Existing shell model descriptions of electrons in atomic systems made a parallel development for nuclear systems quite attractive. Early experimental evidence also indicated that a shell model gave a valid description of many nuclear properties. The existence of strongly peaked isotopic abundances of nuclei clustered about specific nucleon numbers and large jumps seen in nucleon separation energies pointed to an underlying shell structure for nucleons. This experimental evidence hinted at the existence of "magic" numbers, which are indicative of completely filled nuclear shells. By introducing

a strong spin-orbit coupling to a simple harmonic oscillator potential, we obtain the shell structure used today, having magic numbers at 2, 8, 20, 40, 50, 82, and 126 [Fee49, Hax49, May49, May50, Jen52, May55].

Measurements of neutron capture cross sections and quadrupole moments lent further confidence in the shell model description [May48]. Early forms of the shell model were successful in explaining spins and parities of ground states in many nuclei within a few nucleons of the magic numbers [Hax49, May55]. Lastly, the shell model gained acceptance because early experimental studies focused on light nuclei, for which the shell model is more easily applied. Since many studies of nuclei often require probing the nucleus above the Coulomb barrier, advanced accelerator technology was needed to deliver beams of sufficient energy to study some of the heavier nuclei.

As more experimental evidence became available, however, the shell model could not reproduce the properties of nuclei away from the magic numbers. Nuclei residing far away from closed shells exhibited behavior which could not be easily explained by a nuclear shell structure. The most striking evidence that the shell model was an incomplete picture came from study of electric quadrupole moments in nuclei away from closed shells. The electric quadrupole moment is a measure of the quadrupole deviation of the nuclear charge distribution from a spherical shape. It was observed that the electric quadrupole moments for nuclei between closed shells had values much larger than those possible from shell model configurations [Tow49, Gor49]. The discovery of the giant dipole collective mode, where the protons and neutrons oscillate against one another about the center of mass, greatly motivated further development of collective models.

The first collective descriptions of nuclei modeled the nuclear matter as a classical liquid drop possessing surface deformations from a spherical shape. The simplistic liquid drop model had been developed prior to much of the experimental indications

for collective nuclear behavior as a need to explain the process of nuclear fission. Bohr and Wheeler [Boh39], expanding on ideas of Weizsacker [Wei35], studied shape stability of charged liquid drops deformed from a spherical equilibrium shape. The surface of an arbitrarily deformed liquid drop shape can be constructed by an expansion of spherical harmonics as

$$R(\theta, \phi) = R_0[1 + \sum_{lm} \alpha_{lm} Y_{lm}(\theta, \phi)] \quad (1.1)$$

where R_0 is the mean radius, α_{lm} are deformation parameters, and Y_{lm} are spherical harmonics. This straightforward, but useful description of deformed nuclear shapes makes an explicit connection to the importance of multipole orders. Since the nuclear matter is fairly incompressible, the monopole moment, which represents a compressive “breathing” mode of the nucleus, occurs only at high energies. At modest values of α_{lm} , the dipole mode is also somewhat trivial, arising from a translation of the nucleus as a whole without a change in the intrinsic nuclear shape. The important leading term in describing collective motion at low energies is, therefore, the quadrupole moment.

Because the quadrupole degree of freedom is the dominant excitation mode at low energy throughout the Periodic Table, most of the various collective pictures have concentrated exclusively on this mode. Although octupole and hexadecapole degrees of freedom have been shown to contribute to the overall stable nuclear shape [Hen68, But96], their contributions are typically much smaller than the dominant quadrupole contribution. Deformation modes of any multipole order are allowed by the expansion given previously in Equation 1.1.

The earliest shell models, too, have been modified and expanded to account for collective behavior. The great success of the shell model in describing the behavior of spherical nuclei near the magic numbers, and the knowledge of collective behavior away from closed shells, led to the development of a deformed shell model. Nilsson’s deformed shell model [Nil55] has been widely used with great success in predicting

the ground state spins and parities of many nuclei away from closed shells. It has been particularly useful in describing odd mass nuclei, and its importance can not be overstated.

In the mid-1970's, however, a different approach to describing collective motion was developed. The model, known as the Interacting Boson Model (IBM), is developed from the algebraic properties of the dynamical symmetries of the nucleus [Ari75, Ari76, Ari78, Ari79]. The IBM treats pairs of nucleons coupled to specific angular momentum states as integer spin bosons, and has been useful in describing a wide variety of collective phenomena.

The wide variety of collective behavior is due, in part, to the wide variety of shapes that nuclei can possess. Shape deformations of the nucleus can be either static or dynamic. The simplest example of the excitation of a statically deformed nucleus is rotational behavior. The statically deformed nucleus can be viewed as a classical rigid rotor with energy levels spaced according to a $J(J + 1)/2I$ rule, where J is the total angular momentum and I is the classical moment of inertia. In contrast, a vibrational excitation is characterized by an energy spectrum which, in the harmonic limit, has a series of equally spaced and degenerate multiplets. The most commonly observed vibrational mode is the quadrupole mode. However, higher order vibrational modes can be excited as well. Octupole vibrations, a $J = 3$ multipole order carrying $3\hbar$ units of angular momentum and hexadecapole ($J = 4$) vibrations are found throughout the Periodic Table.

The most commonly observed form of vibrational collectivity is the electric quadrupole excitation [Sch55]. The most obvious signatures of low energy quadrupole vibrations are large transition strengths between energy levels which are nearly evenly spaced, and the presence of nearly degenerate multiplets which are evenly spaced and correspond to multi-phonon excitations. Rainwater [Rai50] asserted in 1950 that single valence nucleons outside of a closed shell could polarize

the closed shell core and lead to oscillatory vibrations. New collective degrees of freedom were described by Bohr and Mottelson [Boh52, Boh53, Boh75] which led to the discovery of other vibrational multipoles. Octupole vibrations, evidenced by low energy $J^\pi = 3^-$ states, and coupling between quadrupole and octupole degrees of freedom, evidenced by low energy $J^\pi = 1^-$ states, were found soon after their important work [Ste54, Nat56, Ken56].

A main focus of experimental curiosity is to examine anomalous behavior in nuclei. Nuclei which exhibit unusual or unexpected behavior allow nuclear structure models to be advanced beyond their simplest forms. Ideally, any useful model will describe many different types of behavior over a wide mass range of nuclei. It is the observed behavior at the very edge of a model's capability which motivates careful modification and adaptation of the model itself.

The present work investigates two different examples of anomalous collective behavior in two different mass regions. The first example is seen in the $74 \leq Z \leq 80$ mass region. This mass region is known informally as the heavy transitional region due to a shape transition around $A \approx 192$ from prolate to oblate shape, and then to spherical at $Z = 82$. Nuclei in the heavy transitional region exhibit a wide range of shapes, from near spherical for the Pb and Hg isotopes with $A \approx 208$, to well-deformed shapes farther from the closed shells. While both the spherical shape and the well-deformed shapes have been well described by the shell model and collective models respectively, the transition region between the two shapes is less understood. This is due, in part, to the excitations being a complex coupling of rotational, vibrational, and single-particle degrees of freedom.

In fact, even some of the pure vibrational modes in this mass region have not been adequately described thus far. In particular, the octupole vibrational mode in the heavy transitional region shows unexpected behavior which warrants the investigation in the present work. In other mass regions, the systematic behavior of

the low energy octupole state is typically smooth as the nucleus undergoes a gradual shape change. The energies of the octupole states vary only slightly from nucleus to nucleus. In contrast to the smooth behavior seen in other mass regions, the energies of the octupole states in the heavy transitional region show abrupt changes.

The second example of anomalous behavior investigated in the present work involves differences between the proton and neutron contributions to a quadrupole vibrational excitation in the $12 \leq A \leq 26$ mass region. Some background of early investigations of proton and neutron differences is necessary here. The Giant Dipole Resonance (GDR) is the earliest example of behavior for which proton and neutron motions are not identical. The GDR is a high energy (≥ 15 MeV) collective excitation. In this mode of excitation, the neutrons and protons oscillate against each other about the center of mass of the nucleus. Since the protons constitute the charge carriers of the nucleus, the GDR is seen as a strong oscillation of charge with respect to the center of mass which gives rise to a large dipole (E1) transition when the mode is excited by electromagnetic probes. Several theories were quickly developed upon discovery of the GDR, the most successful of which were from Goldhaber and Teller [Gol48], Steinwedel [Ste50], and Danos [Dan51]. The various theories formulated the now well known $A^{-1/3}$ energy dependence of the GDR, and later extensions of the theory predicted a splitting of the resonance due to the deformation of the nucleus [Oka58, Dan58]. While the GDR is a high energy collective excitation, and this work is primarily concerned with low energy collective excitations, the GDR is an excellent example of anomalous behavior which prompted further theoretical development.

The GDR also suggests that protons and neutrons can behave differently from one another in a collective motion. That is, the nuclear force can have an "isospin" component. Heisenberg suggested that the proton and the neutron could be treated as two states of the nucleon [Hei32]. Neutrons and protons could then be dis-

tinguished by the projection of the isospin vector T_z onto an arbitrarily assigned symmetry axis. With the isospin component added to transition operators between nuclear states, differences in proton and neutron behavior can be quantified on the basis of a non-vanishing isovector component of the transition. Any isovector magnitude is usually treated independently of the known Coulomb charge dependence, which is the dominant isospin symmetry breaking term.

A wonderful test of isospin symmetry is found in the first excited states of even-even closed shell nuclei in the $12 \leq A \leq 26$ mass region. The 2_1^+ states of even-even nuclei in this mass region are often thought of as collective, isoscalar excitations. It has been shown, however, that differences between the proton and neutron contributions can occur in $0_{g.s.}^+ \rightarrow 2_1^+$ transitions, especially in single closed shell nuclei [Ber83, Ken92].

A comparison of the neutron and proton oscillation magnitudes can be done by comparing the $B(E2; 2_1^+ \rightarrow 0_{g.s.}^+)$ reduced transition matrix element from two different experimental probes. Madsen *et al.* [Mad75] have stated that a useful comparison of proton and neutron matrix elements can be carried out with low energy (10-50 MeV) proton scattering to measure the neutron contribution, and electromagnetic transitions to measure the proton contribution. While the electromagnetic probe is sensitive to the charge (proton) distribution only, other probes have varying degrees of neutron to proton sensitivity [Ber81]. The neutron and proton contributions to an excited state can be separated, therefore, by using two or more experimental probes.

A particularly useful way of expressing the difference in neutron and proton contributions to the $0_{g.s.}^+ \rightarrow 2_1^+$ transition is by the ratio of the neutron and proton multipole matrix elements M_n/M_p . The transition matrix element for protons (neutrons) between initial and final states is given by

$$M_{p(n)}(T_z) = \langle \nu_f J_f T_f T_z A || O_{p(n)}^\lambda || \nu_i J_i T_i T_z A \rangle \quad (1.2)$$

where $O_{p(n)}^\lambda$ is the multipole transition operator for a transition of order λ for protons (neutrons), J is total angular momentum, T is the isospin with projection $T_Z = \frac{1}{2}(Z - N)$, and ν is a generic representation of additional quantum numbers needed to specify the state. For purely isoscalar transitions ($\Delta T = 0$), the neutrons and protons oscillate at the same amplitude, and $M_n/M_p = N/Z$. Deviations result from a non-vanishing isovector contribution to the transition.

A major focus of the present work is to provide further information about the systematics of proton and neutron contributions to low-lying quadrupole excitations in even-even nuclei by a study of the unstable nucleus ^{20}O . Until recently, the study of nuclei outside the valley of stability using scattering reactions such as (p, p') was not feasible. With recent advances in radioactive beam production and techniques for measuring proton scattering in inverse kinematics, the possibility of studying the more than 3000 particle stable nuclei has been opened to us. Measurements from these least stable nuclei provide stringent tests of any nuclear model, whether collective or single-particle in character.

The present work presents two separate and distinct studies of collective behavior motivated by anomalous systematics. The first study will detail a $^{196}\text{Pt}(p, p'\gamma)$ coincidence experiment performed at Florida State University which populated a second octupole state containing a significant amount of the octupole phonon strength. The $J^\pi = 3_2^-$ spin assignment given to this state relies on previous proton angular distributions limiting the spin to $J^\pi = 3^-$ or 4^+ [Cot88b] and previous γ -ray angular distributions consistent with a $J^\pi = 3^-$ assignment [DiP93].

The second major focus of the present work offers results from a proton scattering experiment in inverse kinematics from the radioactive beam ^{20}O performed at the National Superconducting Cyclotron Laboratory. The proton angular distribution is used to extract an effective quadrupole deformation parameter β_2 , which, in conjunction with the known $B(E2; 0_{g.s.} \rightarrow 2_1^+)$ electromagnetic measurement

[Ram87, Til95], yields a value of $M_n/M_p = 2.8 \pm 0.4$. The result is much larger than N/Z , which is expected for an isoscalar transition, and clearly indicates an enhanced neutron contribution to the transition.

Chapter 2 of the present work is a theoretical overview of octupole excitations in the heavy transitional mass region. Experimental details of the $^{196}\text{Pt}(p, p'\gamma)$ coincidence experiment are given in Chapter 3, followed by results from the experiment and a discussion of the results in Chapters 4 and 5. Chapter 6 is a theoretical overview of 2_1^+ states in the $12 \leq A \leq 26$ mass region. Chapter 7 presents the experimental details of the inverse kinematics $p(^{20}\text{O}, p)^{20}\text{O}^*$ proton scattering experiment. The analysis and results from the experiment are given in Chapter 8, followed by a discussion of the results in the context of systematics of the mass region in Chapter 9. Chapter 10 will then provide a brief summary of the major points from both experiments.

CHAPTER 2

THEORETICAL OVERVIEW OF OCTUPOLE STATES IN ^{196}Pt

Nuclear structure is typically studied within the context of two major frameworks: the shell model and the collective model. As was mentioned in Chapter 1, the bulk of nuclear behavior exhibits properties of both of these two idealized pictures.

2.1 Structure of Excited States in $74 \leq Z \leq 80$ Mass Region

In the shell model, nucleons in an even-even nucleus in the ground state successively fill nuclear orbitals of lowest available energy. In a $j - j$ coupling scheme, pairs of like nucleons couple to zero orbital angular momentum states. Each angular momentum state j is split by coupling to the magnetic moment of the nucleon into a series of magnetic substates $m = -j, -j + 1, \dots, j - 1, j$. Each m substate contains one nucleon, and substates of opposite m sign couple to zero, giving an overall contribution of zero to the angular momentum of the entire nucleus. Excited states are built by successively promoting nucleons from the ground state configuration to other shells. The angular momentum of the excited state results from the coupling of the excited nucleons with each other and the “holes” left behind in the ground state configuration.

The collective treatment, by contrast, makes no explicit reference to individual nucleon orbits. Instead, eigenstates are built from linear combinations of spherical harmonics which describe the radius of the nuclear surface, as in Equation 1.1, by multipole order. Collective excitations are generally identified by transition

strengths which are considerably larger than those which occur in single-particle transitions. Since the large transition strengths are many times those obtainable with single-particle excitations, we can consider the collective excitation to be a coherent sum of single-particle excitations [Bro59]. The transition probability for an electric transition of multipole order λ between two states is related to the reduced transition probability, $B(E\lambda; i \rightarrow f)$, by

$$T(E\lambda) = \alpha c \frac{8\pi(\lambda + 1)}{\lambda[(2\lambda + 1)!!]^2} \left(\frac{E_\gamma}{\hbar c}\right)^{2\lambda+1} B(E\lambda; i \rightarrow f) \quad (2.1)$$

with the energy difference between the initial and final states given by E_γ . $B(E\lambda)$ relates to the full transition matrix elements by

$$\begin{aligned} B(E\lambda; i \rightarrow f) &= \sum_{\mu M_f} |\langle \nu_f J_f M_f | O_{\lambda\mu}^E | \nu_i J_i M_i \rangle|^2 \\ &= \frac{1}{2J + 1} |\langle \nu_f J_f || O_\lambda^E || \nu_i J_i \rangle|^2, \end{aligned} \quad (2.2)$$

where the ν indicates additional quantum numbers needed to uniquely determine the state, and $O_{\lambda\mu}^E$ is the electric multipole operator given by

$$O_{\lambda\mu}^E = \sum_i r_i^\lambda Y_{\lambda\mu}(\hat{r}_i). \quad (2.3)$$

The Weisskopf unit (W.u.) single-particle estimate [Bla79], is commonly used to quantify the strength of a transition independently of the size of the nucleus. This is done by considering the transition probability of multipole order λ of a single nucleon moving from one single-particle orbit to another. In this extreme independent-particle picture, the transition of a single particle is assumed to occur without affecting any other nucleons. The single-particle estimate can be obtained from the transition operator by evaluating the average value of r^λ by

$$\langle r^\lambda \rangle = \int_0^\infty R_f^* r^\lambda R_i r^2 dr \quad (2.4)$$

where R_f^* and R_i are the normalized radial parts respectively of the final and initial single-particle wavefunctions. Approximating the nucleus as a uniformly dense sphere with radius $R = r_o^\lambda A^{\frac{\lambda}{3}}$ fm reduces the the radial integral to

$$\int_0^\infty R_f^* r^\lambda R_i r^2 dr \approx \frac{3}{\lambda + 3} r_o^\lambda A^{\frac{\lambda}{3}}. \quad (2.5)$$

The Weisskopf single-particle estimate for electric transitions is then given by

$$B_W(E\lambda) = \frac{1}{4\pi} \left(\frac{3}{\lambda + 3} \right)^2 r_o^{2\lambda} A^{2\lambda/3} e^2 fm^{2\lambda}. \quad (2.6)$$

2.2 Interacting Boson Model

The behavior of the octupole states in the even-even Pt isotopes has been discussed in the framework of the Interacting Boson Model (IBM) [Zam93a], the Quasiparticle-Phonon Model (QPM) [Pon92], and Hartree-Fock formalisms [Egi96]. Only the IBM and QPM approaches, however, have been successful in explaining fragmentation of the octupole strength.

Until the mid-1970s, descriptions of collective behavior were generally given in the Bohr and Mottelson geometric picture. An alternate method of describing collective behavior, the IBM, was introduced by Arima and Iachello in 1974 [Iac74, Ari75], and is algebraic in its formalism. The IBM is an attempt at truncating the shell model basis space which quickly becomes too large to be useful in describing the behavior of heavy nuclei. The IBM treats valence nucleons in pairs as bosons which couple to particular integer spins. Low-lying collective behavior is then described in terms of the energies and interactions of these nucleon pairs. The truncation of the shell model space results from allowing only a limited number of angular momentum values J to which a pair of nucleons can couple. For example, if momentum couplings of only $J = 0$ (s bosons) and $J = 2$ (d bosons) are allowed, the number of magnetic substates is limited to six (1 from $J = 0$, 5 from $J = 2$), and basis states

span a six dimensional space. The allowed angular momentum couplings constitute a system which can be described in terms of its $U(6)$ algebraic group properties.

The $U(6)$ group can be decomposed into subgroups by way of three decomposition chains which are physically meaningful. That is, the three chains decompose to an $O(3)$ symmetry which is required for invariance under rotation. Each of the three chains has a geometric analog associated with it. Consequently, the three group chains define the limiting cases of collective behavior associated with the quadrupole degree of freedom in the IBM picture. The $U(5)$ symmetry is the IBM equivalent of a spherical vibrator. $SU(3)$ symmetry corresponds to an axially symmetric rigid rotor deformation commonly associated with rotational collective motion. The $O(6)$ symmetry, which is the primary concern of this section, corresponds to a γ -unstable, axially-asymmetric rotor [Ciz78, Cas78, Bol81].

Some rather bold and drastic assumptions are made in the IBM. Valence nucleons make the primary contribution to the excitation, and excitations from nucleons in closed shells are taken into account by means of effective charges in the transition operators. Additionally, no distinction is made between protons and neutrons, in the earliest version of the model (IBM-1), nor is there a distinction between particles and holes. Valence nucleons are counted from the closest closed shell. Some of these restrictions to the model are removed in advanced forms of the IBM (IBM-2 and IBM-3). Casten and Warner provide an excellent review of the IBM formalism [War82]. The present work will be concerned only with the usage of the IBM in understanding octupole behavior. Some background is necessary here, though, to make this possible.

The IBM features a Hamiltonian containing operators for the creation and annihilation of the bosons needed to construct the excitations of interest. A generic operator is written in the spherical tensor form used by Barfield *et al.* [Bar88] $\bar{b}_{\mu}^{(\lambda)} = (-1)^{(\lambda+\mu)} b_{-\mu}^{(\lambda)}$. In the simple case of a harmonic oscillator, for example, the

Hamiltonian is given by

$$H = \epsilon_d(d^\dagger \tilde{d}) = \epsilon_d n_d \quad (2.7)$$

where ϵ_d is the energy of a d ($J=2$) boson, and d^\dagger and d are the creation and annihilation operators respectively of a d boson. The energy of the excitation is then just the intrinsic energy of the d boson multiplied by the number n_d of d bosons needed to create the excitation.

In order to describe octupole excitations, however, the addition of an f ($J=3$) negative parity boson is required. A suitable Hamiltonian for describing a number N_B of bosons in an $(sd)^{N_B-x} f^x$ $O(6)$ basis, where $x = 0$ or 1 , is given by

$$H = H_{sd} + H_f + V_{sdf}. \quad (2.8)$$

This choice of basis allows for, at most, a single f boson. The first term of the Hamiltonian, H_{sd} , describes the even-even positive parity (sd) core upon which the negative parity excitations are built, described by H_f . The final term, V_{sdf} , is a two-body interaction between the positive and negative parity bosons. The positive parity core term consists of pure d boson operators, L_d , and a mixing operator between s and d bosons, Q_d , in the form

$$H_{sd} = \epsilon n_d + a_1 L_d \bullet L_d - a_2 Q_d \bullet Q_d, \quad (2.9)$$

where $n_d = d^\dagger d$ is the d boson number operator and

$$L_d = \sqrt{10}(d^\dagger \tilde{d})^{(1)} \quad (2.10)$$

$$Q_d = (s^\dagger \tilde{d} + d^\dagger s) + \chi_2 (d^\dagger \tilde{d})^{(2)}. \quad (2.11)$$

The transition from $O(6) \rightarrow SU(3)$ symmetries is obtained by varying the free parameter χ_2 from $\chi_2 = 0$ (the ideal $O(6)$ limit) to $\chi_2 = -1.32$ (the $SU(3)$ limit). The f boson excitations are handled by a simple

$$H_f = \epsilon_f n_f \quad (2.12)$$

where $n_f = f^\dagger \tilde{f}$, the f boson number operator, equals zero for positive parity excitations and one for negative parity excitations in this choice of basis which is limited to a single f boson. The interaction between the positive parity core and the f boson system is considered as a multipole expansion of the form

$$V_{sdf} = A_1 L_d \bullet L_f + A_2 Q_d \bullet Q_f + A_3 : E_{df}^\dagger \bullet E_{df} : \quad (2.13)$$

with

$$L_f = 2\sqrt{7}(f^\dagger \tilde{f})^{(1)} \quad (2.14)$$

$$Q_f = -2\sqrt{7}(f^\dagger \tilde{f})^{(2)} \quad (2.15)$$

$$: E_{df}^\dagger \bullet E_{df} : = 5 : (d^\dagger \tilde{f})^{(3)} \bullet (f^\dagger \tilde{d})^{(3)}. \quad (2.16)$$

The $: E_{df}^\dagger \bullet E_{df} :$ term is an “exchange” term composed of a linear combination of five multipole terms, and is added for phenomenological reasons [Bar88].

2.3 Octupole Fragmentation in the Heavy Transitional Region

It has long been known that the low energy octupole state is fragmented in well deformed nuclei, such as those in the rare earth and actinide regions [Nee70, Cot96]. In the case of nuclei with large static quadrupole deformations, the octupole mode aligns along different K quantum number components with respect to the symmetry axis having $K = 0, 1, 2,$ and 3 . The Pt isotopes of the heavy transitional region, however, do not have large, stable deformations, having $\beta_2 \leq 0.15$. The high degree of fragmentation observed in the Pt isotopes can not be explained simply by different K alignments.

As early as 1986 Engel [Eng86] predicted fragmentation of the low energy octupole state in the Pt isotopes. Zamfir *et al.* [Zam93a] further demonstrated that octupole fragmentation would occur in nuclei which conform to the O(6) dynamical

symmetry, of which ^{196}Pt is the best known example [Ciz78]. Zamfir *et al.* summarized two different situations where octupole fragmentation is likely to occur in the IBM formalism. The first is seen in nuclei having a large static quadrupole deformation. The nuclei in this category correspond to the usual picture where large fragmentation is expected, and are interpreted in the IBM as a transition from $U(5)$ to $SU(3)$ symmetry. The other situation where large octupole fragmentation is expected is for nuclei conforming to an $O(6)$ symmetry, such as the Pt isotopes. As mentioned previously, $O(6)$ nuclei have γ -soft, axially asymmetric shapes and do not have large static deformations [Ciz78, Cas78, Bol81]. It has even been proposed that the existence of octupole fragmentation can provide a signature for $O(6)$ nuclei [Zam93a].

The calculations of Zamfir *et al.* [Zam93a, Zam93b] show that a high degree of fragmentation of the low energy octupole state is expected for the even-even Pt isotopes. In their analysis, a large concentration of octupole strength is found nearly 1 MeV above the 3_1^- state. Distributions of octupole strength from their calculations are given in Figure 2.1 and show the additional strength contained in higher-lying octupole states. The example used in the figure is from ^{194}Pt , but nearly identical results are obtained for $^{196,198}\text{Pt}$ as well. Zamfir *et al.* also demonstrate that the large degree of fragmentation observed in the Pt isotopes cannot be reproduced by modeling the region as a $U(5) \rightarrow SU(3)$ transition region. Only by modeling the region with an $O(6)$ symmetry are they able to reproduce the experimentally observed magnitude of the octupole fragmentation in the IBM-1 formalism.

Zamfir *et al.* made additional simplifications to the IBM Hamiltonian of Equation 2.8 in calculating octupole fragmentation for a wide range of nuclei [Zam93a]. In particular, ϵ_f , the overall excitation energy of the negative parity states, is set to unity. Both a_1 of Equation 2.9 and A_1 of Equation 2.13 are set to zero because the $L_d \bullet L_d$ and $L_d \bullet L_f$ terms have little effect on the non-yrast 3^- states wavefunctions,

and therefore little effect on the magnitude of the fragmentation. Additionally, $a_2 = 0.05$ MeV was used for all the calculations, and χ_2 was varied between values of $0.22-0.055N_B$. Zamfir *et al.* used the same IBM parameters that were used in an earlier study of the positive parity core [Zam93b].

No new IBM calculations were performed for the present analysis, which focuses on identification of low-lying octupole states in the even-even Pt isotopes. The preceding section is intended only to provide a reasonable framework for interpreting the Pt isotopes as examples of the O(6) symmetry in which a high degree of fragmentation is expected for the low energy octupole state.

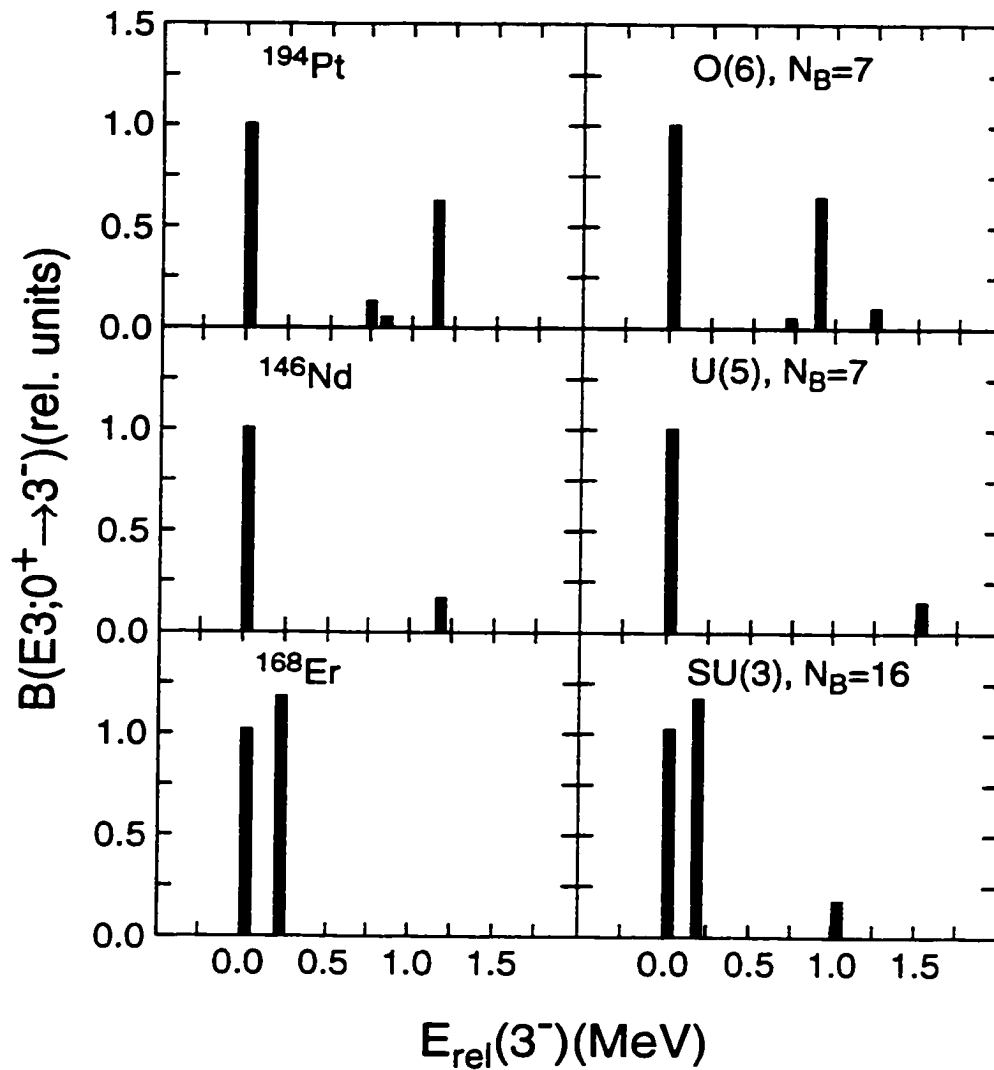


Figure 2.1: Octupole state strength distribution. (a) ^{194}Pt modeled as an $\text{O}(6)$ nucleus, (b) ^{146}Nd modeled as a $\text{U}(5)$ nucleus, and (c) ^{168}Er modeled as an $\text{SU}(3)$ nucleus. Of the three idealized symmetries, only the $\text{O}(6)$ symmetry can reproduce the significant octupole strength in higher-lying 3^- states in the IBM-1 formalism.

CHAPTER 3

$^{196}\text{Pt}(p, p'\gamma)$ COINCIDENCE EXPERIMENT

We performed a proton - γ coincidence experiment at the Florida State University Tandem-LINAC facility to study low-lying octupole states in ^{196}Pt . A 2.1 mg/cm² thick self-supporting target of 99% isotopically enriched ^{196}Pt was bombarded by a beam of 12.7 MeV protons. Both elastically and inelastically scattered protons were detected, as were the γ -ray de-excitations from excited target nuclei.

3.1 Beam Production

A beam of 12.7 MeV protons was produced from a commercially bought hydrogen cathode placed in a SNICS (source of negative ions by cesium sputtering) source. The SNICS source produces negative ions as an atomic beam from oven-heated cesium. The cesium beam is ionized as it contacts a hot, coaxial tantalum surface, and is accelerated toward a negatively biased cathode material from which neutral hydrogen atoms are sputtered. The hydrogen atoms pick up electrons as they pass through a layer of cesium condensed on the front of the cathode. The negatively charged hydrogen ions are then injected into the tandem Van de Graaff accelerator. Source intensities of up to 3 μA of negatively charged protons are obtainable.

The proton beam was accelerated by the Florida State University FN tandem Van de Graaff to an energy of 12.7 MeV. The negatively charged beam was stripped of electrons at the tandem terminal to produce a positively charged proton beam. The beam was focused by a series of quadrupole magnets and steered by dipole magnets into the experimental vault. We choose a beam energy of 12.7 MeV on

the basis of a number of $^{196}\text{Pt}(p, p'\gamma)$ measurements performed by the author. A range of beam energies between 10 MeV and 17 MeV were tried before deciding on 12.7 MeV. The lower limit of 10 MeV represents the minimum energy required to penetrate the Coulomb barrier, while 17 MeV was the maximum energy that did not produce so many neutrons as to overwhelm the detectors. In each trial, the total yields of elastic and inelastic proton events was monitored, as were background neutron and γ -ray radiation yields. The 12.7 MeV beam energy appears to optimize the inelastic scattering cross section relative to the elastic, while causing minimal γ -ray background from (p, n) and $(p, 2n)$ reactions. The energy is comparable to that used in a similar $^{198}\text{Pt}(p, p'\gamma)$ study [Yat88].

3.2 Particle - γ Detection

A new beam line and scattering chamber were constructed in the old target room for the particle - γ experiment. The new beam line was necessary to position the scattering chamber as close to the final quadrupole focusing magnet as possible to obtain a small, well-focused beam spot on the target. It is crucial in proton - γ experiments of this kind to minimize any background neutron radiation. The neutrons not only damage the γ -ray detectors, but also give rise to a high γ -ray background. Therefore, it is imperative that the beam strikes only the target material and does not impinge upon the target frame. Similarly, collimators could not be used to reduce the beam size because unwanted neutron and γ -ray background from protons striking the collimators would have resulted. 12.7 MeV protons are above the Coulomb barrier of most common collimator materials, and thus react readily with the collimators themselves. Since the beam spreads as a function of distance from the quadrupole magnet, it is advantageous to place the target at the minimum focal length of the magnet, thereby eliminating the need for collimators.

The beam dump consists of a 4.6 m long section of 15 cm beam pipe. The large diameter pipe and the large length of the beam dump is required to reduce background radiation. The end of the beam dump contains a natural carbon disk placed in the beam path. To further reduce the neutron background, the last 1.2 m of the beam dump is surrounded with 15 cm of boronated paraffin shielding. The boron has a large cross-section for absorbing neutrons, and the paraffin acts a moderator to slow the neutrons. The neutron dose rate along the beam line was reduced from 2000 mrem/hr during the first test run, to 2 mrem/hr during the production runs by this shielding and by carefully tuning the incident beam.

The scattering chamber built for the present experiment is a 20 cm diameter cylindrical chamber large enough to house a charged-particle detector and its cooling apparatus. The chamber radius is kept at a minimal size to allow γ -ray detectors to be placed as close as possible to the target, thereby increasing the target event to background ratio. In an effort to minimize γ -ray attenuation, the chamber walls were constructed at a minimal thickness needed to maintain structural integrity under vacuum. The chamber allows up to four targets to be inserted into the beam path without breaking vacuum. Figure 3.1 is a schematic drawing of the detector positions.

A single charged-particle detector was used to detect scattered protons. The detector was a 100 mm² area silicon surface barrier detector, having a thickness of 1.5 mm and placed 6 mm from the target position. The detector was thick enough to fully stop protons up to 20 MeV. The charged-particle detector was placed at 90° to the incident beam direction, an angle at which the elastically scattered proton cross section is much smaller than that at more forward angles. The cross section for inelastically scattered protons at 90° is comparable to that at more forward angles.

The particle detector has an intrinsic resolution of 50 keV for detecting alpha particles from ²²⁸Th and ²⁴¹Am radioactive sources. The in-beam resolution, how-

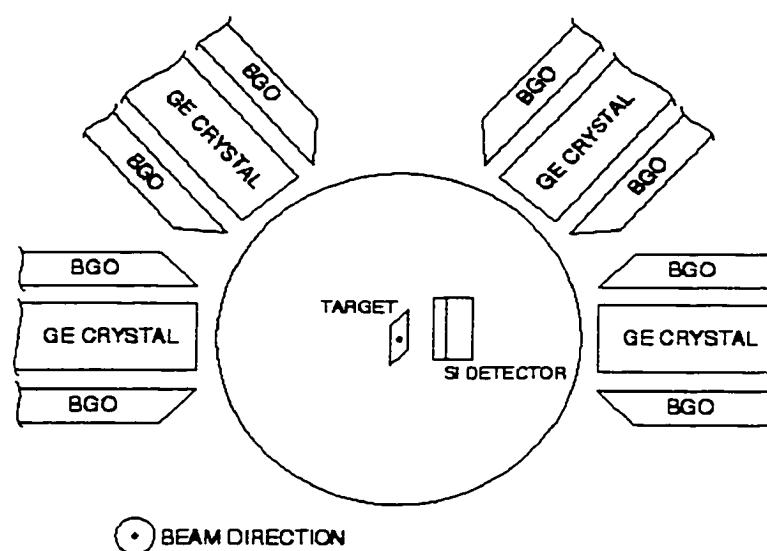


Figure 3.1: Schematic of the $^{196}\text{Pt}(p, p'\gamma)$ experimental apparatus.

ever, was considerably worse (150 keV) due to “pile up”, a successive particle event occurring in the detector before the charge from the preceding event has been collected. A major contributor to the pile up was beta decay from the activated target in which ^{196}Au had been produced via the $^{196}\text{Pt}(p, n)$ reaction. After a few hours of beam on target, the beta decays became frequent enough to interfere with the detector resolution. A number of ways to reduce the resolution degradation were investigated, including placing magnets around the detector entrance path to deflect unwanted electrons, and biasing the target with positive voltage to capture the produced electrons. These methods had only a small effect on the pile up.

A compromise was made, finally, between maximizing the beam current on target and minimizing the resolution of the charged particle detector. During the production runs, the detector was cooled by thermal contact with a brass block in which ethanol chilled to -20°C was circulated. Cooling the detector minimizes the effects of neutron damage in the detector.

Detecting γ -ray de-excitations was considerably more straightforward than particle detection. Four Compton-suppressed n-type hyper-pure Ge (HPGe) detectors having 20 % relative efficiency and 2.5 keV resolution at 1.33 MeV from the FSU-Pitt Gamma Array [Tab93] were used to identify γ -ray de-excitations from excited target nuclei. All four detectors were placed at 90° to the beam direction in a semi-circle surrounding the scattering chamber (see Figure 3.1). The detectors were placed as close as possible (6 cm) to the target to maximize the beam event to background ratio. Even so, the γ -ray background was significant.

The γ -ray background is mainly produced in two ways. The first is from reactions away from the target position. As mentioned previously, 12.7 MeV protons are above the Coulomb barrier on most materials commonly used in beam line construction. Neutrons and γ -rays were produced, therefore, around the quadrupole focusing magnet before the detector, and from secondary scattered protons after the target. Although Compton suppression of the Ge detectors reduces this background to a great extent, a large amount of shielding and very careful beam tuning was required to further reduce the background. The beam tuning was performed while monitoring radiation flux along the beam line. The second major source of γ -ray background came from (p,n) and (p,2n) reactions of protons with the ^{196}Pt target. The dominance of (p,n) and (p,2n) reactions was also seen in $^{198}\text{Pt}(p,p'\gamma)$ experiments [Yat88]. Unlike the first source, these background events take place at the target position and can not be reduced by shielding. Fortunately, γ -rays from (p,n) and (p,2n) reactions are not associated with a scattered proton, and a care-

ful particle- γ coincidence requirement can filter out a majority of these unwanted events. Even with a coincidence requirement, however, many “chance” coincidence events were seen between an elastically scattered proton and a γ -ray de-excitation from (p,n) and (p,2n) reactions.

The particle- γ coincidence requirement is crucial for two reasons. The first is to reduce the dominating background from (p,n) and (p,2n) reactions just mentioned. The second, and perhaps more important reason, is to associate each γ -ray decay with a particular excitation of the target nucleus. The particle- γ coincidence condition required a particle event followed by a γ -ray event from any one of the four Ge detectors within a 200 ns time window. To further separate true coincidences from the chance coincidences falling within the 200 ns time window, the time difference between the detected particle and the γ -ray in coincidence with it was recorded via a time-to-amplitude converter (TAC). The TAC was started by a particle event and stopped by any γ -ray event. Prompt coincidences resulting from an inelastically scattered proton and the γ -ray de-excitation of the populated state all occur at one specific time difference, while chance coincidences from other γ -ray de-excitations occur over a continuum of time differences within the 200 ns time window. The TAC spectrum (Figure 3.2 (a)) shows a peak at the prompt coincidence time difference sitting on top of the chance coincidence events. The prompt TAC peak was used as a gating requirement in the off-line analysis.

The collected particle- γ events were sorted in two separate matrices of particle energy versus γ -ray energy. One of the matrices was sorted with a gate on the prompt time peak seen in the TAC spectrum, and the other was sorted with a gate on an equal number of channels of the chance coincidence event time background. The chance time gated matrix was subtracted from the prompt time gated matrix to produce a single time background subtracted particle- γ matrix. Figures 3.2 (b) and (c) show the dramatic effect of using the TAC to filter chance coincidences. The

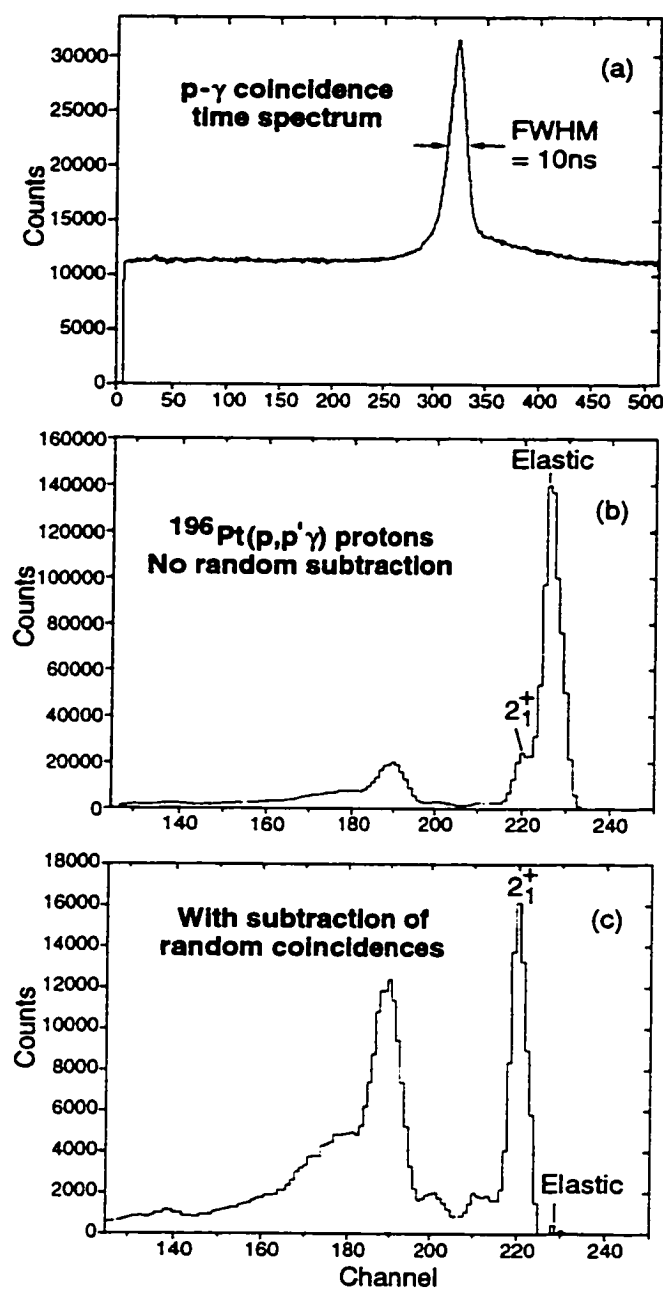


Figure 3.2: The TAC timing spectrum and gated particle projections. (a) The time spectrum is the total yield as a function of the time difference between a particle and γ -ray event. A peak from the prompt coincidences sits above a continuum of “chance coincidence” background. (b) Projected proton spectrum before any software gating. The first excited state is seen as a shoulder of the elastic proton peak. (c) Projected proton spectrum with the chance coincidences subtracted. The elastic peak is nearly completely suppressed, and the spectrum is dominated by the first excited state.

proton spectrum in Figure 3.2 (b) is shown without any TAC gating condition. The first excited state in ^{196}Pt appears as a “shoulder” on the dominant elastic peak. The same proton spectrum is shown again with the chance coincidences subtracted from the prompt in Figure 3.2 (c). The elastic peak, which dominated the spectrum when no gating was imposed is nearly completely suppressed, while the first excited state now dominates the spectrum.

3.3 Particle- γ Electronics

The electronics requirements were fairly straightforward for the experiment. Figure 3.3 is a diagram of both the signal and logic electronics. The particle signals were split after pre-amplification into energy and timing signals. The energy signal was fed directly into a spectroscopy amplifier for signal amplification and shaping. The timing signal goes first to a fast timing filter amplifier (TFA) for signal shaping. The output is fed to a constant fraction discriminator (CFD) where the leading edge of the signal is picked off and used to start the TAC.

The Ge detector electronics were set up in a similar fashion. The energy signal was pre-amplified and sent directly to a spectroscopy amplifier. The timing signal from the preamplifier feeds a TFA, whose output is discriminated by a CFD. The CFD output goes to a “blue box” coincidence unit to be used in Compton suppression and to set a logical OR condition for the four Ge detectors. In its capacity as a logical OR unit, any timing signal from one of the four Ge detectors generates a new timing signal from the coincidence unit.

Compton suppression is handled by the same “blue box” coincidence unit built at Florida State University specifically for that purpose. The unit allows for easy adjusting of the delay and width of both the Compton shield and the Ge detector timing signals. The Compton BGO shield signal is fed to a TFA, whose output is picked off by a CFD. The CFD output feeds the “blue box” unit, where internal

timing signals are generated. The shield timing signal is adjusted in time to fit completely around the Ge detector signal, and is used to veto any Ge signal for which a shield event is seen. The veto is made internally so that a timing signal is generated only for non-Compton scattered events. A coincidence requirement set to a multiplicity of one is used to logically OR the four Ge signals. Therefore, any non-Compton scattered event from any of the four Ge detectors results in a positive timing signal. The timing signal is delayed by 280 ns and used as a stop condition for the TAC.

Coincidence gating by the TAC is done by using the TAC output, which signifies a particle event followed by a γ -ray event within 200 ns, to generate a positive particle- γ coincidence signal. The signal is lengthened in time by a gate and delay generator (GDG) to fit completely around the spectroscopy amplifier energy signals from all detectors, and is used as a master gate at the analog-to-digital converters (ADCs) for data acquisition.

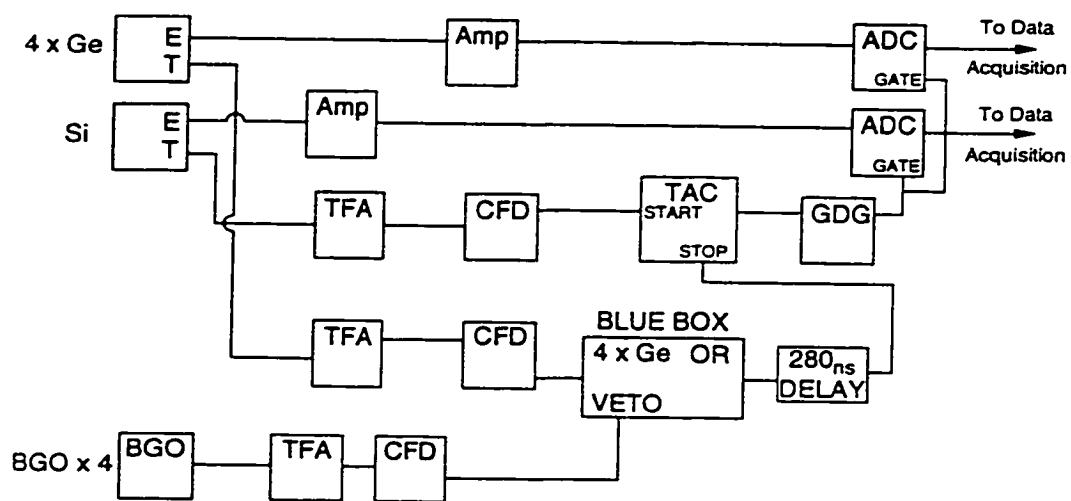


Figure 3.3: Diagram of the electronics. Both the signal and logic electronics are included.

CHAPTER 4

ANALYSIS AND RESULTS OF ^{196}Pt DATA

4.1 Previous Experimental Work on ^{196}Pt

Previous experimental [Cot88a, Cot88b, Yat88, Zam93a] work shows that the lowest energy octupole states (3_1^- states) in the even-even Pt isotopes ($^{194,196,198}\text{Pt}$) and some of the Os isotopes have substantially lower excitation energies than do the corresponding states in the rest of the heavy transitional mass region. The lowest energy octupole states in the stable even-even Hg and Pb nuclei are around 2.6 MeV. This value remains fairly constant throughout the mass region as evidenced by Figure 4.1. The figure depicts the energy of the lowest-lying octupole state, the 3_1^- state, for nuclei in the heavy transitional mass region. The energy for the lowest octupole state in the Pt isotopes, represented as triangles in Figure 4.1, resides nearly 1 MeV lower than in the other nuclei of the region. In addition, the drop in the energy of this 3_1^- state is seen to be rather abrupt. This abrupt drop is not seen elsewhere in the heavy transitional region, nor is it seen in other mass regions above $A \geq 16$ [Spe88].

Cottle *et al.* suggested that the anomalous lowering of the 3_1^- state energy in the even-even Pt isotopes was due to a fragmentation of the octupole phonon strength [Cot88a]. They proposed that the octupole phonon strength was not concentrated in the 3_1^- state, but rather was shared between a number of 3^- states. The identification of additional 3^- states is a major focus of the present work and will be discussed later. If a number of additional low energy octupole states could be identified, then a better measure of the octupole state energy may be the energy of the centroid,

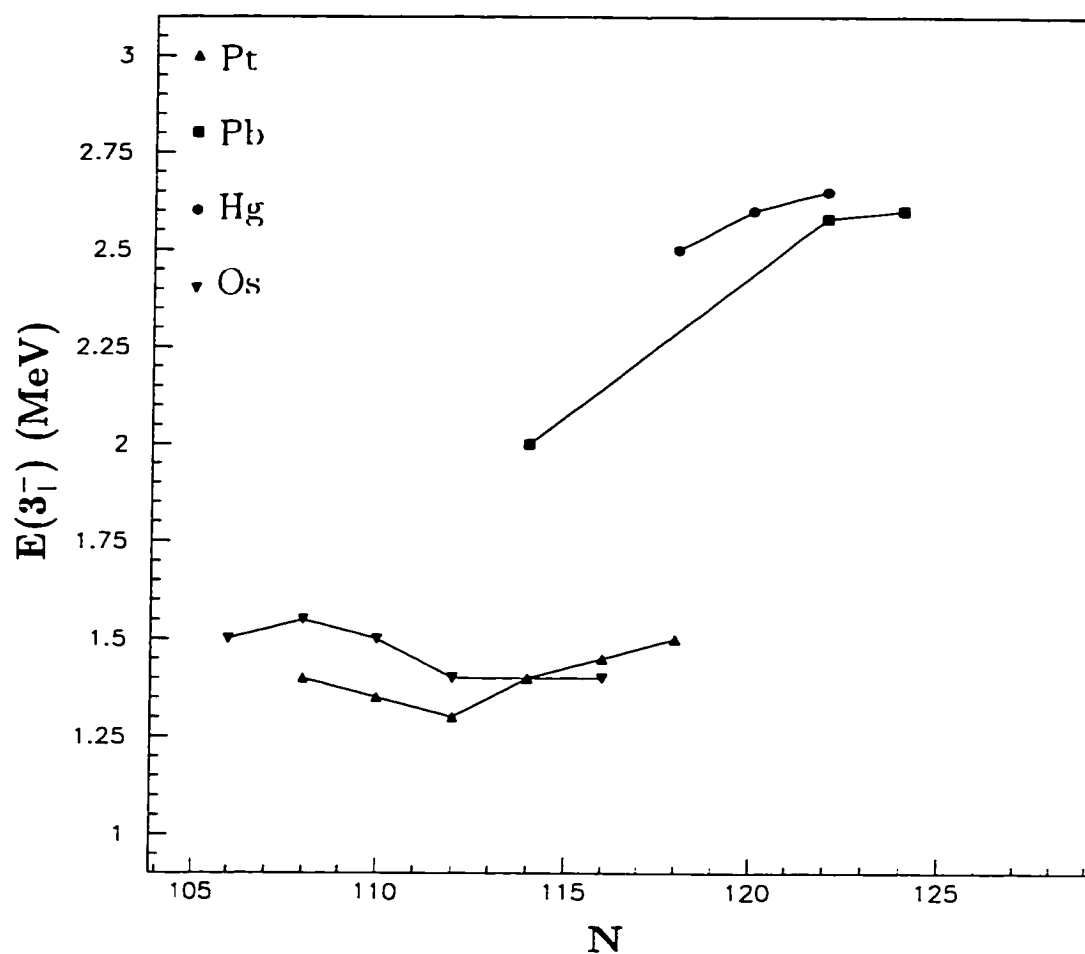


Figure 4.1: Energy systematics of the 3_1^- states in the heavy transitional mass region ($74 \leq Z \leq 82$). The energies of the lowest octupole state in Hg and Pb are nearly constant around 2.6 MeV. In the Pt and Os isotopes, however, (shown respectively as triangles and inverted triangles) the energy of the lowest octupole state is nearly 1 MeV lower.

defined as

$$C = \frac{\sum_i E_i B(E3; 0_{g.s}^+ \rightarrow 3_i^-)}{\sum_i B(E3; 0_{g.s}^+ \rightarrow 3_i^-)} \quad (4.1)$$

The centroid measure is a weighted average of the octupole state energy. The energy of each octupole state is scaled by the amount of the octupole phonon strength ($B(E3; 0_{g.s}^+ \rightarrow 3^-)$) it carries. Looking again at the mass region systematics of the octupole state energy in Figure 4.2, we see that the value of the octupole state energy for the Pt isotopes, indicated by the open triangles, is very similar to those in Hg and Pb when using the centroid measure. If, in fact, the octupole state strength is fragmented over a number of states, then fragmentation provides an explanation for the observed lowering of the 3_1^- state energy. As a simple measure of the magnitude of the octupole fragmentation, Cottle *et al.* offered the quantity

$$\Delta E3 = C - E(3_1^-) \quad (4.2)$$

where C is the centroid of the octupole state energy as defined previously, and $E(3_1^-)$ is the energy of the lowest octupole state. It is seen, then, that if the octupole strength is concentrated in a single state, the degree of fragmentation is zero. As the strength spreads out over a large energy range, the fragmentation increases, as seen in the Pt isotopes. The proposal of octupole fragmentation provides a nice explanation for the reduced energy of the 3_1^- state, and is understood in the even-even Pt isotopes as an expression of $O(6)$ symmetry in the IBM formalism [Zam93b].

Octupole fragmentation has been observed before. In fact, large degrees of fragmentation of vibrational phonons have been observed and are well understood for many well-deformed nuclei [Nee70, Bar88, Cot90]. However, the even-even Pt isotopes of the heavy transitional region are not well-deformed. Also, there is no experimental example which indicates that this large a fragmentation of the octupole phonon strength is expected. Indeed, a fragmentation of this magnitude can not be

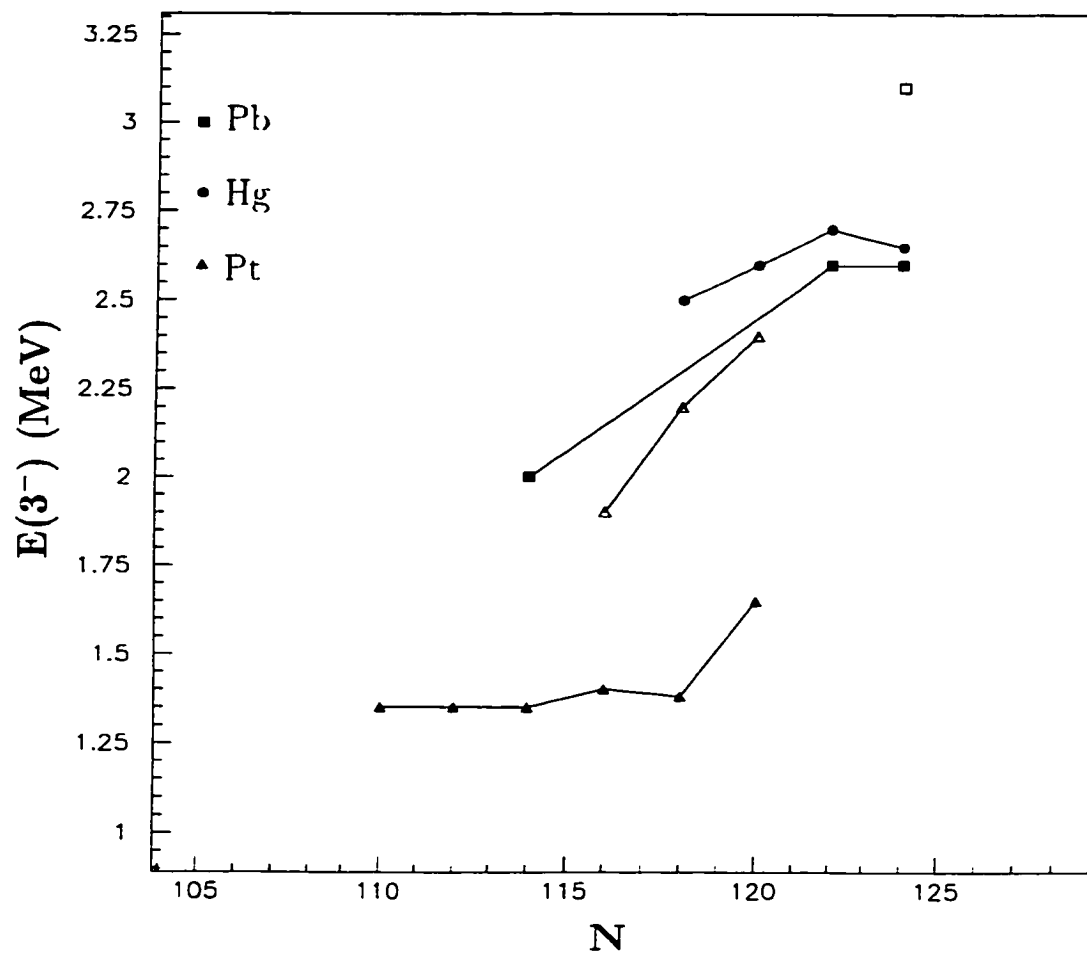


Figure 4.2: Energies of the low energy octupole state in the heavy transitional region. The open shapes indicate the centroid energy of the low energy octupole state, while the closed shapes are the 3_1^- state energies.

seen in any other mass region [Cot90]. The ratio

$$R_{4/2} = \frac{E(4_1^+)}{E(2_1^+)} \quad (4.3)$$

provides a measure of deformation which allows a study of how the octupole deformation depends on quadrupole deformation. The magnitude of octupole fragmentation seen in the Pt isotopes can be compared in a meaningful way to other nuclei. $R_{4/2}$ has long been used as a structural indicator of the degree of quadrupole deformation for medium and heavy mass nuclei. Values of 2.0 indicate a spherical harmonic vibrator, while values of 3.3 represent an upper limit to the most deformed nuclei known. The Pt isotopes in question have $R_{4/2} \approx 2.3$, indicating that they do not possess a large static deformation. Looking at a plot of ΔE_3 , the degree of octupole fragmentation, as a function of $R_{4/2}$ in Figure 4.3, shows the extremely high degree of fragmentation seen in the even-even Pt isotopes. They show a larger degree of fragmentation than even the most statically deformed nuclei. The present work seeks to confirm the occurrence of octupole fragmentation in the even-even Pt isotopes by confirming $J^\pi = 3^-$ assignments for the presumed octupole states.

The first step in understanding the octupole fragmentation is to identify higher-lying 3^- states in the even-even Pt isotopes. A considerable amount of information and study has been done previously which lends insight to the present work. In 1981 Deason *et al.* [Dea81] performed proton scattering experiments at a 35 MeV beam energy on $^{194,196,198}\text{Pt}$. A number of states in each Pt isotope were populated in the reaction which were identified as good candidates of higher-lying octupole states. Deason *et al.* made tentative spin assignments of the same states based on their measurements of angular distributions from scattered protons. A later proton- γ coincidence experiment performed by Yates *et al.* [Yat88] on ^{198}Pt identified a 2603 keV state which was tentatively assigned $J^\pi = 3^-$. Yates *et al.* further noted that the 2603 keV state corresponded to one of the states seen in the (p, p') experiment of Deason *et al.* Prompted by this new development, a further analysis of the

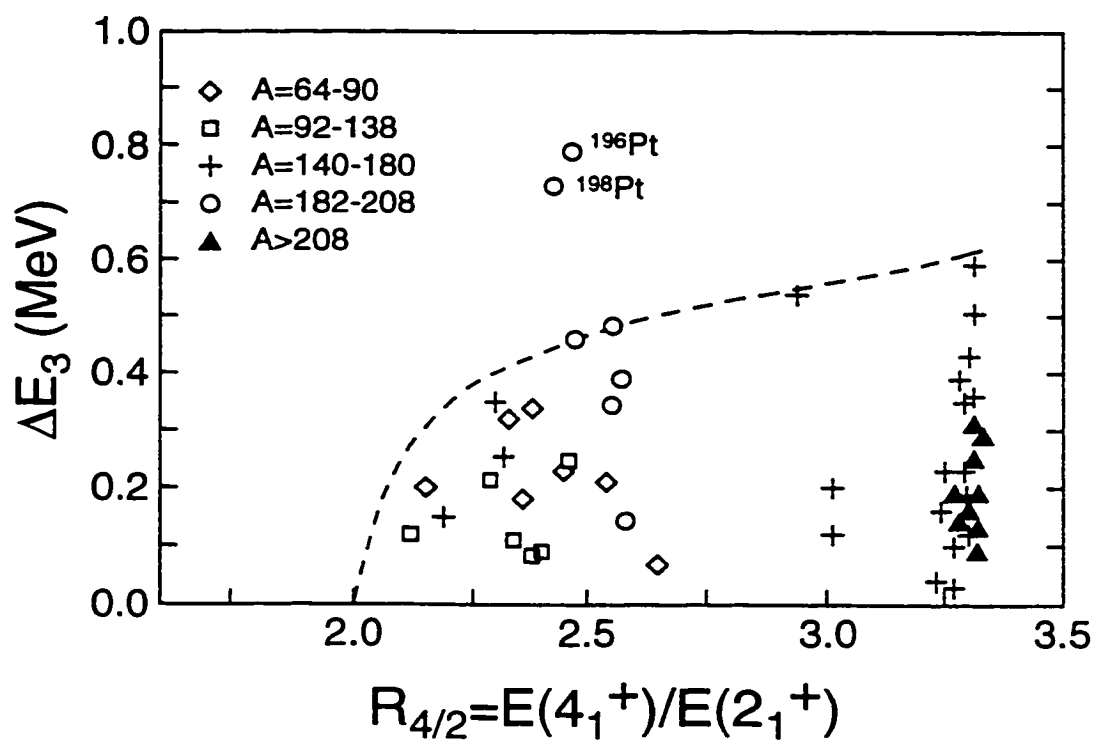


Figure 4.3: The magnitude of fragmentation is plotted against $R_{4/2}$, a structural indicator of the degree of static quadrupole deformation. The degree of fragmentation seen for the Pt isotopes is greater than that of even the most statically deformed examples of nuclei.

scattered proton angular distributions was performed by Cottle *et al.* [Cot88a] to more definitely determine the spins and parities of some of the higher-lying states. Cottle *et al.* modeled the proton angular distributions with a coupled channels analysis and compared the angular distributions to lower-lying states with known spin. A total of 11 states in the three Pt isotopes ($^{194,196,198}\text{Pt}$) were identified as being higher-lying octupole states containing a significant amount of the total octupole phonon strength. However, uncertainty existed in the spin assignments of these states. It is clear by looking at the example in Figure 4.4 that the proton angular distribution of a 4^+ state is nearly identical to that of a 3^- state in the data set of Deason *et al.*. Hence, a 4^+ spin assignment could not be excluded for the suggested octupole states in question.

For one of the Pt isotopes at least, ^{196}Pt , more information soon became available when DiPrete *et al.* [DiP93] performed a low energy neutron scattering experiment with neutron beam energies between 2.0 and 3.5 MeV. DiPrete *et al.* detected the γ -ray de-excitations from excited states and set constraints on the spin and parity assignments of the proposed octupole states based on γ -ray angular distributions. Twelve states were identified which could correspond to the same states populated by (p, p') . Unfortunately, DiPrete *et al.* could not determine exactly which states corresponded to the proposed octupole states. The difficulty in making a correspondence between the states seen by DiPrete *et al.* and the ones seen by Deason *et al.* stems from the non-selectivity of the neutron scattering reaction at low beam energies. Unlike proton scattering, which strongly populates single phonon states [Pet86], neutron scattering populates all states at or below their excitation threshold energy in a statistical fashion to a near equal extent. Because there is no Coulomb barrier to overcome, states can be populated in (n, n') which are only 100 or 200 keV above their excitation threshold, and spectral complications from higher-lying

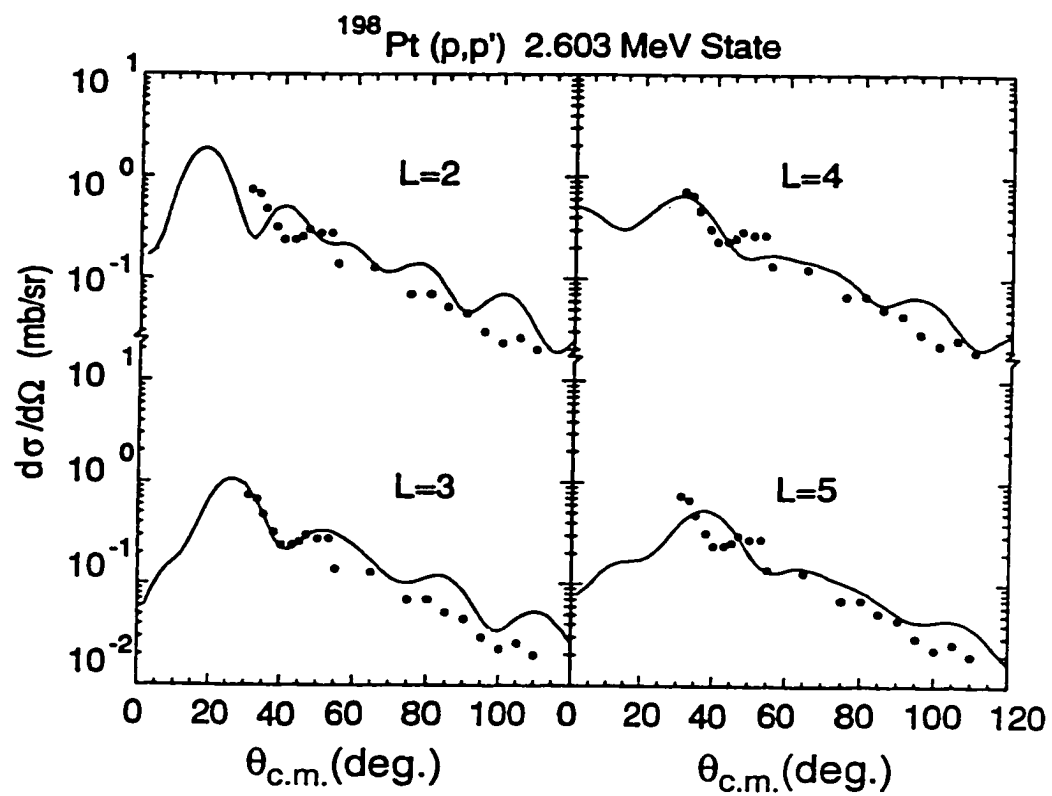


Figure 4.4: Proton angular distributions compared to coupled channels calculations. The similarity between 3^- and 4^+ states makes impossible an unambiguous spin assignment based on the proton angular distributions alone.

states are avoided. Thus, a number of states seen by Diprete *et al.* could correspond to the proposed octupole states.

The specific goal of the $^{196}\text{Pt}(n, n'\gamma)$ experiment by Diprete *et al.* was to identify the possible octupole states corresponding to those populated in (p, p') by Deason *et al.* by extracting all possible spin and parity information from the measured properties of γ -ray decays. The minimal energy uncertainty provided by γ -ray detection permits much more reliable energy level determination than that obtainable from charged-particle detection such as (p, p') [Dea81] or (e, e') [Pon92]. DiPrete *et al.* set specific criteria for a state seen in their $(n, n'\gamma)$ reaction to be identified as an octupole state from the (p, p') reaction. First, they required that the energy of the state fall within 15 keV of the energy reported by Deason *et al.*. Deason *et al.* quote an energy uncertainty between 8-10 keV for their experiment. Secondly, DiPrete *et al.* required that the state have a spin and parity assignment of either 3^- or 4^+ from their γ -ray decay properties. The states in question were known to have either 3^- or 4^+ assignments based on the (p, p') angular distributions [Cot88a].

Of the 107 states observed in their $^{196}\text{Pt}(n, n'\gamma)$ reaction, Diprete *et al.* identified 12 states fitting these criteria for which a spin assignment of 3^- or 4^+ was allowed by the γ -ray angular distributions, which could correspond to the possible octupole states seen in (p, p') . The candidate states proposed by Diprete *et al.* are shown in Figure 4.5 along with the states seen in (p, p') to which they correspond.

4.2 Analysis of $^{196}\text{Pt}(p, p'\gamma)$ Experiment

The intended goal of the present $^{196}\text{Pt}(p, p'\gamma)$ coincidence experiment was to identify which four of the 12 candidate states observed in Reference [DiP93] were actually populated in the previous (p, p') study of Deason *et al.* [Dea81]. Identifying these states allows energy level placements based on the highly reliable γ -ray decay energies as opposed to relying on tentative placements made from proton scattering

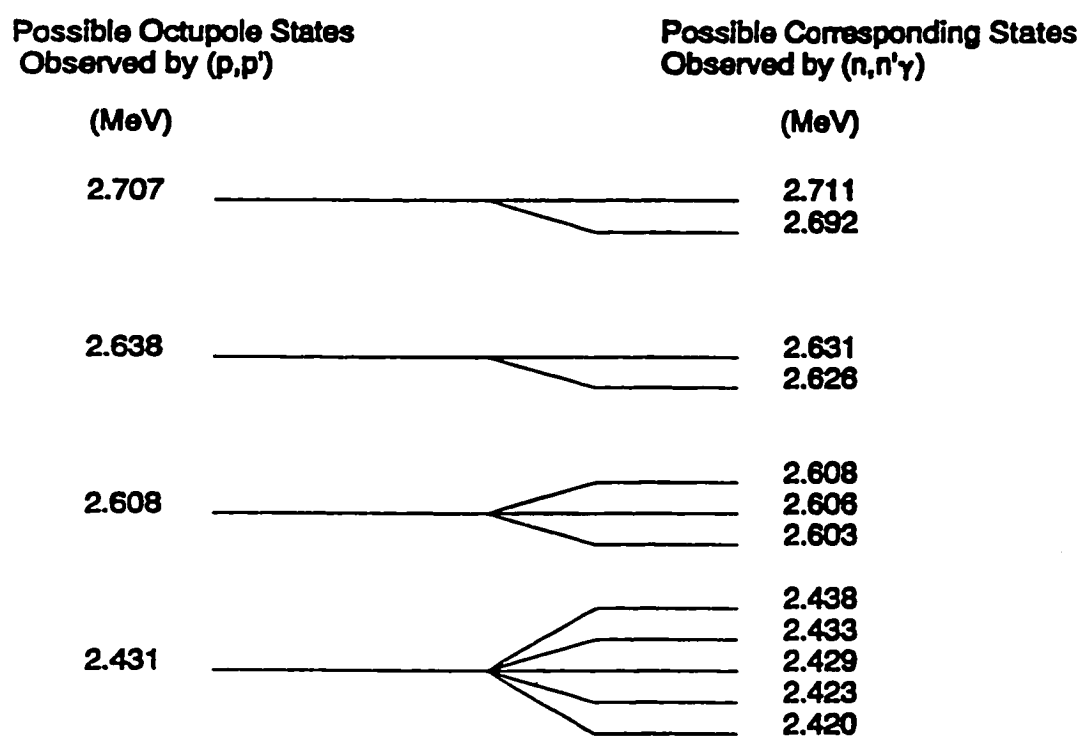


Figure 4.5: The proposed octupole candidate states in ^{196}Pt . γ -ray angular distributions allow for a $J^\pi = 3^-$ spin assignment for each state. Additionally, each state energy is, within error, consistent with one of the proposed octupole states seen in (p,p')

and electron scattering information. Although Ponomarev *et al.* have assigned three states in ^{196}Pt with $J^\pi = 3^-$ from an $^{196}\text{Pt}(e, e')$ study [Pou92], it is desirable to identify exactly which states their assignments refer to, using the best available information, namely, the γ -ray decay energies [DiP93].

It is possible that more than four of the candidate states were populated in the previous (p, p') study. Since Deason *et al.* reported an energy resolution of no better than 2-8 keV, proton peaks interpreted as single peaks may, in fact, be multiple states which were unresolved in their experiment. However, there is no evidence in the present $(p, p'\gamma)$ experiment for this occurring. It is further assumed that inelastic proton scattering of 12.7 MeV protons selects the same states seen in the 35 MeV (p, p') reaction of Reference [Dea81]. Table 4.2 summarizes the experimental findings of the present $^{196}\text{Pt}(p, p'\gamma)$ experiment. The table shows the populated states, γ -ray decays from these states, and measured branching ratios where possible. Figure 4.6 is an abbreviated energy level decay scheme showing the states populated in the present experiment. The following analysis will rely heavily on previous results, while taking advantage of the new coincidence information of the present experiment.

As an example of the quality of the proton- γ coincidence information, Figure 4.7 shows γ -ray and proton projected spectra. The γ -ray spectrum is projected from a gate placed on proton events at 2245 keV and shows the 2245 keV γ -ray decay to the ground state, shown in the decay scheme of Figure 4.6. Likewise, the proton spectrum is projected from a gate placed on the 2245 keV γ -ray and shows the 2245 keV proton peak. The contaminant 1969 keV γ -ray is from the γ -ray decay chain of the 2262 keV state, which predominately decays to the 1969 keV state by a 293 keV γ -ray. The 1969 keV state subsequently decays to the ground state by a 1969 keV γ -ray. Due to our poor proton energy resolution (150 keV), the 2262 keV state can not be separated from the 2245 keV state in the proton gating. The 2245 keV

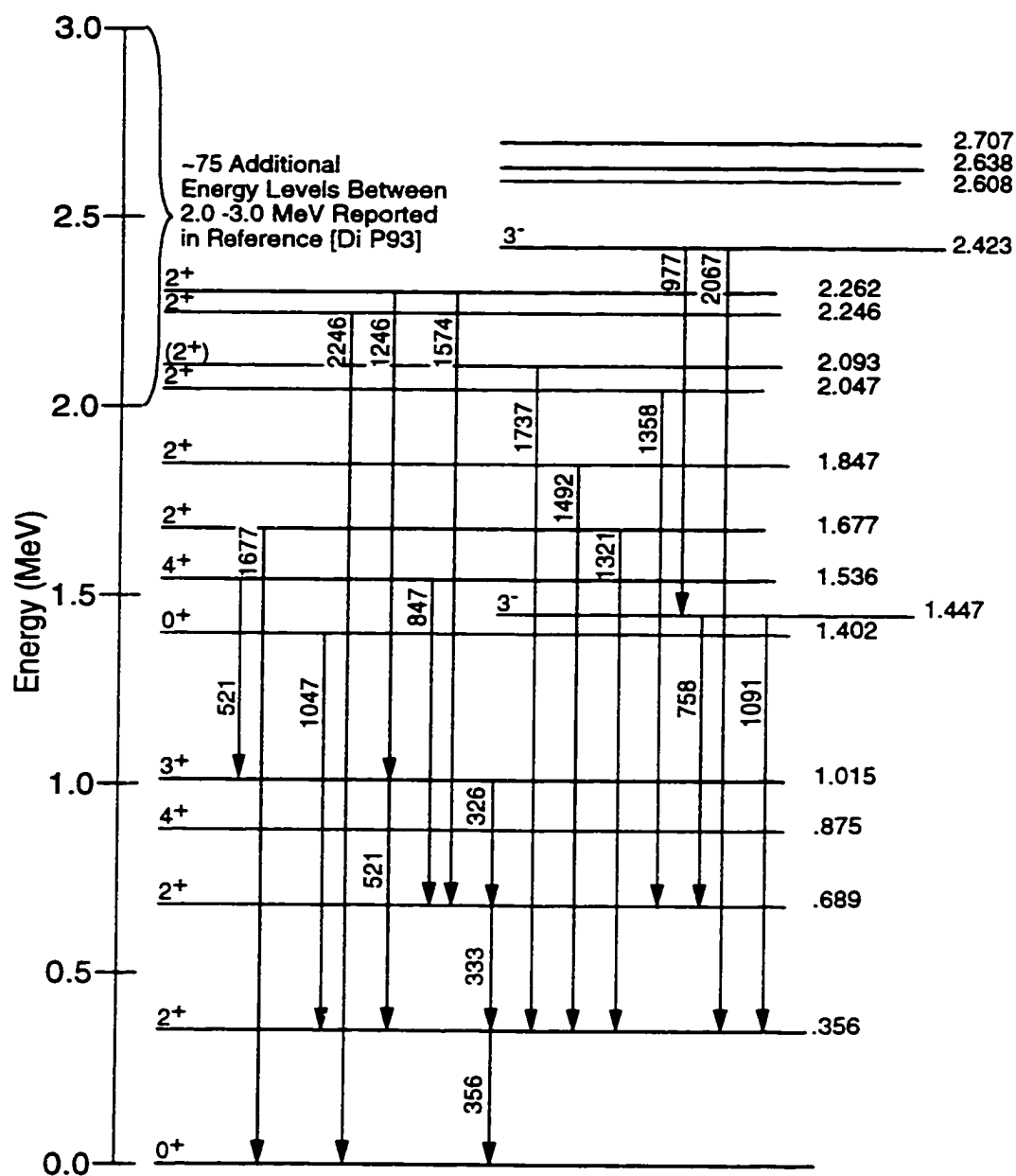


Figure 4.6: Abbreviated energy level decay scheme showing the states populated in the present $^{196}\text{Pt}(p, p'\gamma)$ experiment.

Table 4.1: Energy levels and γ -ray transitions observed in $E_p = 12.7$ MeV $^{196}\text{Pt}(p, p'\gamma)$ reaction.

| E_{level} (keV) | E_γ (keV) | Branching ratio | E_f (keV) | $I_i^\pi \rightarrow I_f^\pi$ |
|-------------------|------------------|-----------------|-------------|-------------------------------|
| 355.7(2) | 355.7(2) | | 0 | $2^+ \rightarrow 0^+$ |
| 688.7(2) | 332.9(2) | | 356 | $2^+ \rightarrow 2^+$ |
| 876.8(3) | 521.1(2) | | 356 | $4^+ \rightarrow 2^+$ |
| 1015.0(2) | 326.3(2) | | 689 | $3^+ \rightarrow 2^+$ |
| 1402.7(3) | 1047.0(3) | | 356 | $0^+ \rightarrow 2^+$ |
| 1447.0(2) | 758.4(2) | 12(4) | 689 | $3^- \rightarrow 2^+$ |
| | 1091.1(3) | 88(17) | 356 | $3^- \rightarrow 2^+$ |
| 1535.8(3) | 847.1(3) | 17(9) | 689 | $4^+ \rightarrow 2^+$ |
| | 521.0(4) | 83(11) | 1015 | $4^+ \rightarrow 3^+$ |
| 1677.2(5) | 1677.3(6) | 68(45) | 0 | $2^+ \rightarrow 0^+$ |
| | 1321.4(5) | 32(81) | 356 | $2^+ \rightarrow 2^+$ |
| 1847.3(5) | 1491.6(5) | | 356 | $2^+ \rightarrow 2^+$ |
| 2047.0(4) | 1358.3(4) | | 689 | $2^+ \rightarrow 2^+$ |
| 2093.0(3) | 1737.3(3) | | 356 | $(2^+) \rightarrow 2^+$ |
| 2245.6(7) | 2245.6(7) | | 0 | $2^+ \rightarrow 0^+$ |
| 2262.4(7) | 1246.7(7) | 67(15) | 1015 | $2^+ \rightarrow 3^+$ |
| | 1573.5(7) | 33(18) | 689 | $2^+ \rightarrow 2^+$ |
| 2423.4(4) | 976.7(3) | 52(13) | 1447 | $3^- \rightarrow 3^-$ |
| | 2067.6(7) | 48(22) | 356 | $3^- \rightarrow 2^+$ |

state is of some interest in a matter not related to octupole excitations, and will be briefly discussed in the following chapter.

Of the 4 higher-lying octupole states proposed by DiPrete *et al.* [DiP93], we see evidence for only one of the states. The evidence in support of an octupole inter-

pretation for this state, however, is very strong. Gating on inelastically scattered protons at 2423 keV reveals a 2067.6 keV γ -ray in coincidence with the protons. The 2067.6 keV γ -ray was previously reported by DiPrete *et al.* [DiP93] as decaying from a 2423 keV state to the 2_1^+ level (see Figure 4.6). A gate on the 2067.6 keV γ -ray shows this same coincidence as a proton peak at 2423 keV. Both γ -ray and proton projected spectra are shown in Figure 4.8 (a) and (b) respectively.

Figure 4.9 (a) also shows that, in addition to the 2067.6 keV γ -ray decay, the 2423 keV state also decays by emission of a 976.7 keV γ -ray to the lowest-lying octupole state, the 3_1^- state, seen in Figure 4.6. This decay has not been reported previously and lends certainty to the placement of the 2423 keV energy level. The proton projection showing the coincidence between the 976.7 keV γ -ray and the 2423 keV state is shown in Figure 4.9 (b).

Of the 12 candidate states identified in Reference [DiP93], the 2423 keV state is one of the three for which $J^\pi = 4^+$ is excluded by γ -ray angular distribution measurements. The proton angular distribution measurements of Reference [Cot88a] have already limited the spin assignment to either 3^- or 4^+ . We can therefore unambiguously assign $J^\pi = 3^-$ to the 2423 keV level.

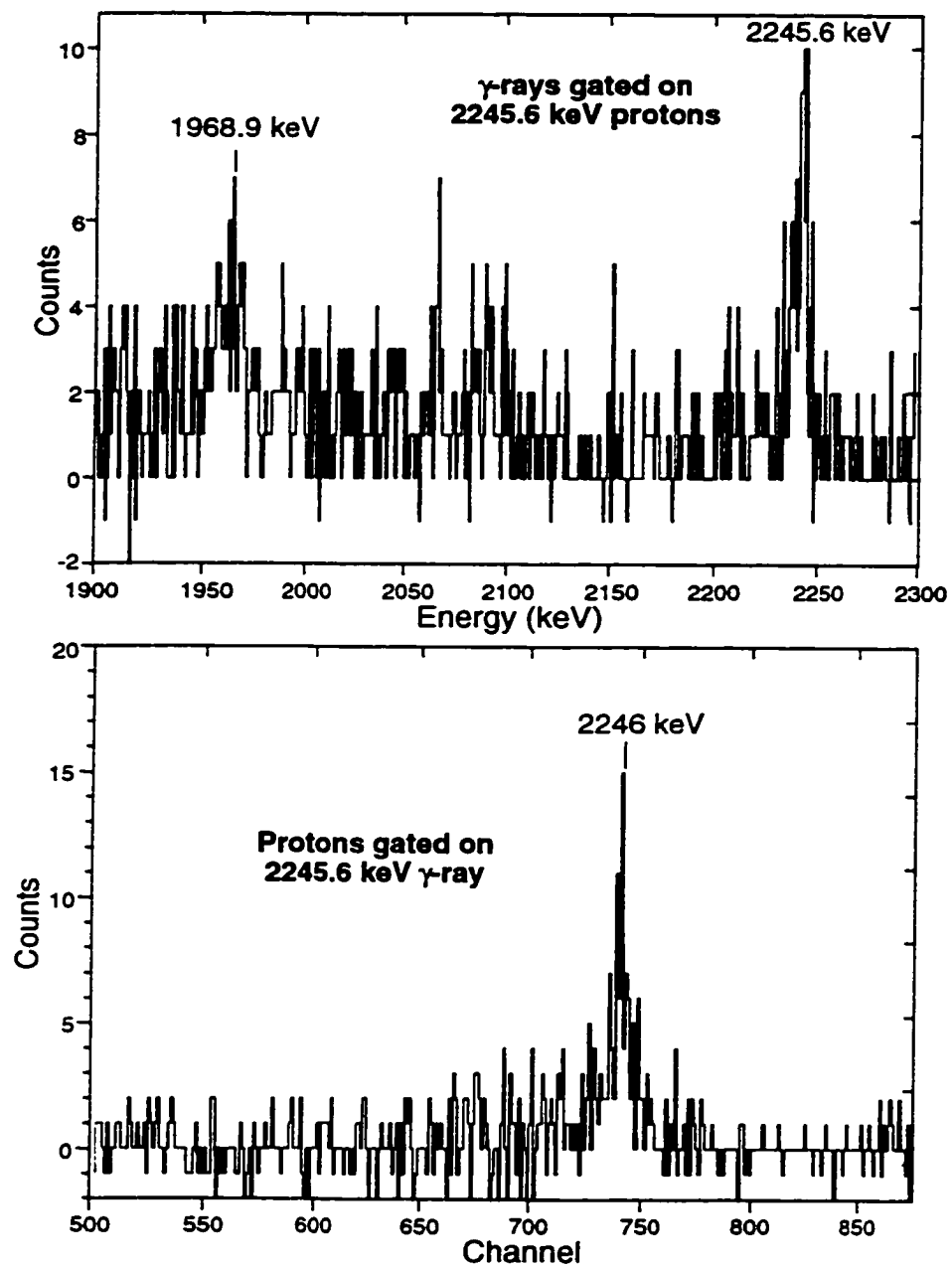


Figure 4.7: (a) γ -ray spectrum showing the 2245 keV γ -ray decay to the ground state and (b) the proton spectrum showing a peak from the 2245 keV state.

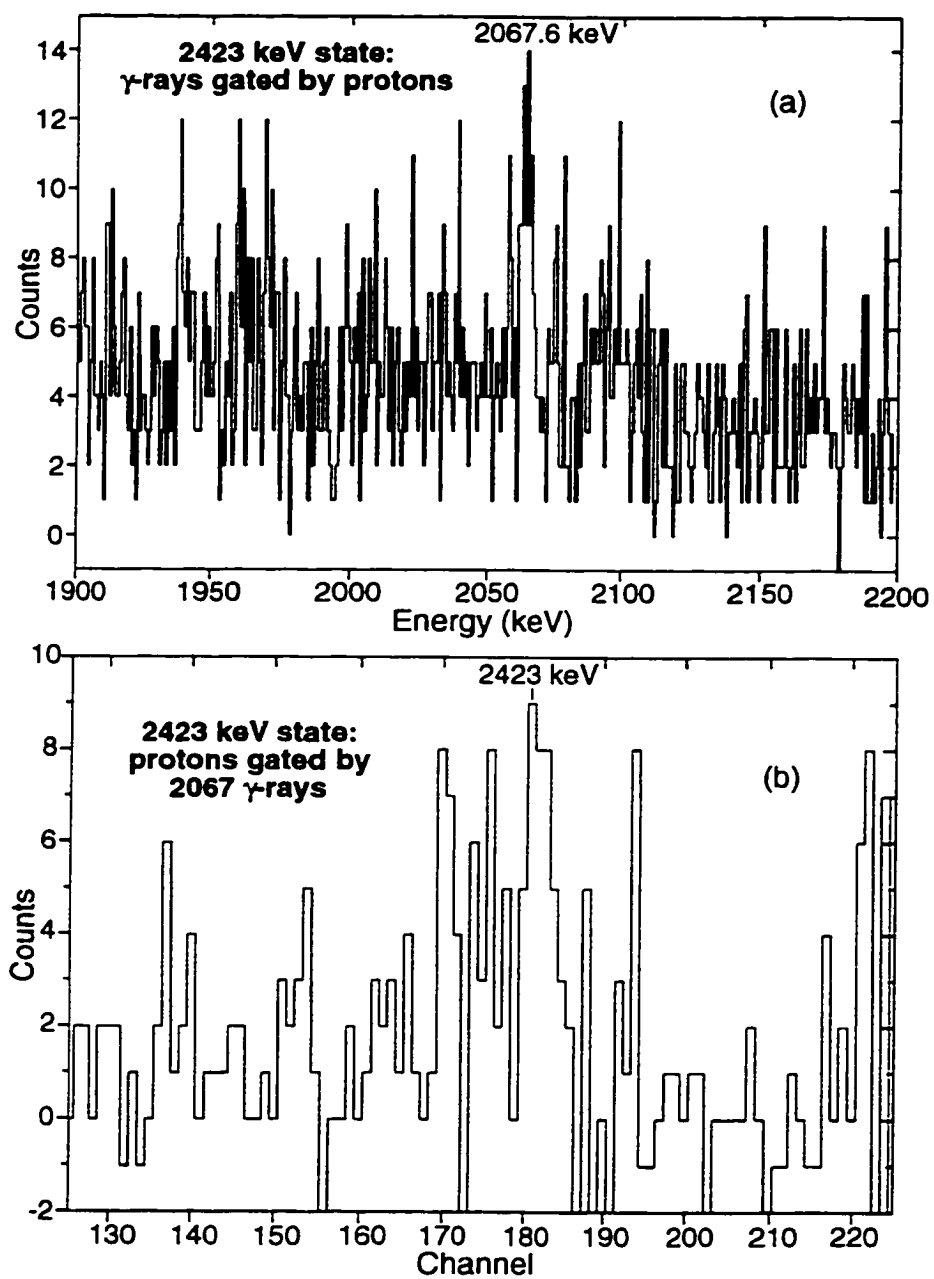


Figure 4.8: (a) γ -ray and (b) proton spectra showing the previously reported decay from the 2423 keV state by a 2067.6 keV γ -ray.

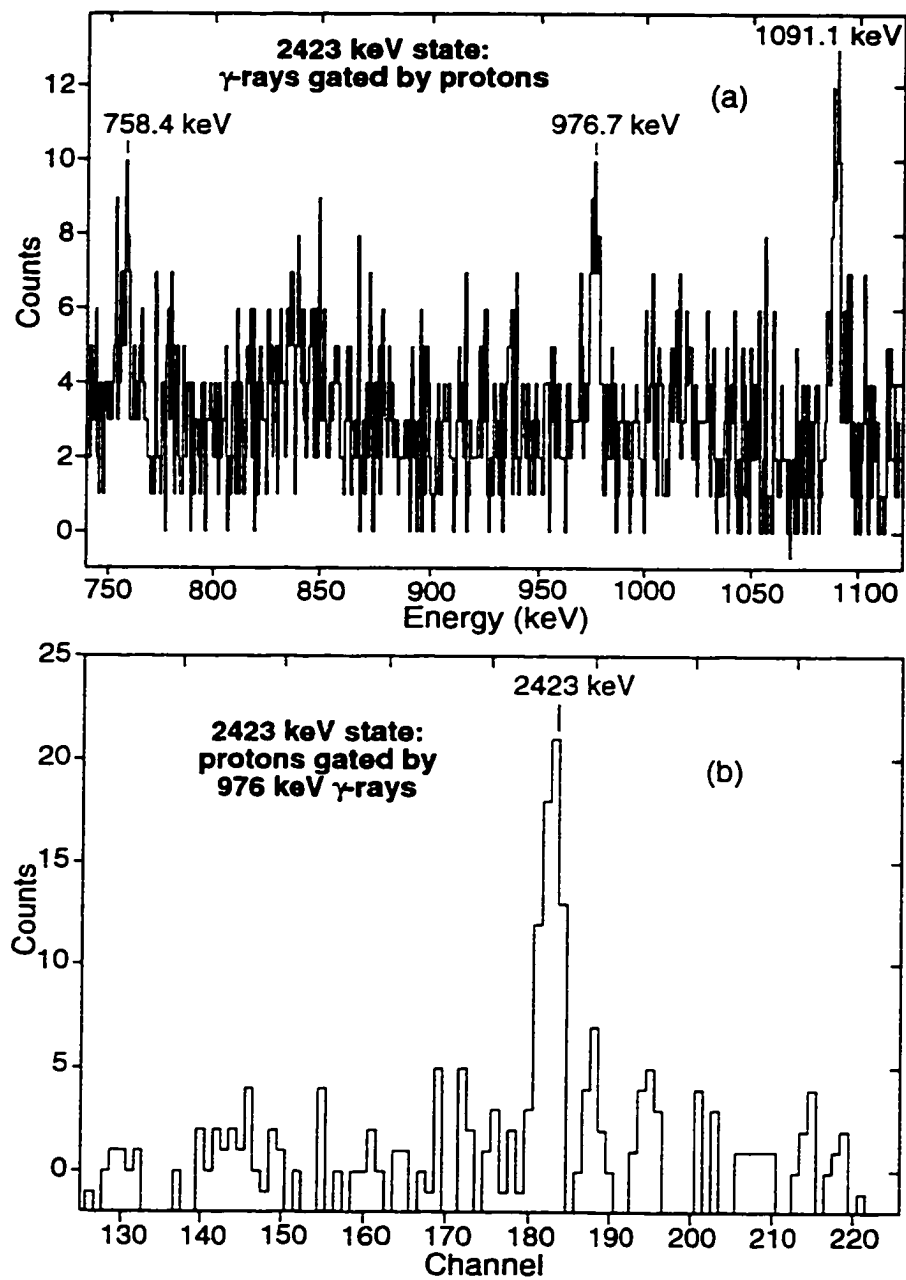


Figure 4.9: (a) γ -ray and (b) proton spectra showing the previously unreported decay from the 2423 keV state by a 976.7 keV γ -ray to the 3_1^- state. The subsequent decays from the 3_1^- state are also shown.

CHAPTER 5

DISCUSSION OF $^{196}\text{Pt}(p, p'\gamma)$ RESULTS

5.1 Octupole States in ^{196}Pt

Identification of an additional, higher-lying octupole state in ^{196}Pt lends considerable support to the argument made in Reference [Cot88b] for fragmentation of the low energy octupole state. The present study shows that the low energy octupole strength is shared by at least two states, at 1447 keV and 2423 keV. However, Cottle *et al.* proposed that three additional states (2608, 2638, and 2707 keV) seen in the 35 MeV $^{196}\text{Pt}(p, p')$ experiment [Dea81] also share a significant amount of the octupole strength. Since the proton angular distributions for these other three states are nearly identical to that of the identified 2423 keV 3_2^- state, it is highly probable that the other three states also have $J^\pi = 3^-$. We do not, however, have direct evidence for this from the present experiment.

There are several possible reasons why the other high-lying octupole states in ^{196}Pt at 2608, 2638, and 2707 keV proposed in Reference [Cot88b] were not observed in the present experiment. The assumption was made that the present experiment using 12.7 MeV protons would populate the same states seen in (p, p') by Deason *et al.* using 35 MeV protons [Dea81]. It may be, however, that the incident proton beam energy of 12.7 MeV used in the present experiment is too low to excite the higher-lying octupole states. There were no clearly identifiable states, octupole or any other type, populated at higher energy in the present experiment than the 3_2^- octupole state which was identified. Secondly, two of the proposed octupole states (the 2608 keV and the 2707 keV states) have smaller B(E3) values (2.1 and 3.2 W.u.

respectively) than that for the 2423 keV state (4.4 W.u.) [Cot88b] and are therefore more difficult to observe. Lastly, it is possible that the 2423 keV state was more isolated in the proton spectrum than the other proposed states. The γ -ray spectrum from these states would not be as clean, making the high energy de-excitations more difficult to see than the weak 2067 keV decay that was observed. The resolution of the proton spectrum was not sufficient to determine whether this was true.

A detailed search for γ -rays from the other proposed octupole states reported by DiPrete *et al.* [DiP93] to the 2_1^+ , 2_2^+ , 3_1^- , and 4_1^+ states was conducted by gating on the proton spectrum between 2.3 and 2.8 MeV and examining the resulting γ -ray spectra for the connecting transitions. Furthermore, γ -ray gates were set at the energies where the connecting transitions would occur, but no evidence of peak structure at the correct energies was seen in the resulting proton spectra.

5.2 Octupole States in Other Pt Isotopes

The observation of the 2423 keV state in ^{196}Pt is similar to a finding in a $^{198}\text{Pt}(p,p'\gamma)$ study of Yates *et al.* [Yat88]. They identified a state at 2603 keV which decayed to the 3_1^- state at 1680 keV, and proposed, based on the occurrence of this transition, that the 2603 keV level has $J^\pi = 3^-$. They associated this state with a 2611 keV state populated in the 35 MeV $^{198}\text{Pt}(p,p')$ reaction by Deason *et al.* [Dea81]. In a similar analysis to the one of ^{196}Pt , Cottle *et al.* [Cot88b] proposed five higher-lying octupole states seen in the 35 MeV $^{198}\text{Pt}(p,p')$ reaction based on proton angular distribution measurements. These states, too, have angular distributions nearly identical to the identified 3_2^- 2423 keV state in ^{196}Pt , and it is likely that they also have $J^\pi = 3^-$. If this is the case, it provides evidence for octupole fragmentation in ^{198}Pt as well as ^{196}Pt . Furthermore, Cottle *et al.* [Cot88b] proposed three higher-lying octupole states in ^{194}Pt having nearly identical proton angular distributions to the octupole states in ^{196}Pt , and fragmentation of the low

energy octupole state may be present in ^{194}Pt as well. Direct experimental evidence is needed, however, to confirm these suppositions.

The similarity between the scattered proton angular distributions indicate that all of the proposed states in $^{194,196,198}\text{Pt}$ may have $J^\pi = 3^-$. There remains, however, open discussion as to whether or not these states are collective octupole excitations. Yates *et al.* [Yat88] have suggested that the 3_1^- states in $^{194,196,198}\text{Pt}$ are not vibrational octupole states, but are instead composed of two-quasiparticle states coupled to rotational excitations. However, reported $B(E3; 0_{gs}^+ \rightarrow 3_1^-)$ values [Cot88a] derived from an analysis of the Deason *et al.* (p, p') data [Dea81] range from 6-9 W.u., indicating some degree of octupole collectivity for the states. The higher-lying 3^- states all have similar $B(E3)$ values, which yields a summed strength of ≈ 20 W.u. for each of the Pt isotopes. The reported $B(E3)$ values of Reference [Cot88a] are consistent with Coulomb excitation measurements for ^{194}Pt [Ron77].

Inelastic electron scattering measurements performed on ^{196}Pt by Ponomarev *et al.* [Pon92] also populate the three lowest 3^- states in ^{196}Pt at 1447 keV, 2431 keV, and 2638 keV. The authors assume collective excitations and assign $J^\pi = 3^-$ for the three states. The $B(E3)$ values they extracted from scattered electron angular distributions are identical, within error, to the $B(E3)$ values reported in Reference [Cot88a]. The values are given in Table 5.1. Although there may be some mixing from quasiparticle excitations, the 3^- states clearly show octupole collectivity.

Identical $B(E3)$ values from electron scattering, which probes the role of the protons, and from 35 MeV proton scattering, which primarily probes the neutron role, indicates that the amplitudes of the proton and neutron oscillations in the octupole vibrations are nearly equal. Identical proton and neutron oscillation amplitudes (that is, $\beta_n = \beta_p$) conforms to the simple isoscalar collective picture, and lends support to interpretation of these 3^- states as collective excitations.

The $J^\pi = 3^-$ assignments of Ponomarev *et al.* [Pon92] provide a spin assignment of the proposed octupole states in ^{196}Pt which is independent of other measurements. However, from their scattered electron angular distributions, Ponomarev *et al.* cannot identify exactly which states they have populated, and rely, instead, on previously reported energies from Deason *et al.* [Dea81]. We maintain that the superior energy resolution of γ -ray detection methods is the most reliable way of identifying these states, and that a coincidence experiment, such as ours, is required to make use of the existing γ -ray information to identify the precise energy of the 3^- states in ^{196}Pt .

Table 5.1: Comparison of the transition strengths of the three lowest energy 3^- states in ^{196}Pt from (p, p') and (e, e')

| ^{196}Pt | 1447 keV | 2423 keV | 2638 keV |
|-------------------|--------------------|--------------------|--------------------|
| (p, p') | 0.099(20) e^2b^3 | 0.070(14) e^2b^3 | 0.070(14) e^2b^3 |
| (e, e') | 0.111(11) e^2b^3 | 0.087(14) e^2b^3 | 0.072(13) e^2b^3 |

5.3 Mixed Symmetry States in ^{196}Pt

The observation of a state at 2246 keV in ^{196}Pt in the present experiment raises a point which has little relation to octupole fragmentation in the Pt isotopes. It is, however, interesting in its own right, and deserves discussion here. A recent report by von Brentano *et al.* [vonBre96] indicates the first possible observation of a mixed symmetry “scissors mode” state in a γ -soft nucleus, ^{196}Pt . The scissors mode is a vibrational mode in which the proton and neutron distributions oscillate with respect to one another in a scissors type of motion. The mode, characterized by strong M1 transitions to the ground and 2_1^+ states, has been observed in a number of well-deformed and spherical nuclei, but never before in a γ -soft nucleus. Using

nuclear resonance fluorescence, von Brentano *et al.* observed ten states between 2.2 and 3.5 MeV and suggested that these states may have $J^\pi = 1^+$ and are fragments of the scissors mode state. The observation of the 2246 keV state in the present experiment indicates that the spin is more likely $J^\pi = 2^+$.

Excitation by a photon type mechanism, such as nuclear resonance fluorescence, brings a very small amount of angular momentum to the reaction and thereby selects only $J = 1, 2$ states. On the basis of their measured branching ratios and excitation strengths, von Brentano *et al.* report that a 1^+ spin assignment is most favored for the 2246 keV state. The $^{196}\text{Pt}(p, p'\gamma)$ reaction of the present experiment is also highly selective, however, with no known mechanism for strongly exciting a 1^+ state [Car85a, Dja85, Pet86].

The electromagnetic M1 operator has both spin and orbital components, which give rise to, respectively, the usual "spin" type excitation and a mixed symmetry orbital or "current" (the scissors mode) excitation. As noted in References [Car85a, Dja85], the cross section for exciting a purely orbital mixed symmetry 1^+ state with inelastic scattering of protons below 200 MeV is vanishingly small. In fact, as pointed out in Reference [Pet86], even the usual "spin" type 1^+ states are unlikely to be populated with 12.7 MeV protons. This appears to be true as no other 1^+ states were observed in the present experiment. Observation of the 2246 keV state in the present experiment, then, supports a $J^\pi = 2^+$ assignment. Assigning $J^\pi = 2^+$ to the 2246 keV state in no way contradicts the assertion of von Brentano *et al.* for their observation of the first scissors mode state in a γ -soft nucleus; it simply indicates that the 2246 keV state is not one of the fragments of the 1^+ scissors mode state.

There exists the possibility that the 2246 keV state may still be a mixed symmetry excitation. Iachello [Iac84] predicted that the lowest mixed symmetry state in an O(6) nucleus, of which ^{196}Pt is the best known example, would have $J^\pi = 2^+$ and a large E2 transition to the ground state. This is consistent with what was seen in the

present experiment. With the exception of the 2_1^+ state, the fully symmetric states in an $O(6)$ nucleus are not predicted by Iachello to have significant E2 transitions to the ground state. The E2 transition strength for the 2246 keV state decaying to the ground state is 2.6 W.u. (from width measured by von Brentano *et al.* [vonBre96]), making this state a likely candidate for the 2^+ mixed symmetry excitation.

CHAPTER 6

THEORETICAL OVERVIEW FOR $0_{gs}^+ \rightarrow 2_1^+$ TRANSITION IN ^{20}O

As was discussed in Chapter 2, the bulk of nuclear behavior exhibits properties of both the idealized pictures of the shell model and the collective model. While the data on 2_1^+ states in some of the nuclei of the $12 \leq A \leq 26$ mass region suggest collective interpretations, our conclusions indicate that the shell structure has a strong effect on the behavior of the $0_{gs}^+ \rightarrow 2_1^+$ transition.

6.1 Structure of First Excited States in the $12 \leq A \leq 26$ Mass Region

The two most common descriptions of macroscopic collective behavior are as rotational and vibrational excitations. Collective 2_1^+ states, the primary concern of this chapter, can be easily described by both types. Rotational and vibrational behavior is usually distinguished experimentally by the systematic spacing of energy levels corresponding to successive quanta of vibrational or rotational excitation. Figure 6.1 shows typical energy level spacings for vibrational and rotational behavior. While some nuclei in the $12 \leq A \leq 26$ mass region clearly exhibit rotational behavior, such as $^{20,22}\text{Ne}$ and $^{24,26}\text{Mg}$, the known energy levels of ^{20}O , shown in Figure 6.2, suggest vibrational behavior in this nucleus. In particular, the energies of the 2_1^+ and 4_1^+ states in ^{20}O are very near the harmonic vibrational limit, with $E(4_1^+)/E(2_1^+) = 2.18$. Elliott *et al.* have pointed out that the energy spectrum of ^{20}O indicates vibrational behavior, while that of the neighboring nucleus, ^{20}Ne , is interpreted to be rotational in their IBM treatment of $A = 20$ nuclei [Eli80]. Because of the nearly equal energy level spacing, and since stable nuclear deformation

generally only occurs in the ground state when a nucleus has both protons and neutrons in the valence shells [Cas81], we choose to model the 2_1^+ state of the singly closed shell nucleus ^{20}O as a quadrupole vibrational state.

Vibrational excitations occur in energy quanta of a given multipole order known as vibrational phonons. The multipole order also determines the angular momentum quanta carried by the vibrational phonon. In the case of a quadrupole vibration, the angular momentum of the excited phonon is $2\hbar$. Phonons of the same or different multiplicities can couple to each other, producing multiplets of excited states. An example of this is shown in Figure 6.1, where quadrupole phonons are coupled to produce multiplets of degenerate positive parity states. In physical cases, the degeneracy of the multiplets is broken because of residual interactions between the phonons. Phonon-phonon interactions also account for the deviations from a perfectly harmonic level spacing.

From a microscopic point of view, vibrational excitations are coherent superpositions of quasiparticle excitations. However, in the $A < 40$ mass region, there are relatively few single-particle configurations available with which to build vibrational excitation modes. In spite of this, many of these nuclei still exhibit the enhanced transition probabilities characteristic of collective behavior. Due to the low binding energy of these nuclei, (^{20}O , for example, has a neutron separation energy of 7.6 MeV) the number of excited states is oftentimes not sufficient to clearly determine whether the collectivity is vibrational or rotational based on energy level spacing (see Figure 6.2). The coupled channels approach we have used to analyze the scattered proton angular distributions for the ground state and 2_1^+ state in ^{20}O is not very sensitive to the choice of a vibrational or rotational model. The coupled channels calculations were performed for both models for ^{20}Ne , with very little difference to the results whether the quadrupole deformation was treated as dynamic or static.

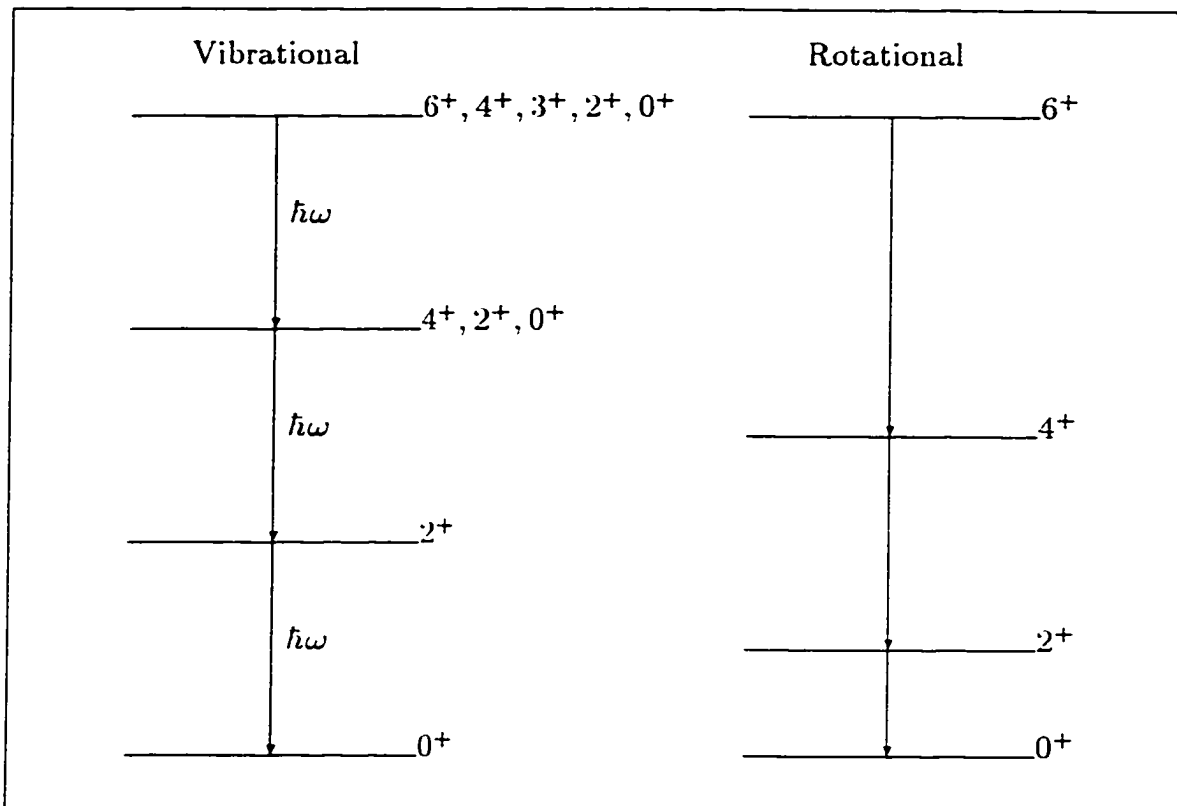


Figure 6.1: Typical energy level spacings from vibrational and rotational collective behavior

We have therefore chosen, in the present analysis, to model the 2_1^+ state in ^{20}O as a vibrational collective excitation, following the interpretation of Elliott *et al.* [Eli80].

Although there is no attempt in the present work to describe the nuclear behavior microscopically in an explicit way, the shell model is very useful in understanding collective excitations in the $12 \leq A \leq 26$ mass region. Shell model descriptions typically treat closed shells as inert cores which contribute little to the excitation, and only the valence nucleons outside of closed shells are free to populate higher orbitals. To quantify the isospin behavior, the isospin quantum number T and its projection onto an arbitrary isospin symmetry axis T_z are used. The ground state isospin for even-even nuclei is the minimum value allowed for a given $T_z = 1/2(Z - N)$

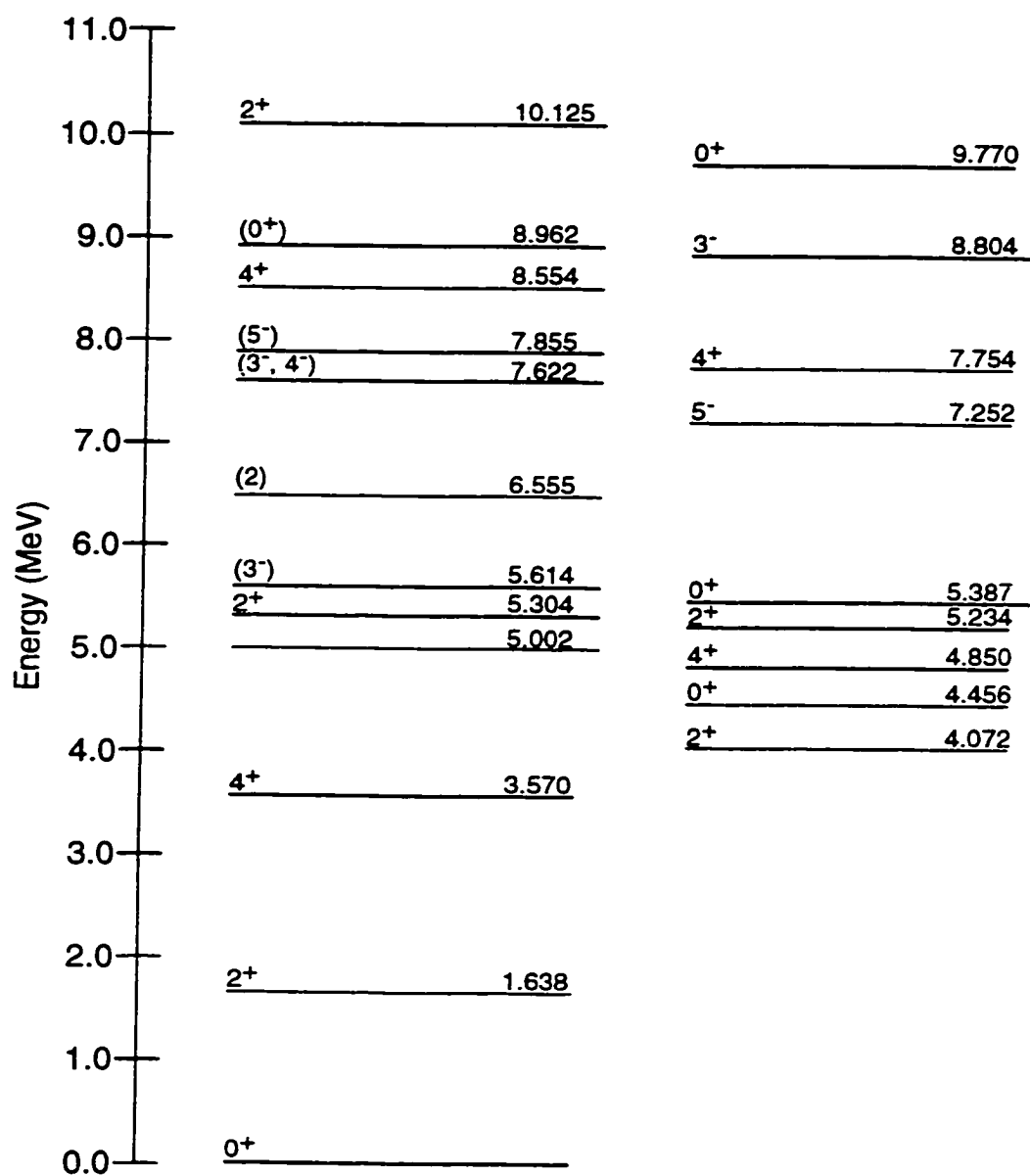


Figure 6.2: Known energy levels in ^{20}O .

projection. Any transition with $\Delta T = 0$ is purely isoscalar, and any with $\Delta T = 1$ is purely isovector. Oftentimes, though, a transition will have both isoscalar and isovector components.

The choice of a particular nuclear model can make a huge difference in predicting relative neutron and proton contributions in these transitions. In the simplest shell model picture, vibrations consist solely of valence nucleon excitations. Vibrations in a nucleus with a closed proton shell, like ^{20}O for example, are viewed as entirely due to the valence neutrons. The ratio of neutron to proton transition matrix elements M_n/M_p for this transition would be infinite in this example, and the vibration would be exclusively from neutron excitations. The isoscalar and isovector transition matrix elements, M_0 and M_1 respectively, are related to the proton and neutron transition matrix elements by

$$\begin{aligned} M_0 &= M_p + M_n \\ M_1 &= M_p - M_n, \end{aligned} \tag{6.1}$$

although other sign conventions are used [Ber79, Bro82, Pet93]. In the simplest collective picture, however, the nucleus is thought of as a homogeneous neutron-proton fluid with the protons and neutrons oscillating with equal amplitudes. In the example of ^{20}O just used, the same transition which gave $M_n/M_p = \infty$ in the simplest shell model, would give $M_n/M_p = N/Z$ in the simplest collective model. The participation of excitations of the core nucleons, known as core polarization, resolves to some extent, the drastic discrepancy between these two pictures [Bro75, Bro80, Bro82].

In a more realistic shell model, the closed shell core is not entirely inert, and the participation of core nucleon excitations serves to reduce M_n/M_p from infinity in singly closed proton shell nuclei and increase M_n/M_p from zero in singly closed neutron shell nuclei for the $0_{gs} \rightarrow 2_1^+$ transition [Ber83]. The magnitude of the core

polarization is always greater for the core nucleon type which is unlike the valence nucleon type because the residual interaction between unlike nucleons is stronger than that between like nucleons [Ber81, Ber83]. Although low-lying collective 2_1^+ states are primarily composed of $0\hbar\omega$ excitations from the valence nucleons, higher-lying $1\hbar\omega$ and $2\hbar\omega$ excitations of the core contribute to the excitation [Ber83]. The degree of mixing between core nucleon excitations and valence nucleon excitations is quantified in shell model treatments by introducing core polarization parameters which connect the proton and neutron transition matrix elements A_p and A_n in the shell model valence space with the full transition matrix elements M_p and M_n . M_p and M_n can be defined as

$$\begin{aligned} M_p &= A_p(1 + \epsilon_{pp}) + A_n\epsilon_{pn} \\ M_n &= A_n(1 + \epsilon_{nn}) + A_p\epsilon_{np} \end{aligned} \quad (6.2)$$

where ϵ_{ab} signify the strength of the coupling between valence nucleons b and the core nucleons a [Bro82].

A systematic coupling scheme has been used by Bernstein *et al.* [Ber81] to set the core polarization parameters so that the experimental energies of the isoscalar and isovector giant quadrupole resonances are reproduced. Their scheme reproduces extracted ratios of transition matrix elements, M_n/M_p , for $0_{gs}^+ \rightarrow 2^+$ transitions in singly closed shell nuclei between $18 \leq A \leq 208$. The same scheme has been extended by Madsen and Brown [Mad84] to include open shell nuclei between $N = 50$ and $N = 82$. Brown *et al.* [Bro82] have also performed shell model calculations for 2_1^+ states in selected $8 \leq A \leq 20$ nuclei, although only a few calculations exist for nuclei away from stability. Their calculations for nuclei close to stability assume an inert ^{16}O core with $n = A - 16$ valence nucleons in a complete $0d_{5/2}, 1s_{1/2}, 0d_{3/2}$ basis of Chung and Wildenthal [Bro80b], notated as $(sd)^n$. The results from the calculations of Brown *et al.* [Bro82] will be discussed in Chapter 9. Brown *et al.*

[Bro82] concede that their calculations are somewhat model dependent, and they point specifically to their assumption of harmonic oscillator radial wave functions.

6.2 Probe Sensitivity

To investigate differences between proton and neutron contributions it is often necessary to use two independent experimental probes, one sensitive to neutrons and one sensitive to protons. With the exception of electromagnetic (EM) probes, which interact with the protons only, every probe has its own unique interaction with both protons and neutrons. Thus, different probes have a variety of sensitivities to the neutron contribution relative to the proton contribution of the $0_{gs}^+ \rightarrow 2_1^+$ transition. Each probe, therefore, measures a mixture of the transition matrix elements M_n and M_p [Ber81]. If the relative sensitivity of the probe to neutron and proton contributions is known, however, the transition operator $O_{\lambda\mu}^F$ can be decomposed into neutron and proton operators such as

$$O_{\lambda\mu}^F = b_n^F O_{\lambda\mu}^{Fn} + b_p^F O_{\lambda\mu}^{Fp}, \quad (6.3)$$

where b_n^F and b_p^F are the neutron and proton external field strengths for a given probe F . The multipole matrix element measured by a given probe is then

$$\begin{aligned} M_F &= \langle \nu_f J_f T_Z A || O_{\lambda}^F || \nu_i J_i T_Z A \rangle \\ &= b_n^F M_n + b_p^F M_p. \end{aligned} \quad (6.4)$$

For two different probes F and G having different neutron and proton sensitivities, M_n and M_p can be extracted from M_F and M_G .

In the case of scattering probes, with which the present work is concerned, the extraction is typically done by relating the transition matrix element of a given probe to the RMS multipole deformation length $\delta_{\lambda}^F = r_{\lambda}^F \beta_{\lambda}^F$. δ_{λ}^F is experimentally obtainable by a coupled channels or folding model analysis of the elastic and inelastic

differential cross sections. The mean radius r_λ^F depends on the particular probe, and the β_λ^F are RMS deformation parameters which correspond to the multipole order expansion of the nuclear surface R in Equation 1.1. Just as the matrix element M_F for a given probe is decomposed into neutron and proton components, so is the RMS deformation length as

$$\delta_\lambda^F = \frac{b_n^p N \delta_\lambda^n + b_p^p Z \delta_\lambda^p}{b_n^p N + b_p^p Z}. \quad (6.5)$$

The ratio of neutron to proton transition matrix elements as measured by two different probes F and G is then

$$\frac{M_n}{M_p} = \frac{N \delta_\lambda^n}{Z \delta_\lambda^p}. \quad (6.6)$$

Bernstein *et al.* [Ber81] have compiled approximate sensitivity ratios b_n^F/b_p^F for various experimental probes in specific energy ranges which allow us to use the explicit form of Equation 6.5 to obtain

$$\frac{M_n}{M_p} = \frac{\epsilon_G^F \frac{\delta_\lambda^F}{\delta_\lambda^G} - 1}{\frac{b_n^F}{b_p^F} - \frac{b_n^G}{b_p^G} \epsilon_G^F \frac{\delta_\lambda^F}{\delta_\lambda^G}} \quad (6.7)$$

where

$$\epsilon_G^F = \frac{1 + \frac{N b_n^F}{Z b_p^F}}{1 + \frac{N b_n^G}{Z b_p^G}}. \quad (6.8)$$

M_n/M_p values which incorporate these sensitivity parameters are consistent among the experimental probes to within 15% [Ber81] over a mass range of $18 \leq A \leq 208$. The b_n^F/b_p^F ratios listed by Bernstein *et al.* are given in Table 6.1.

For the present work, which focuses on inelastic proton scattering, the ratio b_n^N/b_p^N is derived from phenomenological optical model potentials for elastic nucleon scattering. The treatment, taken from Satchler [Sat83], is general for any type of nucleon scattering in a 10-50 MeV energy range. A general optical potential V_N for elastic nucleon scattering can be given by the Lane potential [Sat64, Mad75], and written in terms of isoscalar and isovector components as

$$V_N = V_0 + V_1 \frac{4}{A} \vec{\tau} \cdot \vec{T} \quad (6.9)$$

Table 6.1: Ratios of neutron to proton sensitivity of various probes. [Ber81]

| Probe (F) | Energy [MeV] | b_n^F/b_p^F |
|---------------------|--------------|-----------------------|
| EM | – | 0 |
| (p, p') | 10 - 50 | ≈ 3 |
| (n, n') | 10 - 50 | $\approx \frac{1}{3}$ |
| $(\pi^+, \pi^{+'})$ | 160 - 200 | $\approx \frac{1}{3}$ |
| $(\pi^-, \pi^{-'})$ | 160 - 200 | ≈ 3 |
| (p, p') | 800 | 0.83 |
| (p, p') | 1000 | 0.95 |
| (α, α') | All | 1 |

with $\vec{\tau}$ and \vec{T} as the respective isospin operators for the incident nucleon and target nucleus, and V_0 and V_1 respectively containing the isoscalar and isovector potential form factors and well depths. Using the isospin projections, $\tau_z = \frac{1}{2}$ for protons and $\tau_z = -\frac{1}{2}$ for neutrons, we can specify the nucleon scattering potential V_N for neutron and proton scattering as

$$V_p = V_0 + V_1 \frac{(N - Z)}{A} \quad (6.10)$$

$$V_n = V_0 - V_1 \frac{(N - Z)}{A}. \quad (6.11)$$

The potential simplifies with the assumption of identical form factors for the isoscalar and isovector components, and the assumption that the ratios of real to imaginary parts of V_0 and V_1 are identical. An additional assumption must be made about the ratio of isoscalar to isovector potential strength V_0/V_1 . The existence of the deuteron, and the absence of a bound neutron-neutron or proton-proton state, indicates that the isoscalar potential is considerably stronger than the isovector. A lower limit of $V_0/V_1 = -3$ is made by neglecting odd relative angular momentum interactions [Car85b]. However, more realistic potentials give the value $V_0/V_1 = -2$

[Car85b, Ber81, Mad75]. Using the more realistic estimate of $V_0/V_1 = -2$ gives the probe sensitivity to protons and neutrons as the coefficients of N and Z from proton scattering,

$$\begin{aligned} V_p &\approx V_0 \left[1 + \frac{(N - Z)}{2A} \right] \\ &\approx \frac{V_0}{2A} (3N + Z), \end{aligned} \quad (6.12)$$

and from neutron scattering,

$$\begin{aligned} V_n &\approx V_0 \left[1 - \frac{(N - Z)}{2A} \right] \\ &\approx \frac{V_0}{2A} (N + 3Z). \end{aligned} \quad (6.13)$$

The N and Z coefficients show that proton scattering is a factor of three more sensitive to the neutron distribution ($b_n^{(p,p')} = 3$, $b_p^{(p,p')} = 1$), and that neutron scattering is a factor of three more sensitive to the proton distribution ($b_n^{(n,n')} = 1$, $b_p^{(n,n')} = 3$). Ratios of b_n^F/b_p^F are given in Table 6.1.

Table 6.1 also lists probe sensitivities for pion scattering (π^+ , π^-) between 160-200 MeV, an independent method of extracting the M_n/M_p . The pion scattering method is used in the present work as a comparison of the experimental method and is discussed in Chapter 9.

6.3 Coupled Channels Calculations

As was mentioned in the preceding sections, the dynamic, RMS quadrupole deformation parameter β_2 is usually extracted from a measured angular distribution by means of a coupled channels or folding model analysis. We have chosen, for the $0_{g.s.}^+ \rightarrow 2_1^+$ transition in ^{20}O , to extract β_2 from the elastic and inelastic proton scattering angular distributions by way of a coupled channels calculation. The computer code CHUCK [Kunz] was used for this purpose. CHUCK performs a

numerical integration to simultaneously solve a set of n coupled equations of the form

$$\left[\frac{d^2}{dr_c^2} - \frac{l_c(l_c + 1)}{r_c^2} + (k_c^2 - U_{cc}) \right] \chi_{j_c l_c}^J(k_c; r_c) = \sum_{c' \neq c} \frac{2\mu_c}{\hbar^2} U'_{cc'} \chi_{j_{c'} l_{c'}}^J(k_{c'}; r_{c'}), \quad (6.14)$$

where $\chi_{j_c l_c}^J(k_c; r_c)$ are the available channel wavefunctions describing the relative motion of the projectile and the target with reduced mass μ_c for a given channel c by the relative coordinates \vec{r}_c and wavenumber k_c . The diagonal and off-diagonal terms of the optical potential are denoted by U_{cc} and $U'_{cc'}$, respectively. The channel wavefunctions are found by a partial wave expansion of the allowed orbital angular momenta l_c of the projectile about the target. The total angular momentum J is the sum of the orbital angular momentum, l_c , and the intrinsic moments of inertia s_c and I_c of the projectile and the target respectively, with the coupling scheme $\vec{j}_c = \vec{l}_c + \vec{s}_c$ for every allowed channel c . γ_c is the reduced mass of the projectile and target system. The full potential consists of both diagonal terms, U_{cc} , and off diagonal terms, $U'_{cc'}$. U_{cc} is a many-component optical potential based on an optical model analysis of elastic cross sections, while $U'_{cc'}$ is a coupling term describing the effective interaction for transitions between channels c and c' . The code CHUCK allows for user-defined nuclear potentials, as well as the Coloumb interaction for both U_{cc} and $U'_{cc'}$. The details of the potential forms used in the present analysis, as well as the potential well depths, is given in Chapter 8.

CHUCK produces a physically meaningful solution with the application of two boundary conditions, one at the origin of the projectile and target system, and one at the far field range of the Coloumb interaction. In general, the solution is a linear combination of the independent n solutions of the coupled equations. The output from CHUCK can be directed to give an angular distribution for all included channels in the center of mass of the projectile and target system, providing a comparison to the observed experimental angular distribution. In the present

analysis, β_2 is used as a user-defined coupling parameter which best reproduces the experimentally observed angular distribution.

CHAPTER 7

ANGULAR DISTRIBUTION MEASUREMENT FOR ^{20}O

An experiment to measure the angular distribution of protons scattered from the radioactive beam ^{20}O in inverse kinematics was performed at the National Superconducting Cyclotron Laboratory of Michigan State University. Protons from 1.6 mg/cm² and 3.3 mg/cm² polypropylene targets were scattered from a 30 MeV/A beam of ^{20}O . The polypropylene targets provide a source of protons from which the ^{20}O beam is scattered. The inverse kinematics experiment is equivalent to performing 30 MeV proton scattering from a target of ^{20}O .

7.1 Beam Production

The present $p(^{20}\text{O},p)^{20}\text{O}^*$ experiment was performed at the National Superconducting Cyclotron Laboratory, one of the few facilities equipped to deliver high intensity, high energy radioactive beams. A layout of the laboratory, including the K1200 cyclotron, the A1200 mass fragment separator, and the S2 experimental vault, is shown in Figure 7.1. Radioactive beams at the NSCL are produced by means of particle fragmentation.

A primary stable beam of ^{22}Ne was produced in an electron cyclotron resonance (ECR) ion source and injected into the K1200 cyclotron. There the primary beam was accelerated to an energy of 65 MeV/A and steered into the entrance of the A1200 mass fragment separator [She91]. The primary beam collided with a 360 mg/cm² water-cooled ^9Be target positioned at the entrance of the A1200, shown in Figure 7.2.

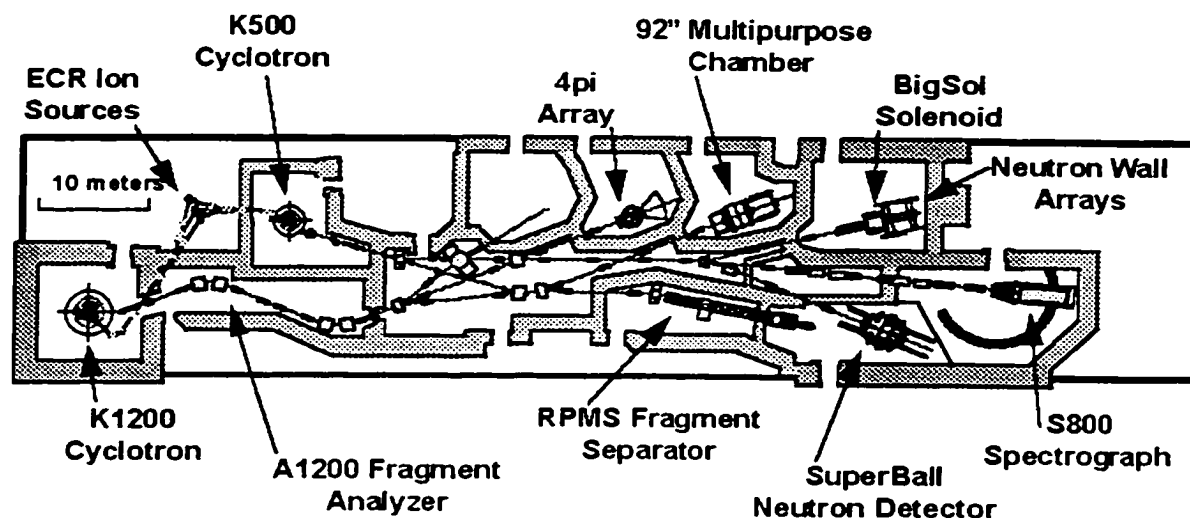


Figure 7.1: The layout of the NSCL experimental facility. The figure shows the K1200 cyclotron where the primary beam is accelerated, the A1200 mass fragment separator for production and selection of the radioactive secondary beam, and the S2 experimental vault at the tail end of the RPMS fragment separator where the $p(^{20}\text{O},p)^{20}\text{O}$ scattering experiment was performed.

The primary beam fragmented upon impact with the ^9Be target into a near continuum of both stable and unstable nuclei. The nucleus used as a secondary beam, in this case the radioactive beam ^{20}O , was selected in the A1200 by time of flight and energy loss characteristics. Degrading wedges placed at the dispersive image of the A1200 allowed isotope separation. For the present experiment, a 1% momentum acceptance was allowed by the placement of a 1.9 mrad ^{12}C degrading wedge at the second dispersive image position. Owing to the high initial beam energy, no re-acceleration of the secondary beam was required. The secondary beam

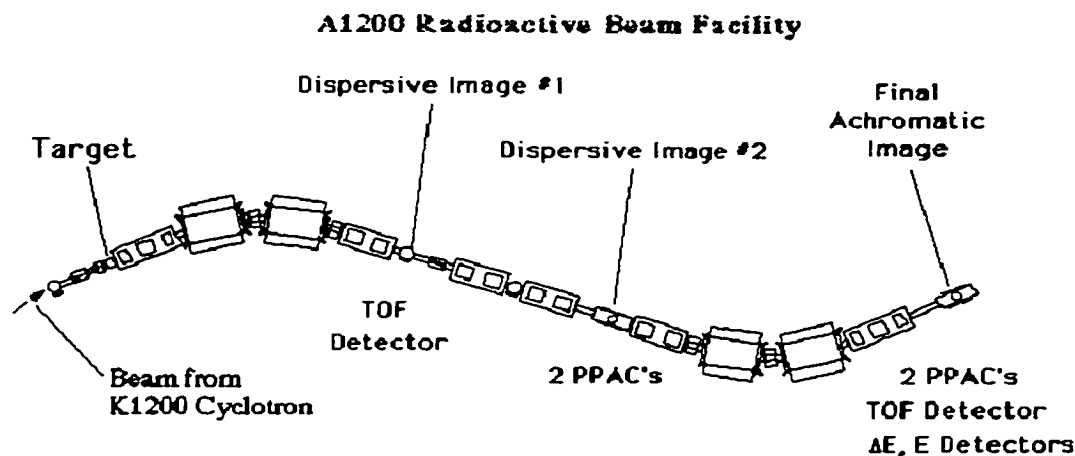


Figure 7.2: A1200 mass fragment separator at the NSCL. The A1200 is used to identify and select secondary beams after fragmentation of the primary beam.

^{20}O was produced at 30 MeV/A. The beam was nearly 99% pure, and yielded roughly 30,000 particles/second (pps) on target.

7.2 Experimental Details

7.2.1 Beam Tracking and Identification

The secondary beam was tracked by two position sensitive parallel-plate avalanche counters (PPACS) [Swa94] placed at 1 m and 2 m upstream of the target position. The PPAC positions, along with a schematic of the other detector positions, can be seen in Figure 7.3. The PPACS provide accurate position sensitivity in two dimensions over a $10 \times 10 \text{ cm}^2$ active area. Low pressure iso-octane gas constrained between two sheets of mylar provided an ionization read out by 0.4 mg/cm^2 aluminized polyester and polypropylene electrodes affixed to each mylar sheet. Two independent read outs were made for each of the two position dimensions so that a simple charge division determined the position. Fast preamplifiers capable of count

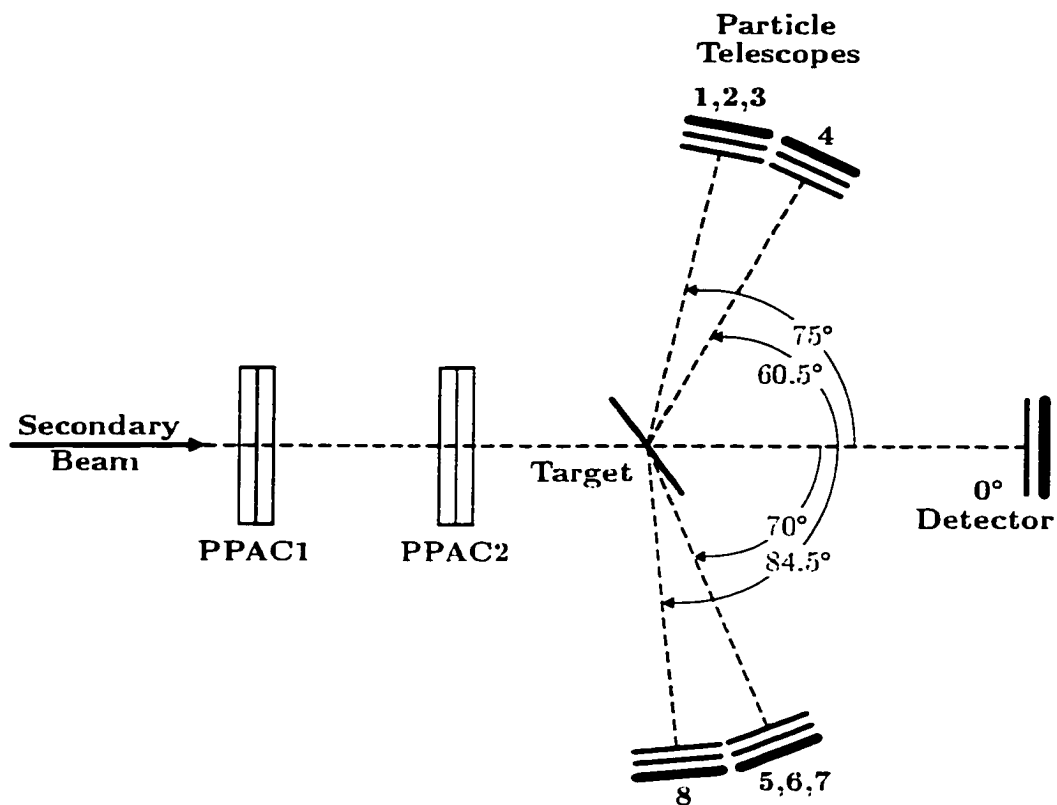


Figure 7.3: Schematic of the experimental arrangement.

rates up to 5×10^4 events/second were used. Initial position calibration measurements were taken with an α source and a mask placed over the PPAC front surface. The mask was a square grid of 2 mm diameter holes spaced 1 cm apart. A position resolution of 1 mm was observed from this calibration. A subsequent in-beam calibration was performed which confirmed the resolution and alignment of the PPACs on the optical beam axis.

The beam was stopped by a fast/slow plastic phoswich placed at a zero degree forward scattering angle 1 m downstream of the target position. The zero degree detector had an angular acceptance of 2.5 degrees which was sufficient to detect the

entire angular scattering of the ^{20}O beam. $\Delta E - E$ energy loss measurements made from comparing the fast and slow zero degree detector signals allowed a moderate degree of beam identification based on mass and charge number. The high purity (99 %) of the secondary beam, however, made this feature somewhat unnecessary. For further identification, the zero degree detector was also used to record the time of flight (TOF) of beam particles. A PIN diode located at the A1200 exit provided the start of the time of flight measurement. Count rates up to 200,000 pps were possible with the zero degree detector. Sample $\Delta E - E$ and TOF plots showing the high beam purity are given in Figure 7.4.

7.2.2 FSU-MSU Charged-Particle Telescope Array

A charged particle telescope array consisting of 8 three stage Si strip-Si PIN-CsI particle telescopes was used to detect scattered protons. Each stage of the telescopes has a $5 \times 5 \text{ cm}^2$ active area. The first stage of the telescope is a $300 \mu\text{m}$ thick position sensitive Si strip detector. The detector face is segmented into 16 individual strips, 3 mm in width, which are read out individually. A $500 \mu\text{m}$ thick PIN diode makes up the second telescope stage, and a 1 cm thick CsI scintillator composes the last stage. Four separate photodiodes attached to the CsI crystal by a clear RTV epoxy were used to collect light from the scintillator. The multi-stage telescope provides not only a means for angular distribution measurements, which could just as easily be done with a single-layer position sensitive detector, but also a means for particle identification. Particles fully stopped in the Si strip detector were identified by time of flight. Higher energy particles which penetrate into two or more layers of the detector were identified by $\Delta E - E$ measurements between the different telescope layers. The various means of particle identification allows filtering of deuterons and alpha particles from the collected data.

Preamplifiers for the PIN diodes and CsI detectors were placed inside the scattering chamber to reduce noise in the signals. Due to the many distinct channels

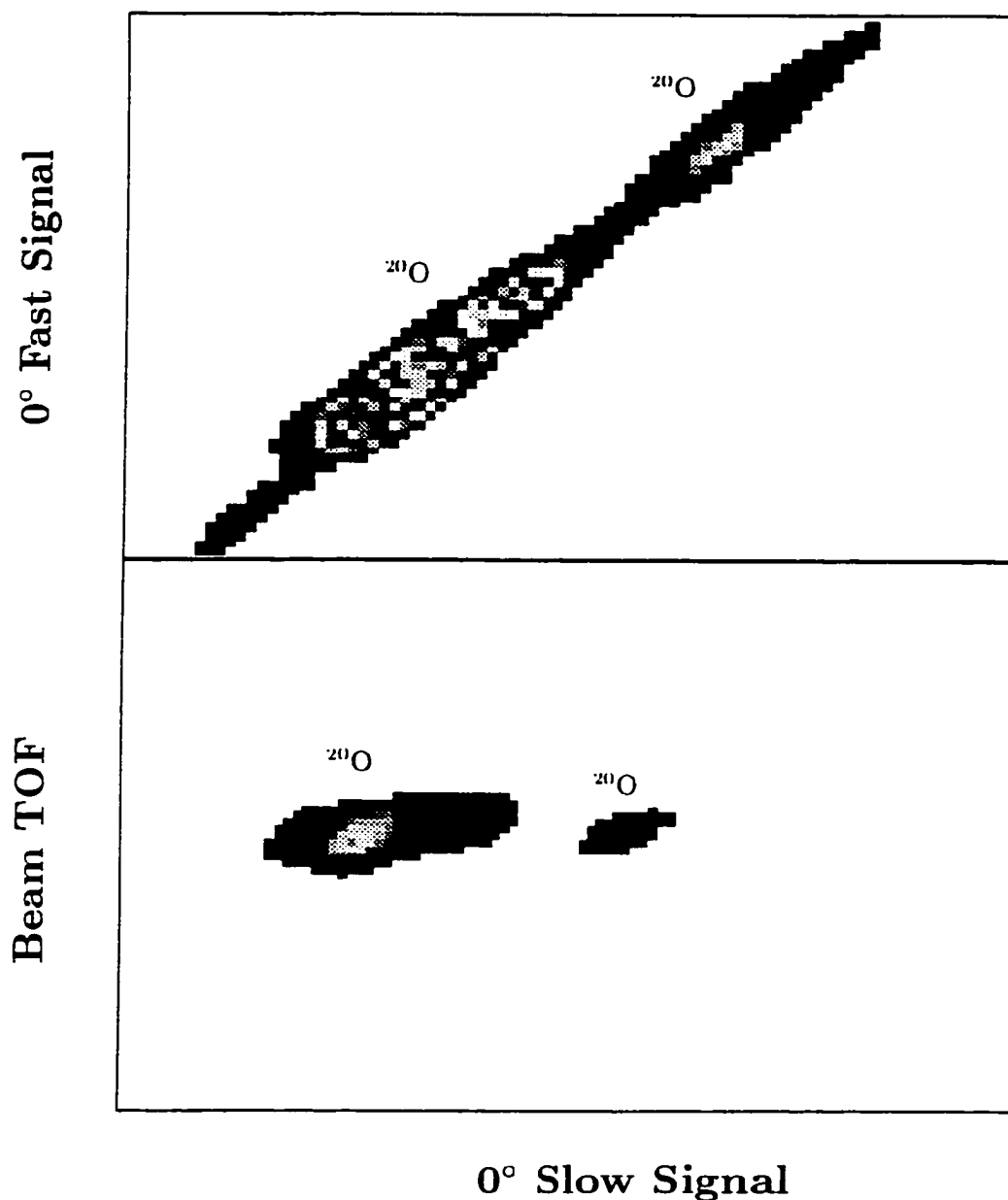


Figure 7.4: Sample $\Delta E - E$ and TOF zero degree detector spectra showing the high purity of the beam. The top plot is the energy loss in the fast plastic versus the energy in the slow plastic. Only a single isotope (^{20}O) can be seen. The bottom plot is the beam TOF between the A1200 exit and the zero degree detector. The spreading of the characteristic energy loss point is caused by an unstable power supply producing fluctuations in the detector bias voltage

required by the Si strip detectors, it was not practical to house the Si strip preamplifiers inside the scattering chamber. Those preamplifiers were instead located just outside of the chamber. The placement of the Si strip detector preamplifiers outside the chamber led to a large increase in noise to the signals, requiring noise threshold settings close to 1 MeV. The PIN diode thresholds, on the other hand, were around 250 keV. All of the preamplifiers used with the charged-particle telescope array were built at the NSCL.

The physical positioning of the telescopes was done so that the Si strips lie tangent to circles of constant scattering angle. The scattering angle is measured in the laboratory frame with respect to a coordinate system having its origin at the target and z-axis coinciding with the optical beamline axis. Each telescope is mounted on one of two vertical bars by an aluminum wedge which aligns each strip along a constant scattering angle. Figure 7.5 (as well as Figure 7.3) illustrates the telescope array positioning. The telescopes were mounted 28 cm from the target position in the present experiment. At this position, each telescope could detect an angular range of 10° , with each individual strip seeing a range of 0.6° in the laboratory frame. Due to the strips not being curved to match the constant scattering angular curves, and due to a large area of the target being illuminated by the beam, each strip actually detected a range of about 0.85° , thereby introducing a modest amount of uncertainty in the overall angular resolution.

Two major concerns were taken into account in choosing the scattering angles at which to place the telescopes. First, the angular range must cover a region where both elastically and inelastically scattered protons are expected from a kinematics calculation, and where they are well separated in energy. Secondly, the angles chosen must be in a region for which the scattering cross section is reasonably high. Additionally, the array as a whole must cover a large enough angular range to yield a multi-point angular distribution. To meet these criteria, three of the telescopes

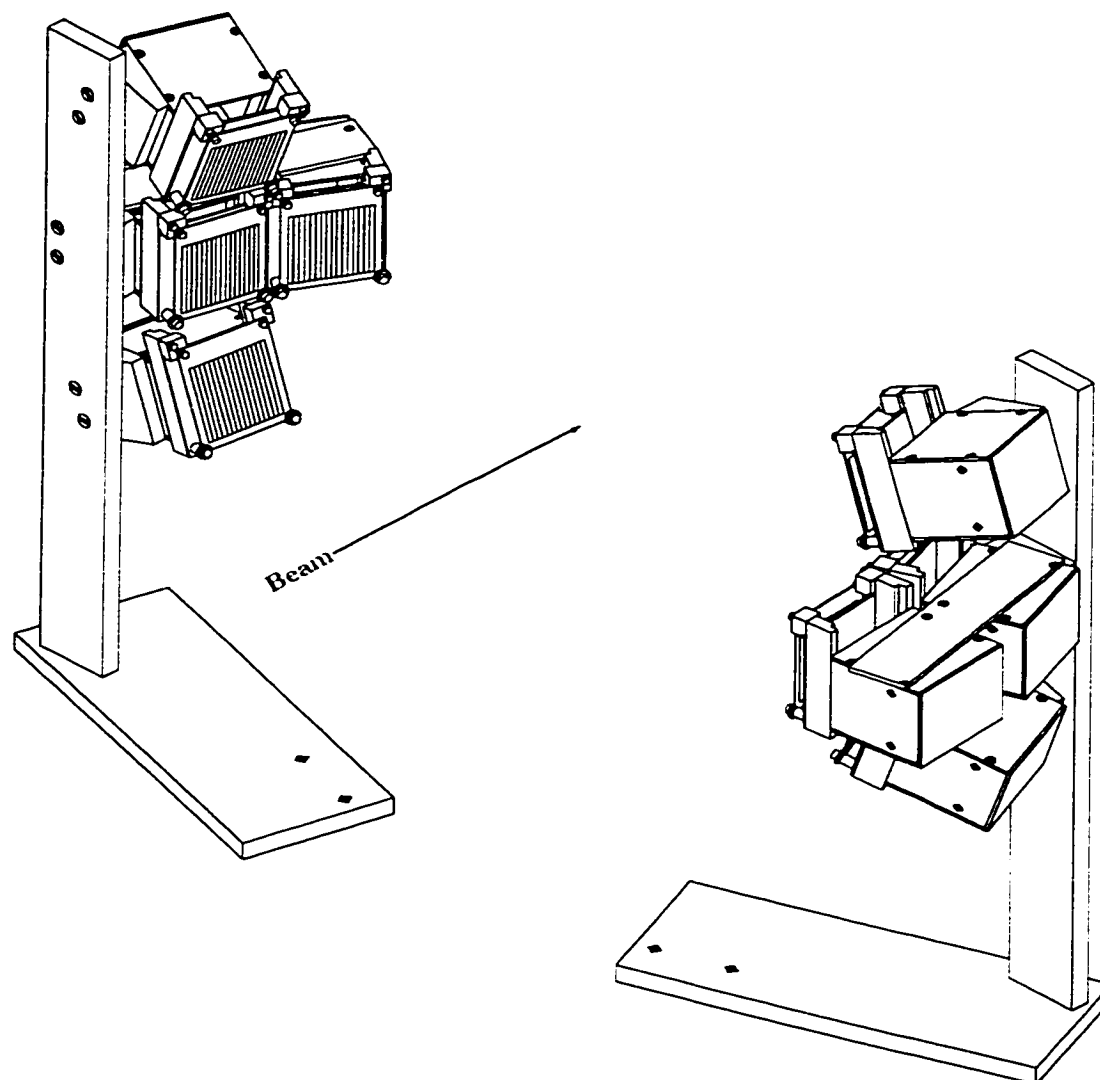


Figure 7.5: Positioning of the FSU-MSU charged particle telescope array. Each telescope is a three stage detector consisting of a position sensitive Si strip detector, a PIN diode, and a CsI scintillator. Telescopes 1,2 and 3, on the left side, are centered at 75° with respect to the beam axis, and telescope 4 is at 60.5° . On the right, telescopes 5,6 and 7 are centered at 70° , and telescope 8 is at 84.5° .

were centered at 70° on one side of the target, three more were centered at 75° on the other side, and the remaining two telescopes were centered at 84.5° and 60.5° . Even without the use of the detectors at 84.5° and 60.5° , which proved unreliable due to electronics difficulties, measurement over a range of $65^\circ - 82^\circ$ in the laboratory frame was possible. This corresponds to an angular range of roughly $20^\circ - 45^\circ$ in the center of mass frame.

7.3 Electronics

A diagram showing the electronics used for beam tracking and identification is shown in Figure 7.6. Each of the two PPAC detectors provides four signals corresponding to left, right, up, and down for determining the position of a passing beam particle. Positions are determined by a charge ratio between the respective left and right signals and up and down signals. The signals are first attenuated and then shaped in a slow amplifier before being sent directly to an ADC. A fast timing signal is also produced in a separate amplifier for any PPAC event. The timing signal is discriminated by a CFD, delayed by 300 ns, and read by a time to digital converter (TDC).

The zero degree detector signal is decomposed into two components, one each for the fast and slow energy signals, and are read directly by FERAs after the preamplifier. A fast timing signal is also produced in the zero degree detector preamplifier which is used in the master logic signal, described below. The timing signal is discriminated to filter noise events. Three identical outputs are taken from the discriminator. One is used in the master logic circuit. The other two are sent to scaler counters, one directly and the other after being rate divided by a factor of 1,000, for absolute cross section measurements. Timing signals were also taken from the beamline PIN diode at the exit of the K1200 and from the RF cyclotron

frequency. Both of these timing signals, and backup timing signals for each, are read by TDCs.

The electronics for the particle telescopes are considerably more extensive than the beam tracking electronics, mostly due to the number of independent channels required. Figure 7.7 is a schematic diagram of the electronics used for a single particle telescope, including Si strip, PIN diode, and CsI signals. Energy signals from each of the 16 Si strips are first amplified in a 16 channel preamplifier, then shaped in a slow amplifier before being read by a peak sensing ADC. The timing signals, also generated in the 16 channel preamplifier, are shaped by an inverting fast amplifier and discriminated by a CFD. Two outputs from the CFD are delayed by 150 ns and used for measuring time signals, one via a common start TFC and read by a FERA for TOF measurements, and the other sent to a scaler counter. A third CFD output is used in the master logic through a logical OR condition with the other telescope strip timing signals. The PIN diode and CsI signals are handled in a similar fashion. The PIN signal is preamplified, then shaped in a combined slow/fast amplifier which gives both energy and timing signals. The energy signal is read directly by an ADC, while the timing signal is discriminated, delayed by 200 ns, and read by a TDC. The CsI signals are processed identically, with the exception that the timing signal is read by a scaler counter.

The master logic circuit is in direct communication with the data acquisition hardware and software, and ultimately controls which events are written to tape. When the master logic coincidence requirement is met, which will be discussed immediately following, all of the aforementioned signals are read out together. The coincidence condition for a "good" event requires detection of a particle in any of the Si strips and detection of a beam particle in the zero degree detector. A coincidence logic unit (CLU), shown in Figure 7.8 along with the rest of the master coincidence electronics, receives delayed gates from the OR of all strip detectors and the zero

degree detector. If both signals are present, the Master CLU outputs a positive coincidence signal which is passed to a gate and delay generator (GDG) before going to a bit register. Even with signals from a strip detector and the zero degree detector present, the acquisition system still requires a start command which was controlled by a second CLU, the Master.Live CLU. The second output of the Master CLU is fed into the Master.Live CLU to provide either a start or a veto to the acquisition. The Master.Live CLU allows for a second "good" event condition from the rate-divided zero degree detector events, which does not require an associated proton event. If either a rate-divided zero degree detector event or a proper particle-beam coincidence is seen by the Master.Live CLU, the start of the acquisition is triggered. A "self busy" veto generated when either the acquisition system or the Master.Live CLU is busy may veto the Master.Live output. The Master.Live output also controls the timing signal gates via a third CLU which requires a signal from the Master.Live CLU and a zero degree detector event. The type of event, whether a particle-beam coincidence or a rate-divided zero degree detector event, is distinguished by which bits are set in the data acquisition bit register.

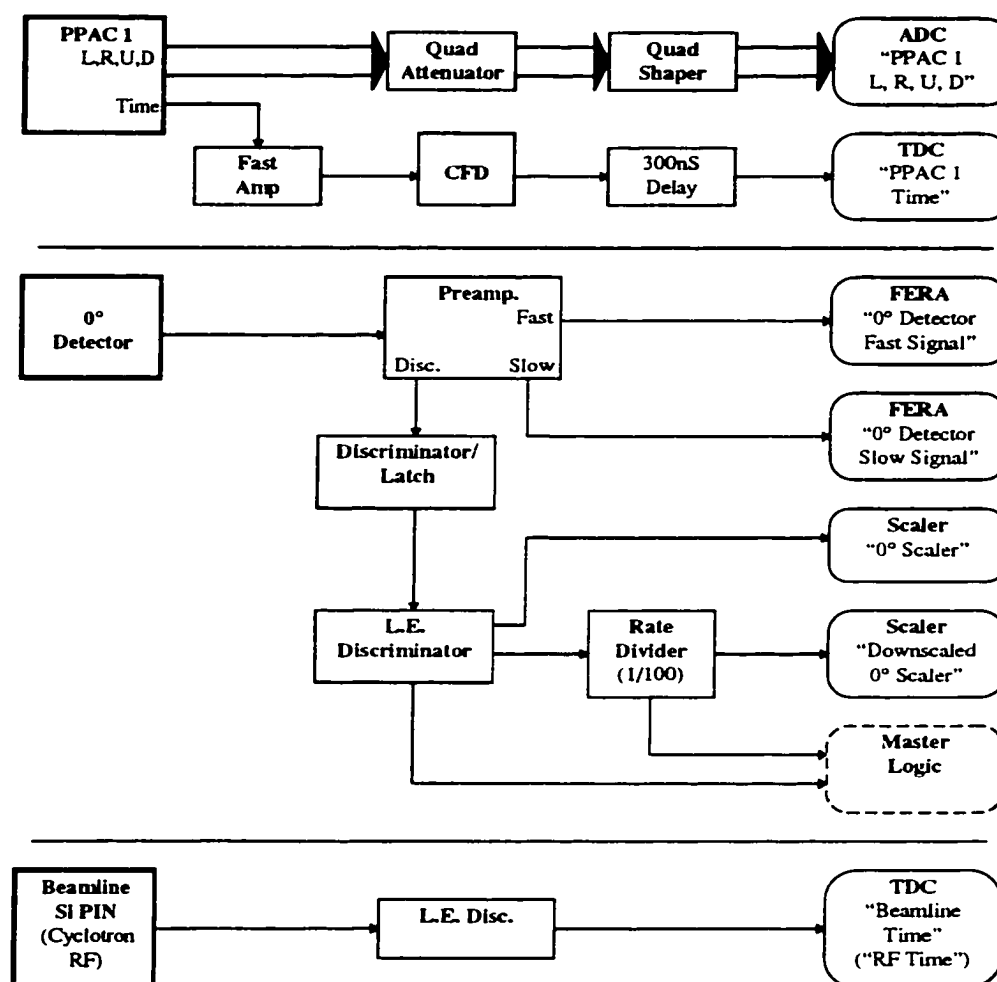


Figure 7.6: Electronics diagram for the beam detectors. Electronics for PPACs 1 and 2 were identical. Gates and time starts were generated by the master electronics shown in Figure 7.8 and are not included explicitly here.

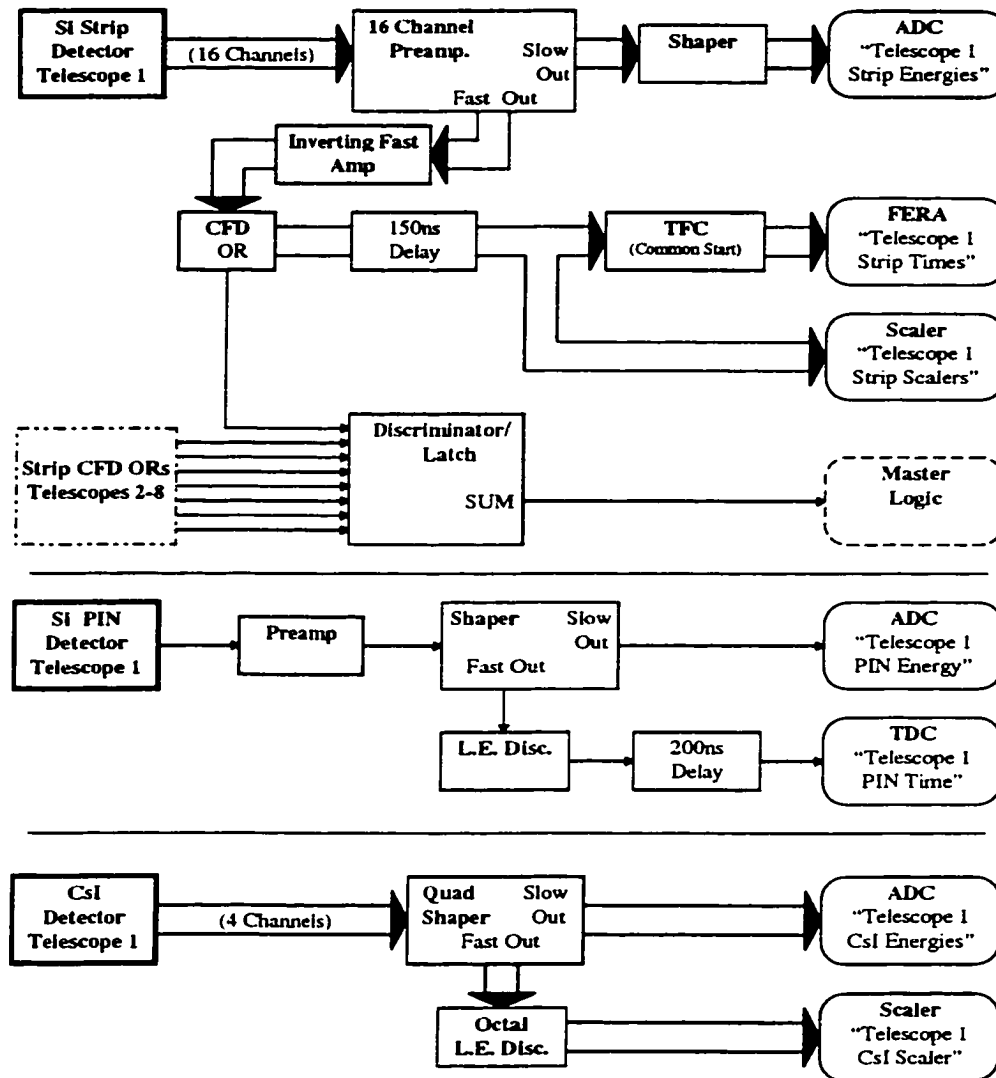


Figure 7.7: Electronics diagram for a single particle telescope. Gates and time starts were generated by the master electronics shown in Figure 7.8 and are not included explicitly here.

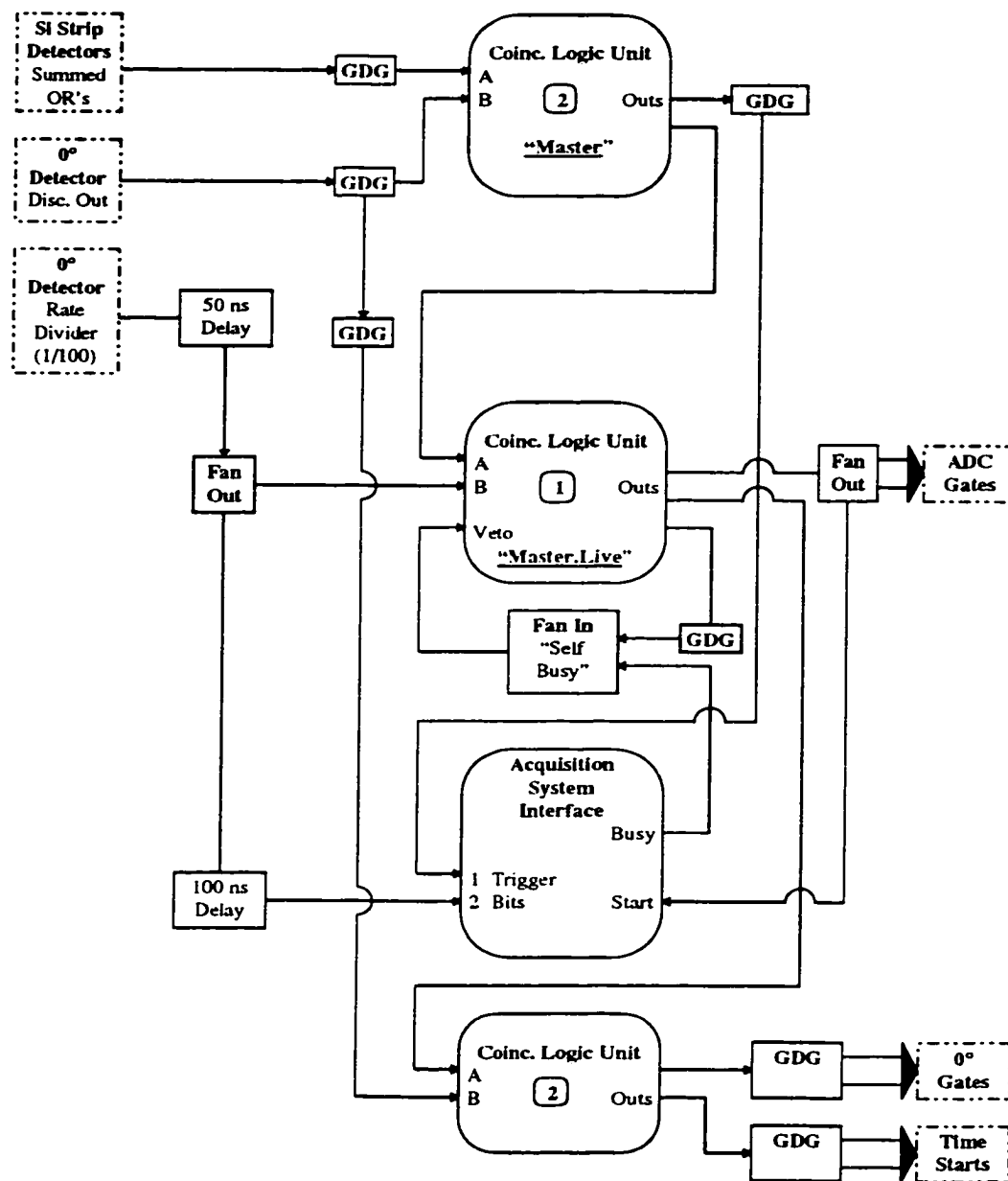


Figure 7.8: Diagram of the master electronics which generated event triggers and gates. The boxed number in the coincidence logic units indicates the coincidence level required between the two inputs labeled A and B.

CHAPTER 8

ANALYSIS AND RESULTS OF $p(^{20}\text{O},p)^{20}\text{O}^*$

8.1 Beam Tracking Correction

The inverse kinematics proton scattering angular distribution measurement required considerable off-line analysis to ensure proper particle identification and to accurately determine scattering angles. The PPAC's provided a means for determining the incident beam angle and the interaction position at the target. The position sensitive Si strip detectors, positioned along lines of constant θ_0 , allow measurement of the scattered proton angle. Beam particle trajectories are not, in general, collinear with the optical beam axis. They are also generally not interacting at the target center. Knowing both the incident beam and the scattered proton trajectories with respect to the optical alignment coordinate system permits a calculation of the final proton scattering angle and the interaction point of the beam with the target. Figure 8.1 shows an arbitrary proton scattering event with the vectors used to reconstruct the beam trajectory and scattering angle.

For determining the beam trajectory, a right-handed Cartesian coordinate system with \hat{y} pointing down (see Figure 8.1) coincident with the optical alignment system proved most useful. An incoming beam particle position is defined at the first PPAC as $\vec{r}_1 = (x_1, y_1, z_1)$, and at the second PPAC by $\vec{r}_2 = (x_2, y_2, z_2)$. The z_1 and z_2 components are fixed by the physical placement of the respective PPACs. Knowing these two position measurements, the angle of the beam trajectory with respect to the optical axis is

$$\theta_{beam} = \tan^{-1} \left[\frac{\sqrt{(x_2 - x_1)^2 + (y_2 - y_1)^2}}{|z_2 - z_1|} \right]. \quad (8.1)$$

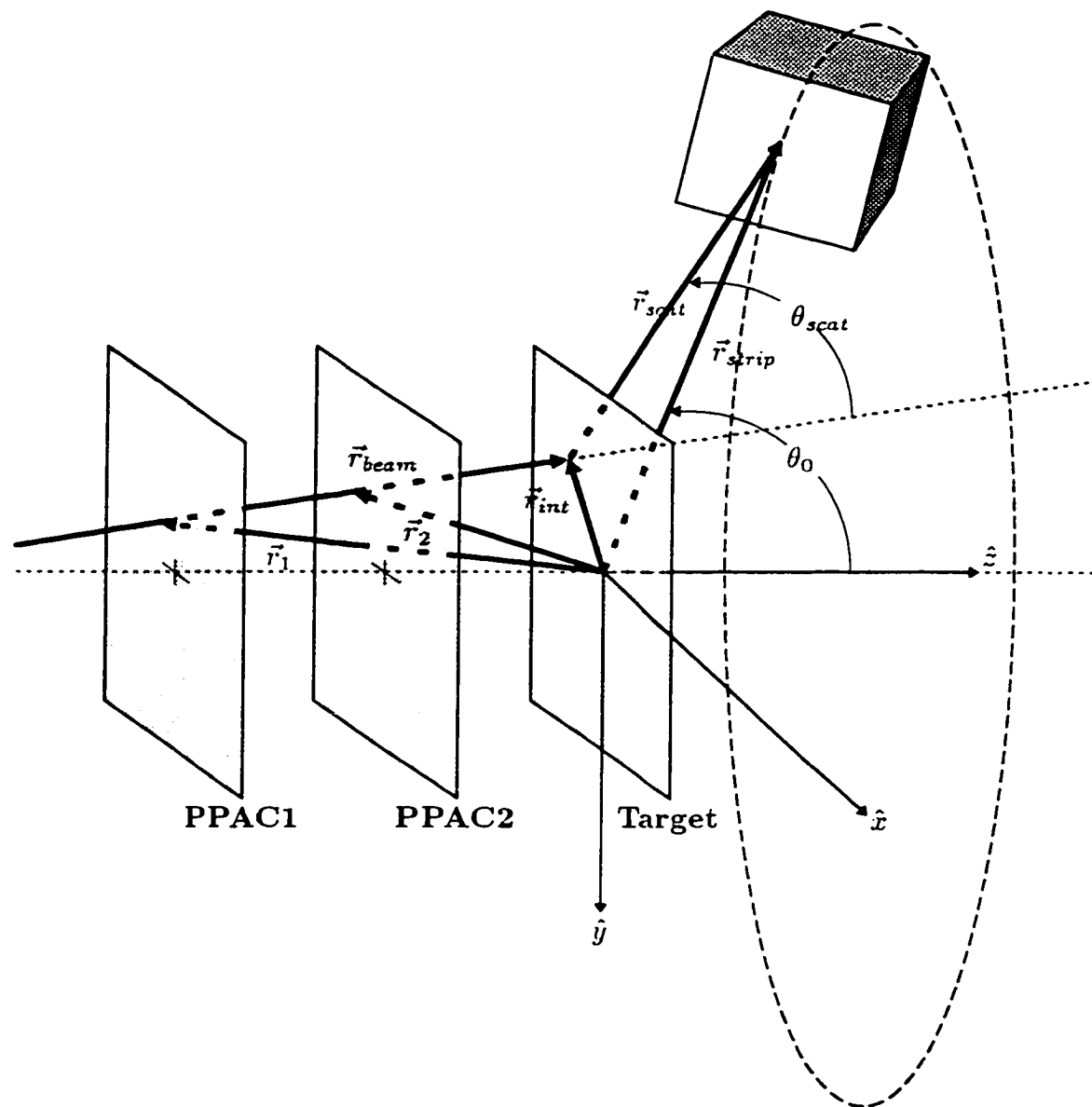


Figure 8.1: The trajectory tracking of an arbitrary proton scattering event. The incoming beam particle with trajectory \vec{r}_{beam} is detected by the position sensitive PPACs at positions \vec{r}_1 and \vec{r}_2 and interacts with a proton in the target at position \vec{r}_{int} . The scattered proton trajectory \vec{r}_{scat} is at an angle θ_0 with respect to the optical axis and an angle θ_{scat} , the proton laboratory scattering angle, with respect to the incoming beam trajectory. For simplicity, the target is shown perpendicular to the incident beam direction.

The interaction point at the target is then calculated by projecting the beam trajectory onto the target. The target was tilted by approximately $\psi_{tilt} = 50^\circ$ with respect to a plane perpendicular to the incident beam direction. For simplicity, Figure 8.1 shows the target perpendicular to the beam direction. The interaction point \vec{r}_{int} is given by

$$x_{int} = \frac{x_2 + \frac{\Delta_x}{\Delta_z} z_2}{1 - \frac{\Delta_x}{\Delta_z} \tan \psi} \quad (8.2)$$

$$y_{int} = y_2 + \frac{\Delta_y}{\Delta_z} \left[z_2 + \frac{x_{int}}{\tan \psi} \right] \quad (8.3)$$

$$z_{int} = \frac{x_{int}}{\tan \psi}, \quad (8.4)$$

where $\vec{\Delta}_{x,y,z} = \vec{r}_{2(x,y,z)} - \vec{r}_{1(x,y,z)}$ is the change in beam position between the two PPACs. A vector describing the beam trajectory \vec{r}_{beam} can now be defined as

$$\vec{r}_{beam} = \vec{\Delta}_{x,y,z}. \quad (8.5)$$

The position of a scattered proton is measured by its detection at the physical location of one of the Si strips, denoted by a vector \vec{r}_{strip} from the coordinate system origin to the particular strip. The scattering position is then

$$\vec{r}_{scat} = \vec{r}_{strip} - \vec{r}_{int}. \quad (8.6)$$

The physical quantity of interest here is θ_{scat} , which is found by taking the scalar product between the two vectors \vec{r}_{beam} and \vec{r}_{scat} as follows.

$$\theta_{scat} = \cos^{-1} \left[\frac{\vec{r}_{beam} \cdot \vec{r}_{scat}}{|\vec{r}_{beam}| |\vec{r}_{scat}|} \right]. \quad (8.7)$$

Because the beam profile on target is rather large, the tracking correction is essential in extracting the actual scattering angles. Figure 8.2 is a two dimensional (\hat{x} and \hat{y} plane) display of the beam projection onto the target. The beam has a FWHM of roughly 2.8 cm, which corresponds to an angular FWHM of 0.9° . An

additional need for the beam tracking arises from the target being tilted. The target tilt of $\psi_{tilt} = 50^\circ$ about the \hat{y} axis results in a much larger angular profile of the target being presented to detectors 1, 2, and 3 than to detectors 4, 5, and 6. This results in a much larger angular correction applied to detectors 1, 2, 3 than for the others, because the large beam profile on target expands the angular field of view of each strip in these telescopes. A particularly illuminating way of illustrating this difference is to plot the angular corrections $\Delta\theta = \theta_{scat} - \theta_0$, shown in Figure 8.3. The correction for telescopes 1, 2, and 3 has a FWHM of 4° , while for telescopes 5, 6, and 7, the correction is on the order of the angular size of the individual strips (0.8°), and only a small correction is required.

The generated angular correction spectra (Figure 8.3) were used as an off-line gating condition. The gating condition required that $\Delta\theta \leq 1.5^\circ$ which limits the angular field of view for each strip in telescopes 1, 2, and 3 to about 3.6° . This degree of correction is used because it represents the minimum correction needed to separate the elastically scattered protons from the inelastically scattered protons. Figure 8.4 shows the effect that the correction has in improving the separation between the elastic and inelastic events. The imposed correction criteria resulted in the loss of about 40% of the total data from half of the telescopes (1, 2, and 3) used. The amount of usable data is, however, significantly greater than that obtainable had physical collimators been used instead of beam tracking.

A comparison of the beam tracking versus the use of physical collimators can be easily done by imposing software gates on the PPAC spectra which mimic the blocking of the beam by physical collimation. Requiring a beam divergence of $\Delta\theta_{beam} \leq 0.6^\circ$, which is comparable to the angular resolution of the particle telescopes, indicates that roughly 85% of the total beam events must be discarded. Given that the intensities of radioactive beams are typically small to begin with, the loss of the majority of the beam is not acceptable. With the use of beam track-

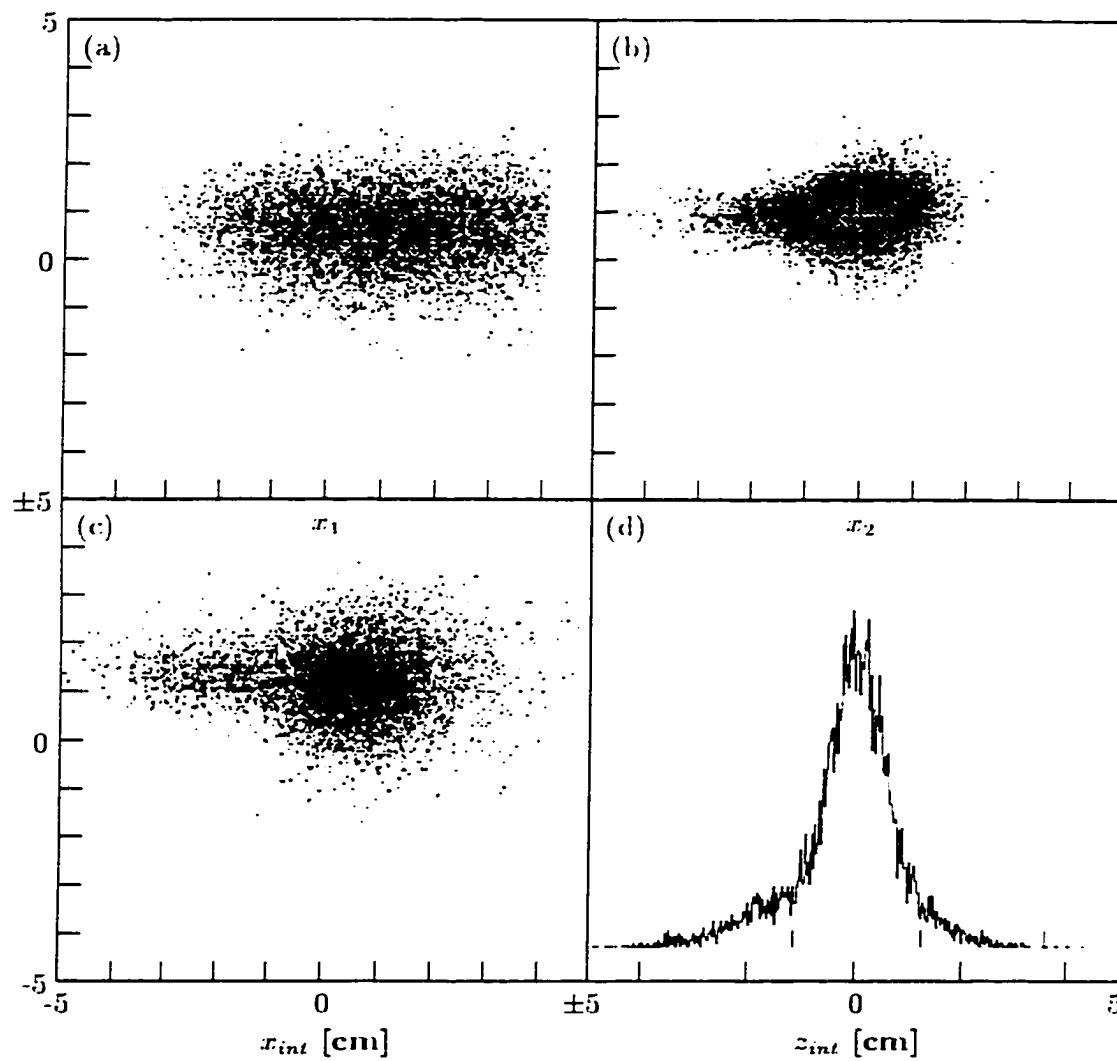


Figure 8.2: Examples of beam tracking spectra show two dimensional position spectra for the beam measured at (a) PPAC 1 and (b) PPAC 2, (c) the projected transverse position, and (d) the z position spectra on target.

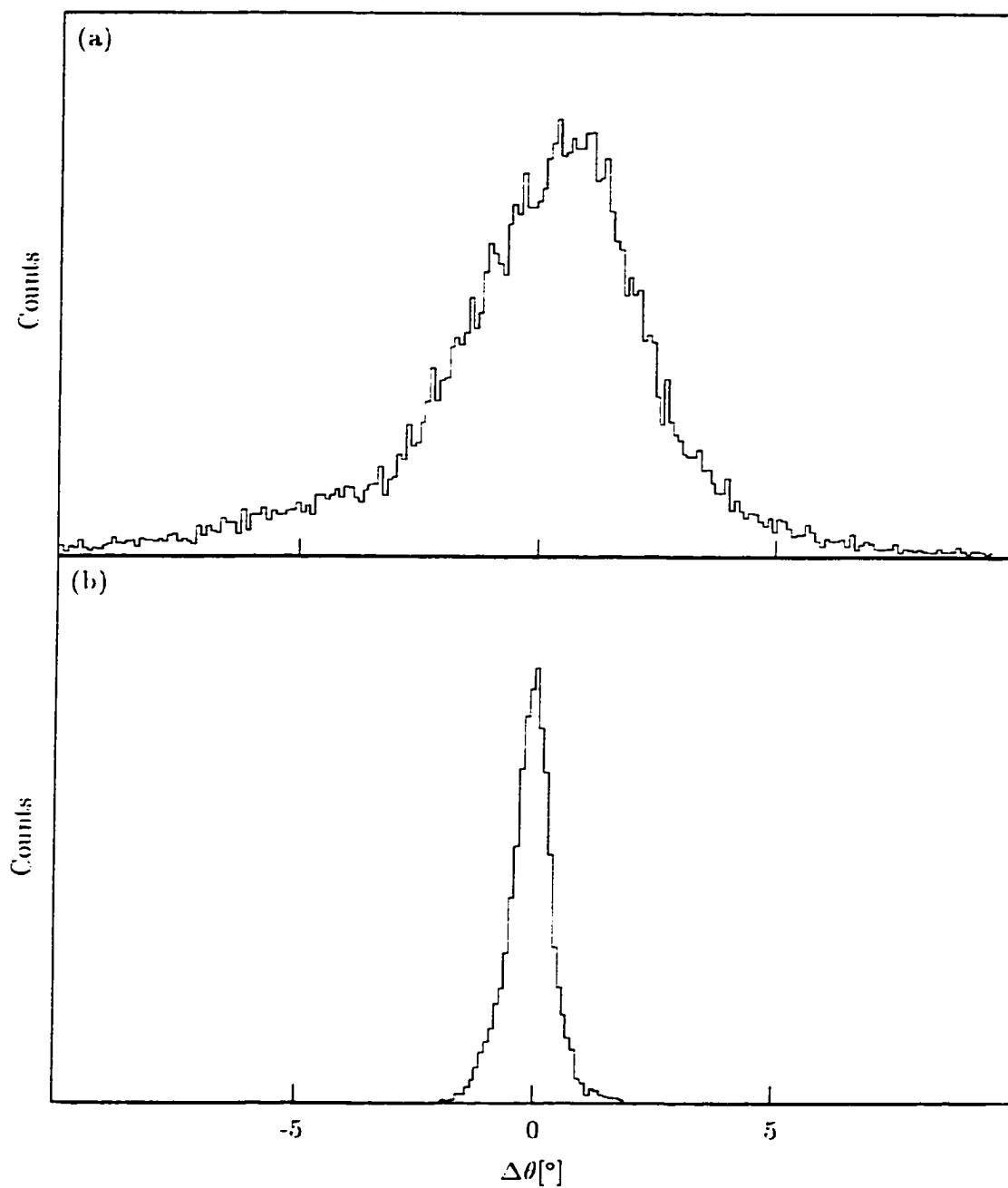


Figure 8.3: Angular correction spectra for (a) telescopes 1,2 and 3 and (b) telescopes 5,6 and 7 show the large correction needed for telescopes 1,2, and 3. The angular resolution for telescopes 5, 6, and 7, however, is on the order of the intrinsic strip width.

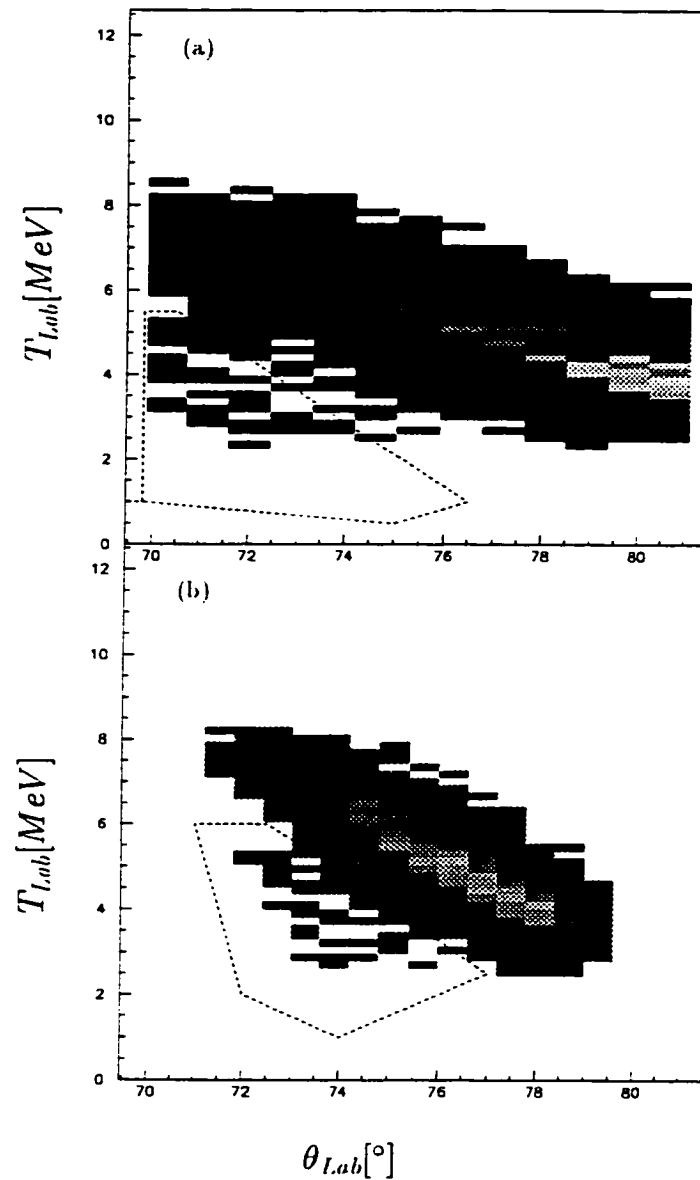


Figure 8.4: Proton laboratory kinetic energy versus scattering angle plots from telescopes 1, 2 and 3 (a) without and (b) with the beam tracking correction, illustrating the need for a scattering angle correction in order to separate the elastic and inelastic events. The inelastic events are indicated by the dashed boxes.

ing, however, 80% of the beam is usable while still maintaining acceptable angular resolution.

8.2 Proton Angular Distributions

We imposed numerous software gates in addition to the beam tracking correction to generate the final angular scattering information. As previously mentioned in Chapter 7, a gate placed on the characteristic energy loss of ^{20}O in the zero degree detector ensured that only events associated with an ^{20}O beam particle were accepted. Additionally, $\Delta E - E$ and $TOF - E$ gates were used to filter particle events other than protons seen in the telescopes. The resulting proton scattering events were then sorted into discrete angular bins to generate an angular distribution.

A small portion of the available beam time was spent scattering ^{20}O from a natural carbon target. Since the polypropylene target is composed of CH_2 , the carbon target data provide a way of subtracting any events from carbon. Due to the very different kinematics of ^{20}O scattering from carbon, though, these events were not in the field of view of the telescope detectors, and were not observed. Hence, no subtraction was needed.

The proton scattering data is most naturally put into angular bins which correspond to the individual strips of the particle telescopes. This method of binning the angular information ensures that all of the bins have an equal solid area, and avoids having to determine efficiencies on a strip by strip basis. In the center of mass, however, this choice of bins results in a measurement of different scattering angles for the elastic and inelastic events. The scattering data is presented in the form of a two dimensional kinematics plot, having energy plotted against the corrected laboratory scattering angle. Figure 8.5 shows the calculated kinematic curves for both the ground state (elastic scattering) and the 2_1^+ state (inelastic scattering). The same calculation was used to determine the initial placement of the particle telescopes. Figure 8.5 also shows the actual data collected in the experiment. The data shown has been fully corrected for scattering angle. As evidenced by the figure, the data reproduces the expected kinematic curves from the calculations. The data

also shows a clear separation between the ground state and the 2_1^+ state at 1.67 MeV.

The angular distribution is generated by separately summing the elastic and inelastic counts in a single angular bin (one strip). Two bins per data point were used for the inelastic counts due to lower yields. Representative kinematics plots from a single angular bin, which were used in the angular distribution measurement, are shown in Figure 8.6. A conversion to the center of mass was carried out for each data point consisting of angle and yield information. Since the center of mass angles for a particular strip are different for elastic and inelastic events, this results in a slightly different angular range measured for the two states. The angular distribution in the center of mass is displayed in Figure 8.7. The solid lines through the data points are from a coupled channels analysis of the data, which is discussed in the following section. Error bars denote the width of the angular bin and the uncertainty in the cross section.

8.3 Coupled Channels Calculations

Coupled channels calculations (see Chapter 6 for an overview) were performed using the computer code CHUCK [Kunz]. The coupled channels calculations were used to extract the RMS value of the dynamic deformation parameter β_2 of the 2_1^+ state in ^{20}O from the experimental elastic and inelastic proton angular distributions. The optical model parameters used in the analysis are from a 35 MeV (p, p') study by de Swiniarski *et al.* [deS74] on the neighboring nucleus ^{20}Ne , because the detailed elastic scattering data necessary to perform a credible optical model analysis of ^{20}O is not available. We assume that the parameters for elastic scattering do not vary greatly among neighboring nuclei. The parameters are provided in Table 8.1, and their applicability to ^{20}O is discussed in Chapter 9.

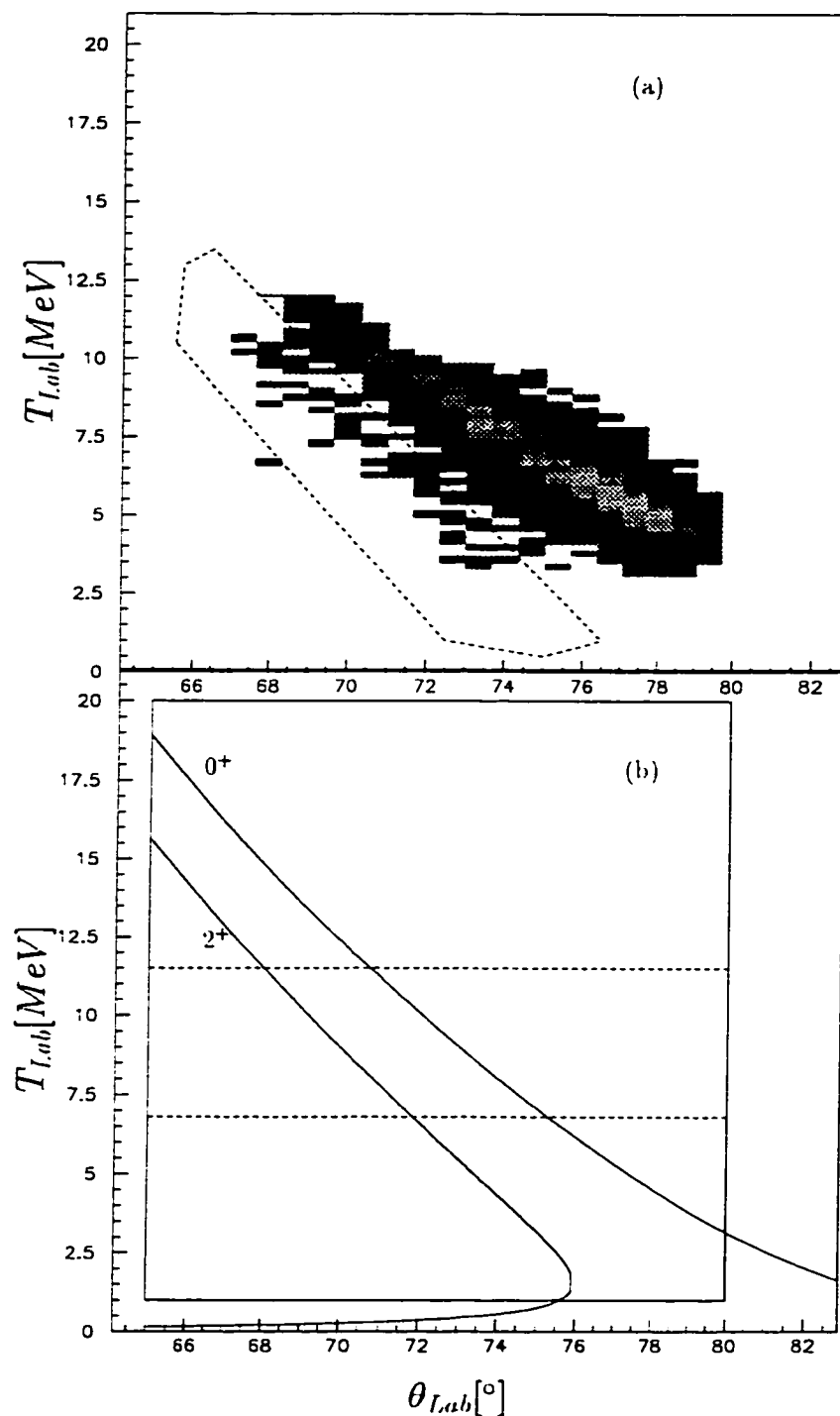


Figure 8.5: Comparison of actual data and calculated kinematics. (a) The collected proton scattering data displayed on the same scale as the calculated kinematics in (b). The dashed box indicates the identified inelastic events. (b) Calculated kinematic curves of energy as a function of scattering angle in the laboratory frame. The solid box shows the field of view of the telescopes. The dashed lines show the punch through energies for a proton penetrating into the next stage of the telescope.

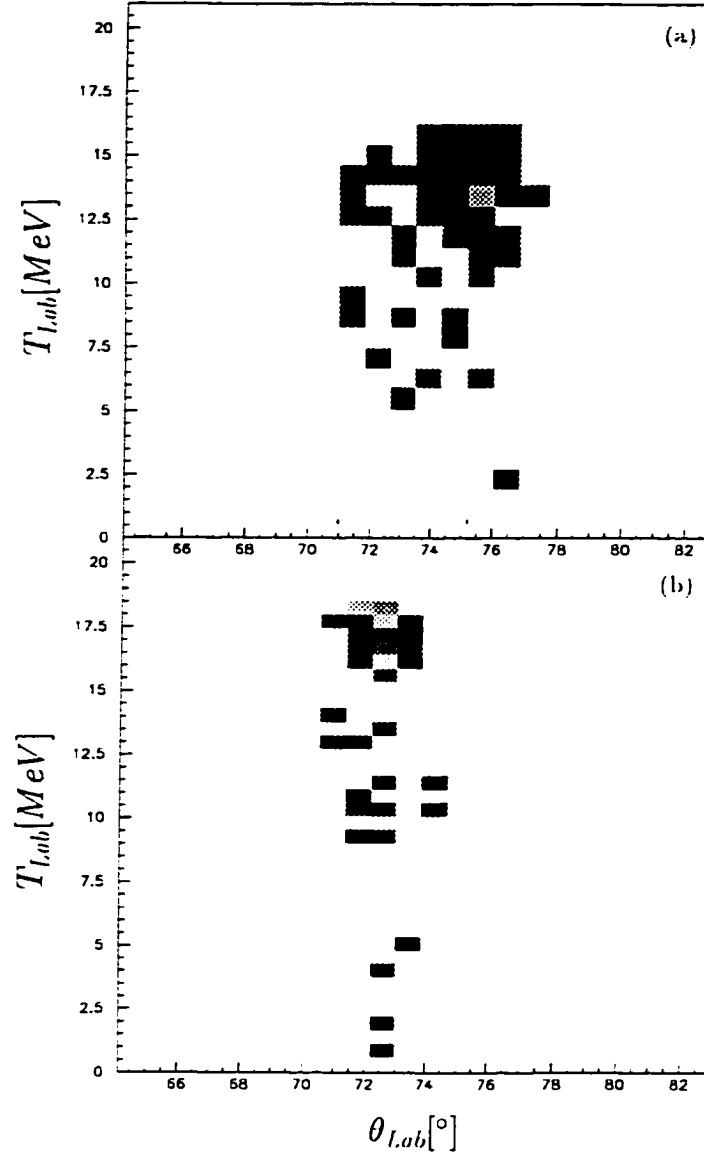


Figure 8.6: Summed proton laboratory kinematics spectra from (a) strip 4 of telescopes 1, 2 and 3 and (b) strip 4 of telescopes 5, 6 and 7. Spectra of this kind were used in summing the cross sections to generate the angular distribution.

As mentioned in Chapter 6, the full optical potential used has both diagonal terms U_{cc} and off diagonal terms U'_{cc} . U_{cc} has the explicit form

$$\begin{aligned}
 U_{cc} = & \frac{2\mu_c}{\hbar^2} \left[-V_R f(x_R) + iW_D \frac{df(x_I)}{dx_I} + V_{Coulomb}^{Elastic}(r_c) \right. \\
 & \left. + V_{SO} \frac{1}{r_c} \frac{df(x_{SO})}{dr_c} \vec{l}_c \cdot \vec{s}_c \right], \quad (8.8)
 \end{aligned}$$

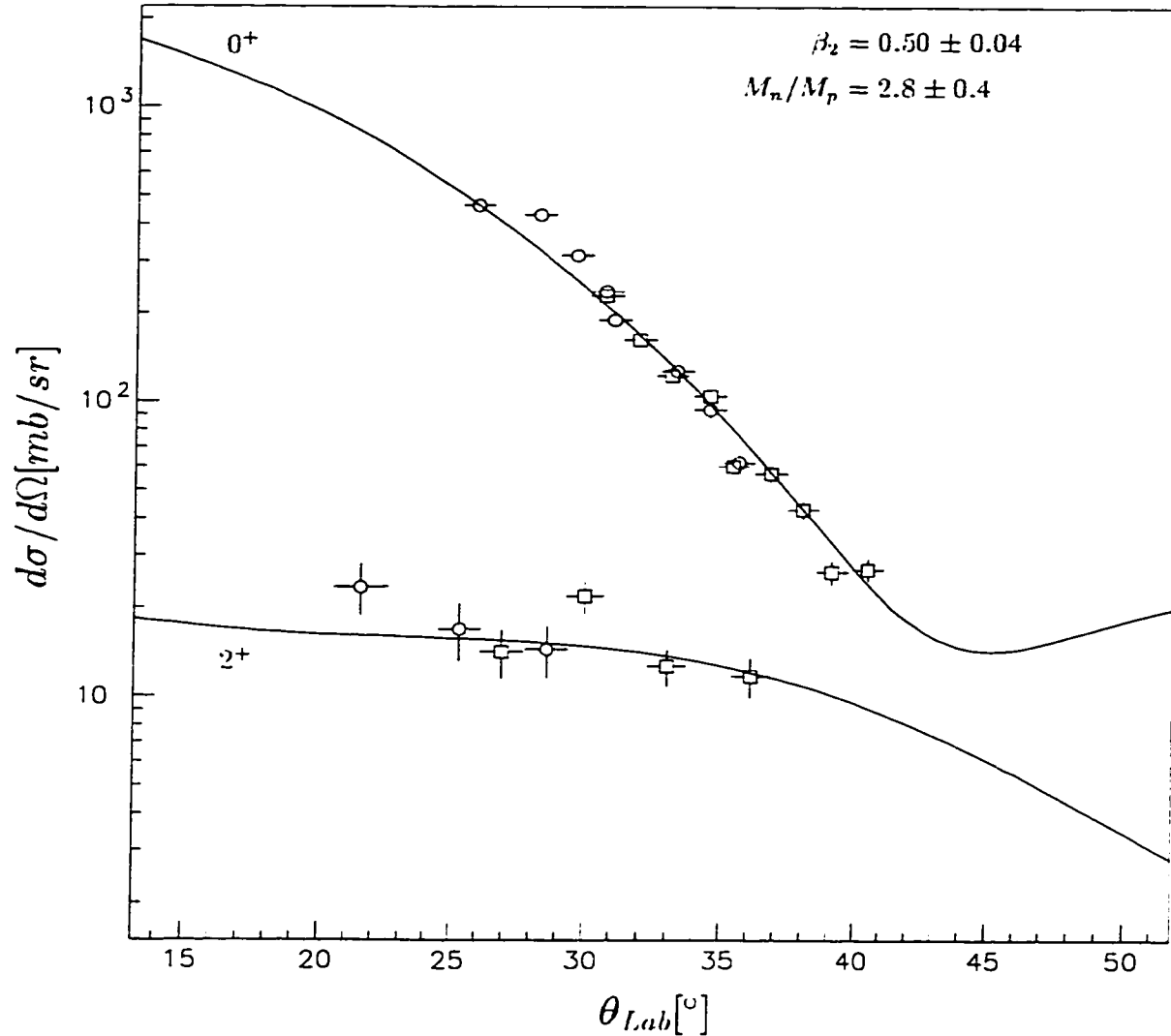


Figure 8.7: Angular distributions of protons scattered from the ground state and 2^+ state of ^{20}O . The smooth curves are coupled channel calculations using known optical model parameters from ^{20}Ne and the RMS quadrupole deformation β_2 giving the best reproduction of the inelastic cross section.

where r_c and μ_c are defined as in Chapter 6 respectively as the relative channel coordinates and the reduced mass of the projectile and target system, and \vec{l}_c is the relative angular momentum between the projectile with spin \vec{s}_c and the target. The

potential terms contained in U_{cc} are a real Woods-Saxon volume potential V_R , an imaginary Woods-Saxon surface absorption W_D , the Coulomb potential $V_{Coulomb}^{elastic}$ for elastic scattering, and a spin-orbit term V_{so} . A volume Woods-Saxon form factor is also used, and is given by

$$f(x_i) = \frac{1}{[1 + e^{x_i}]}; \quad x_i = \frac{r_c - r_i A^{\frac{1}{3}}}{a_i}, \quad (8.9)$$

where A is the target mass number, V_i , r_i , and a_i are the potential well depth, radius and diffuseness, respectively, and the subscript i can refer to real (as in V_R), imaginary (as in W_D), or spin-orbit (as in V_{SO}) potentials as appropriate. The surface Woods-Saxon form factor for the surface absorption W_D is taken as the first derivative with respect to x_i of the volume form factor.

For the simple vibrational model we use in the present analysis, the off-diagonal (or channel coupling) potential terms $U'_{cc'}$ are just the first term in an expansion of each potential term in U_{cc} (V_R , W_D , $V_{coulomb}$) about its equilibrium radius. The spin-orbit potential is neglected in the coupling. Assuming a pure quadrupole vibration, so that the 2_1^+ state is the only state coupled to the elastic channel, gives

$$U'_{cc'} = \frac{2\mu_c}{\hbar^2} \beta_2 \left[V_R r_R \frac{df(x'_R)}{dx'_R} - i W_D r_I \frac{d^2 f(x'_I)}{dx'^2_I} + r_{c'} V_{Coulomb}^{Inelastic}(r_{c'}) \right] \\ \times \sum_m D_m^2(\epsilon_t) Y_{2m}(\hat{r}_{c'}), \quad (8.10)$$

where β_2 is the RMS quadrupole deformation of the target in the 2_1^+ state inelastic channel. The $D_m^2(\epsilon_t)$ performs a rotation through the Euler angles of Y_{2m} , and the ϵ_t represent the Euler angles connecting the intrinsic reference frame of the target to the channel coordinates.

Besides defining the optical model parameter values, the computer code CHUCK also allows definition of multiple deformation parameters for every channel included in the coupling. For our simple vibrational model in the present analysis, only the RMS quadrupole deformation β_2 of the 2_1^+ state was used. For simplicity, the

Table 8.1: Optical model parameters for ^{20}Ne and ^{20}O

| V_R | r_R | a_R | W_D | r_I | a_I | V_{SO} | r_{SO} | a_{SO} |
|-------|-------|-------|-------|-------|-------|----------|----------|----------|
| [MeV] | [fm] | [fm] | [MeV] | [fm] | [fm] | [MeV] | [fm] | [fm] |
| 44.3 | 1.10 | 0.73 | 6.96 | 1.38 | 0.60 | 7.80 | 1.03 | 0.74 |

calculation was done for standard 30 MeV proton scattering kinematics, where the protons were treated as projectiles and ^{20}O as stationary target nuclei. This makes no difference to the results, since the calculation is carried out in the center of mass frame.

A test of our coupled channels calculation method was carried out to reproduce the results of de Swiniarski *et al.* [deS74] for ^{20}Ne prior to our calculations for ^{20}O . The results of de Swiniarski *et al.* were performed using a rotational model for ^{20}Ne with the computer code ECIS. Using the identical optical model parameters (see Table 8.1), we were able to reproduce the results of de Swiniarski *et al.* by using a vibrational model in our coupled channels calculations. Although a rotational model is certainly more applicable to ^{20}Ne , this test indicates that our coupled channels calculations are not sensitive to the choice of rotational or vibrational models. A similar insensitivity was reported by Grabmayr *et al.* [Gra80] in their analysis, which also used CHUCK, of inelastic nucleon scattering for the 2_1^+ state in ^{18}O .

Our calculations for ^{20}O were performed in an identical manner to the test calculations. We adjusted the magnitude of β_2 in successive, but otherwise identical, calculations to obtain the best reproduction of the inelastic scattering cross section. The integration was performed with 20 partial waves out to a distance of 10 fm in steps of 0.1 fm. The best reproduction of the 2_1^+ state angular distribution is with $\beta_2 = 0.50 \pm 0.04$, which is very close to the β_2 value of 0.47 in ^{20}Ne reported by de Swiniarski *et al.* [deS74]. The calculation results and the experimentally measured angular distribution are shown in Figure 8.7.

8.4 M_n/M_p Determination

Calculating M_n/M_p , the ratio of the neutron to proton multipole matrix elements, for the $0_{gs}^+ \rightarrow 2_1^+$ transition in ^{20}O follows the method put forth in References [Mad75, Ber79, Ber81, Ber83]. The two experimental values required in the calculation are the RMS quadrupole deformation parameter β_2 from (p, p') , determined from the proton scattering angular distribution, and the reduced transition probability $B(E2)$ from an electromagnetic probe. We use the adopted value [Ram87] of $B(E2) = 1.80 \pm 0.07$ W.u. from lifetime measurements of the γ -ray decays from the 2_1^+ state [Ber75, Her77, Rut80, Til95]. Following the prescription of Bernstein *et al.* [Ber83], M_n/M_p is determined from these two experimental quantities by the relation

$$\frac{M_n}{M_p} = \frac{b_p}{b_n} \left[\frac{\delta_{(p,p')}}{\delta_{em}} \left(1 + \frac{b_n N}{b_p Z} \right) - 1 \right]. \quad (8.11)$$

The terms b_n and b_p denote the sensitivities of the particular experimental probe to neutron and proton distributions respectively. As discussed previously (see Chapter 6), proton scattering in the energy range of the present experiment (10-50 MeV) is roughly three times more sensitive to the neutron distribution as to the protons, as given in Table 6.1. This gives $b_n/b_p \approx 3$ in the present work. The terms $\delta_{(p,p')}$ and δ_{em} are respective deformation lengths for proton scattering and electromagnetic probes, also discussed in Chapter 6. We assume a uniformly spherical neutron distribution to relate $\delta_{(p,p')}$ to the RMS quadrupole deformation value $\beta_2(p, p')$ by

$$\delta_{(p,p')} = \beta_2(p, p') r_0 A^{1/3} \quad (8.12)$$

where $r_0 = 1.1$ fm is used for consistency with the real part of the optical potential ([deS74] and Table 8.1). Likewise, since this is a simple collective model, we assume a uniformly spherical proton distribution, and relate δ_{em} to $B(E2)$ by the relation

$$\delta_{em} = \frac{r_C A^{1/3}}{5Z} [B(E2)20\pi]^{1/2} \quad (8.13)$$

where $r_C = 1.2$ fm (the Coulomb radius) is used. This gives, finally,

$$\frac{M_n}{M_p} = \frac{1}{3} \left[5Z \left(\frac{1.1}{1.2} \right) \frac{\beta_2(p, p')}{\sqrt{20\pi B(E2)}} \left(1 + \frac{3N}{Z} \right) - 1 \right]. \quad (8.14)$$

Substituting the values of $\beta_2(p, p')$ and $B(E2)$ gives $M_n/M_p = 2.8 \pm 0.4$.

Bernstein *et al.* have pointed out that this approach of obtaining M_n/M_p is somewhat model dependent [Ber81, Ber83]. However, the difference in most nuclear models reveals itself primarily in the transition densities $\rho_{fi}(r)$ for small values of r , and proton scattering at 30 MeV is not very sensitive to the nuclear interior [Ber83]. Carr *et al.* pointed out that nucleon scattering of at least 60 MeV was needed to effectively probe the nuclear interior [Car85b], due to the attenuation of the nucleon wave. Bernstein *et al.* also point out that the r^λ dependence of the multipole operator $O_{\lambda\mu}^F$, which is decomposed into neutron and proton operators in Equation 6.3, reduces the sensitivity of the probe to the nuclear interior [Ber83]. Furthermore, our measured proton angular distribution is primarily at forward angles (20° to 45°), where model dependence is less important. The effects from model dependence have been shown to be small for low energy α scattering [Ber69, Mad77] and proton scattering [Wam79].

CHAPTER 9

DISCUSSION OF ^{20}O RESULTS

The present work finds that $M_n/M_p = 2.8 \pm 0.4$ for the $0_{gs}^+ \rightarrow 2_1^+$ transition in ^{20}O is significantly higher than the $N/Z = 1.5$ value expected for a purely isoscalar excitation. The high M_n/M_p value shows that the 2_1^+ excitation is dominated by neutron oscillations from the four valence neutrons in the $2s1d$ shell that lie outside the relatively inert core of completely filled $Z = 8$ proton and $N = 8$ neutron shells. This result is consistent with our expectations for a singly closed shell nucleus. Hence, it appears that the underlying shell structure of this nucleus plays a large role in the $0_{gs}^+ \rightarrow 2_1^+$ transition, and that the simple picture of a collective, isoscalar excitation is not a sufficient description.

The systematic behavior of $(M_n/M_p)/(N/Z)$ for $0_{gs}^+ \rightarrow 2_1^+$ transitions in the $12 \leq A \leq 26$ mass region can be seen in Figure 9.1. Results from proton scattering [DeL83, Gra80, Ril:diss, deS74, Has83, Zwi83], neutron scattering [Gra80, Ols89, Ols90], and electromagnetic [Ram87] measurements are included where available. The proton and neutron scattering results are compiled from sources where a coupled channels analysis similar to that used in the present work was used to extract RMS quadrupole deformation parameters. In the case of ^{18}Ne [Ril:diss], the value was obtained from the same experimental apparatus and analysis method as the present work. All of the reported M_n/M_p values were derived from Equation 6.7 with the appropriate probe sensitivities from Table 6.1. The dashed lines in Figure 9.1 are shell model predictions from Brown *et al.* [Bro82], and the solid line represents $M_n/M_p = N/Z$, the expected value for equal neutron and proton oscillation amplitudes.

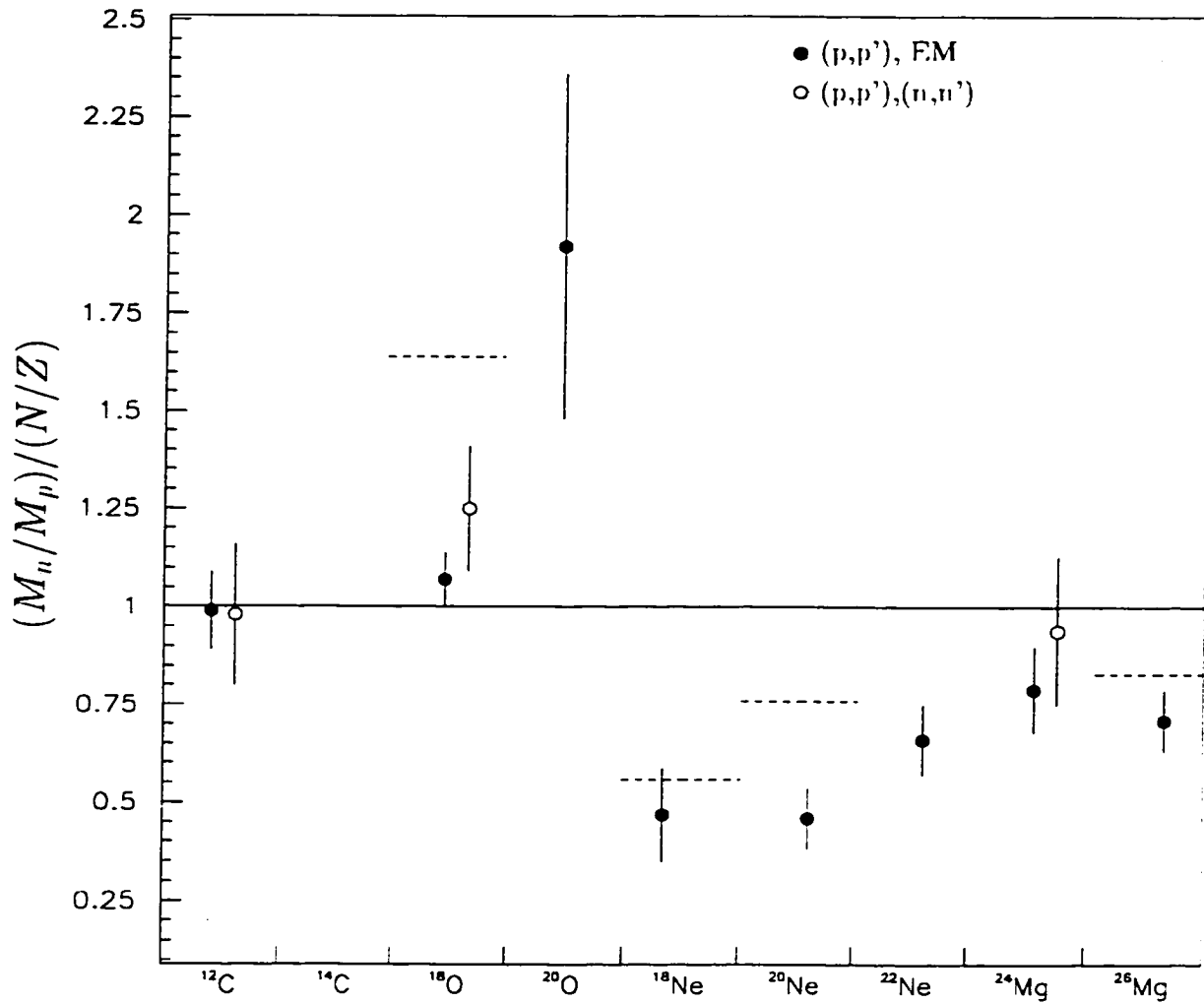


Figure 9.1: Ratios of $(M_n/M_p)/(N/Z)$ for $0_{g.s.}^+ \rightarrow 2_1^+$ transitions in the $12 \leq A \leq 26$ mass region. The values are extracted from comparisons of proton scattering [DeL83, Gra80, Ril:diss, deS74, Has83, Zwi83], neutron scattering [Gra80, Ols89, Ols90], and electromagnetic [Ram87] measurements. The dashed lines are shell model predictions from [Bro82].

Although the shell structure appears to have a large effect on the 2_1^+ excitation in ^{20}O , Figure 9.1 suggests that the simple shell predictions of Reference [Bro82] do not provide an adequate description of the entire mass region. While we expect that singly closed shell nuclei would be better described with a shell model than would

open shell nuclei, the results of Brown *et al.* [Bro82] do not adequately explain the data for both categories of nuclei. The shell model predictions are very close to the experimental M_n/M_p values in the open shell nucleus ^{26}Mg and the singly closed shell nucleus ^{18}Ne . However, the predictions are substantially different from the experimental values for the open shell nucleus ^{20}Ne and the singly closed shell nucleus ^{18}O . Brown *et al.* have pointed out that the most likely cause for errors in their calculations (described in Chapter 6) stems from their use of a harmonic oscillator radial dependence in the single-particle wave functions [Bro82]. They also point to questionable experimental results, and stress the importance of confirming previous measurements. Although there is good agreement between the combined proton scattering and electromagnetic method ($p - EM$ method) and the combined proton and neutron scattering method ($p - n$ method), we see discrepancies in the reported M_n/M_p values when compared to results derived from pion scattering.

Figure 9.2, very similar to Figure 9.1, is a plot of $(M_n/M_p)/(N/Z)$ taken from pion scattering results compiled by Peterson [Pet93]. The figure compares M_n/M_p values obtained from scattering both π^+ and π^- pions from fixed targets with the values obtained from $p - EM$ and $p - n$ methods. Pion scattering, as mentioned in Chapter 1, is an independent method of measuring M_n/M_p .

The pion scattering M_n/M_p values given here agree qualitatively with the simple shell model picture, where deviations from the simple collective $M_n/M_p = N/Z$ value are expected for the singly closed shell nuclei ^{14}C and ^{18}O . Likewise, the M_n/M_p values fall close to the N/Z expectation for the open shell nuclei $^{20,22}\text{Ne}$ and $^{24,26}\text{Mg}$. However, the quantitative shell model predictions of Brown *et al.* [Bro82], do not agree with the M_n/M_p results derived from pion scattering any more than they do for the results derived from the $p-EM$ or $p-n$ methods. In fact, in the three nuclei where a direct comparison is possible (^{18}O , ^{20}Ne , and ^{26}Mg), the shell model predictions fall in between the M_n/M_p values derived from pion scattering and nucleon scattering.

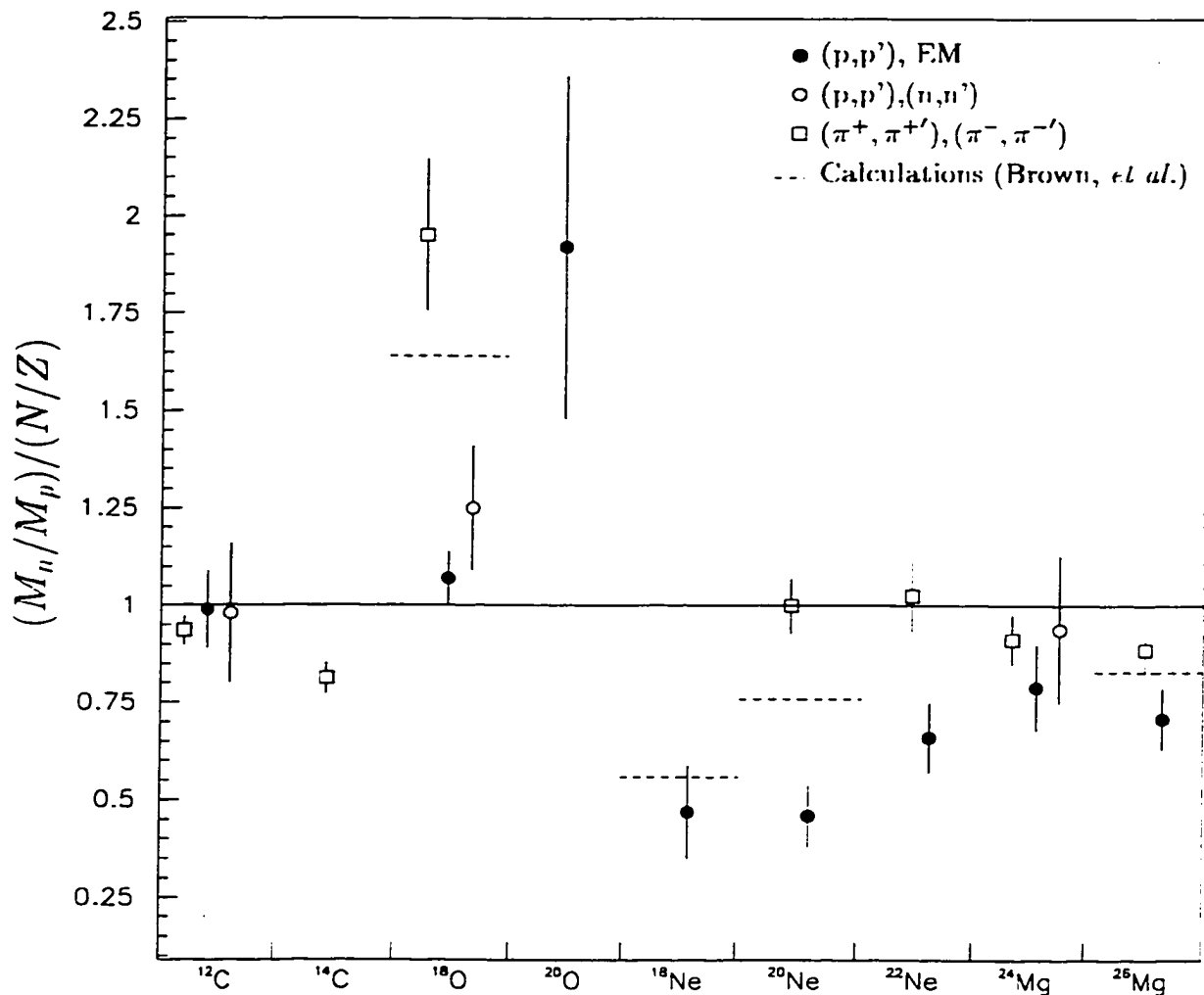


Figure 9.2: $(M_n/M_p)/(N/Z)$ ratios for the $0_{gs}^+ \rightarrow 2_1^+$ transitions in the $12 \leq A \leq 26$ mass region. The results from pion scattering are compared to those from nucleon scattering and electromagnetic results. The dashed lines are shell model predictions from [Bro82].

The discrepancy between the results obtained by pion scattering and those obtained from nucleon scattering raises some concern. When viewed as a whole in the $12 \leq A \leq 26$ mass region, the results obtained by pion scattering seem to best match our expectations from simple shell model and collective model arguments.

Even though M_n/M_p results derived from the pion scattering and nucleon scattering agree well for $A \geq 40$ [Ber81], many authors have pointed out the discrepancy in the $12 \leq A \leq 26$ mass region [Ber81, Bro82, Ber83, Car85b, Pet93]. Unfortunately, a satisfactory answer to this discrepancy has not yet been given. Both pion scattering near the Δ resonance and low energy nucleon scattering are strongly absorbed at the nuclear surface. Although low energy nucleons can penetrate more deeply into the nuclear interior than pions at the Δ resonance, effects from this are expected to be very slight for incident nucleons below 60 MeV [Car85b].

It is also quite possible that we have not entirely removed the probe sensitivity from the present analysis. As discussed in Chapter 6, the probe sensitivity factors we have used from Reference [Ber81] are based on the assumption that the isoscalar strength of the optical potential is twice that of the isovector strength. This is a crude assumption; however, it has been used with much success in $A \geq 40$ nuclei, where very little discrepancy between M_n/M_p results derived from pion scattering and nucleon scattering is seen [Ber81].

Additionally, a systematic bias may exist in this mass region in the deformed optical model potential method most often used to extract β_2 from cross-section data. The pion scattering M_n/M_p value for ^{18}O , for example, is significantly higher than that obtained from nucleon scattering. Indeed, with the exception of ^{12}C where the values nearly agree, a higher M_n/M_p value is obtained from pion scattering in every nucleus (^{18}O , $^{20,22}\text{Ne}$, and $^{24,26}\text{Mg}$) where a direct comparison is possible. The fact that the results derived from pion scattering are always larger would seem to indicate a systematic difference in the two analyses. Since there are so few data points with which to make a direct comparison, however, we can not say with certainty whether or not a systematic analysis difference exists. All of the pion scattering results have been taken from a consistent analysis [Pet93] in which a folding calculation with a distorted wave impulse approximation (see Reference

[Sat83]) was used. A similar, consistent analysis of the nucleon scattering data using a folding model analysis would be quite helpful in detecting a systematic analysis difference.

Since neither M_n/M_p values from pion scattering nor shell model calculations exist for the $0_{gs}^+ \rightarrow 2_1^+$ transition in ^{20}O , it is difficult to evaluate the extent of any systematic analysis error in the present work. We can, however, examine possible sources of error in our experiment and our subsequent analysis. The scattered proton angular distribution we observe is limited by the angular resolution of the detectors ($0.8^\circ - 3.6^\circ$) and by our ability to separate the elastically scattered from the inelastically scattered protons. Each of these factors contributes only slightly to the total error of about 20% in our determination of M_n/M_p . This is because the extraction of the RMS deformation parameter β_2 from our coupled channels calculations is primarily dependent upon the total yield of inelastic events relative to elastic events. Roughly 80 % of the total error in our M_n/M_p determination comes from uncertainty in the γ -ray lifetime measurement of B(E2). The angular distribution over a range of $15^\circ - 45^\circ$ in the center of mass, does, however allow us to check the reasonableness of our coupled channels calculations.

As stated in Chapter 8, we used the existing optical model parameters from the nucleus ^{20}Ne [deS74] in our coupled channels analysis of the proton angular distribution from ^{20}O . The elastic scattering data for ^{20}O is not sufficient to extract reliable optical model parameters, and we chose the parameters of ^{20}Ne as the best alternative for our analysis. The best indication that those optical model parameters are applicable to ^{20}O is that they reproduce well the observed angular distribution for the elastically scattered protons (see Figure 8.7). Furthermore, we have used a phenomenological optical model which is based on the assumption that the optical model parameters vary slowly and smoothly throughout the Periodic Table [Sat83],

so that we don't expect large differences in the optical model parameters for elastic scattering between neighboring nuclei.

Even with the possibility of a systematic discrepancy between the pion scattering analysis and the proton scattering analysis, we can conclude that the $0_{gs}^+ \rightarrow 2_1^+$ transition in ^{20}O is dominated by valence neutron contributions consistent with $Z = 8$ proton shell closure effects. The $p - EM$ method of the present experiment has been used extensively and successfully in the $A \geq 40$ mass region where M_n/M_p values agree with those derived from pion scattering [Ber81]. If, as it seems from the available data, the pion scattering analysis yields a systematically larger M_n/M_p value than the proton scattering analysis, our result of $M_n/M_p = 2.8 \pm 0.4$ from the $p - EM$ method is clearly an indication of a dominant neutron contribution to the $0_{gs}^+ \rightarrow 2_1^+$ transition. We can not claim, however, to have made a precise measurement of M_n/M_p , as evidenced by the large error bars in Figure 9.2. Nor can we yet claim that M_n/M_p is getting larger as we move farther from stability towards the neutron drip line. Such a conclusion would require higher quality data.

In order to understand the systematic behavior of M_n/M_p for the $0_{gs}^+ \rightarrow 2_1^+$ transitions in nuclei approaching the drip line, additional experimental information is required. The singly closed shell nuclei offer the best possibility for confirmation of a large valence nucleon contribution observed in $^{18,20}\text{O}$ and ^{18}Ne . A study similar to the present one on the nuclei $^{22,24}\text{O}$ would allow systematic comparisons of the present data with other $Z = 8$ closed proton shell nuclei. The intensities for producing these secondary beams have been experimentally determined [Fa:diss] at ≈ 300 pps and ≈ 1 pps respectively, at the present NSCL facility, well below the desired intensities of a few thousand pps for successful inverse kinematics proton scattering experiments. However, the planned coupled cyclotron upgrade at the NSCL should increase the available secondary beam intensities by an estimated factor of 1,000 or

more, making studies for other singly closed shell nuclei in the $12 \leq A \leq 26$ mass region quite feasible.

CHAPTER 10

CONCLUSION

Two different proton scattering experiments have been performed to study low energy vibrational excitations. Although the two experiments both involve proton scattering, the techniques used and the information obtained is very different for the two.

A 3_2^- state at 2423.4(4) keV was rigorously identified in the even-even Pt isotope ^{196}Pt . The state was populated via a $^{196}\text{Pt}(p, p'\gamma)$ proton- γ coincidence experiment with a 12.7 MeV proton beam at Florida State University. The spin assignment is based on previous analysis of (p, p') angular distributions [Cot88b], which limit the allowed spins to $J^\pi = 3^-, 4^+$, and previous observation of the 2423.4 keV state in $(n, n'\gamma)$ [DiP93], which excludes the $J^\pi = 4^+$ assignment. We therefore assign a spin of $J^\pi = 3^-$ to the 2423.4 keV state, confirming a previous assignment by Ponomarev *et al.* [Pon92]. The observation of a γ -ray decay of 976.7(3) keV to the lowest-lying 3^- state at 1447.0(2) keV confirms the placement of the level.

Observation of a higher-lying 3^- state considerably strengthens the argument made in Reference [Cot88b] for fragmentation of the low energy octupole state in ^{196}Pt . Three additional states, not observed in the present experiment, have nearly identical proton angular distributions, and it is likely that they, too, have $J^\pi = 3^-$ and are additional fragments of the low energy octupole state [Cot88b]. Ponomarev *et al.* has already assigned $J^\pi = 3^-$ to two of these states [Pon92]. Furthermore, a similar analysis of proton angular distributions from $^{194,198}\text{Pt}$ [Cot88b] shows a number of states in the two isotopes with nearly identical distributions to the 2423.4 keV state in ^{196}Pt . It is likely that the octupole state is fragmented in these nuclei,

also. Transition strengths on the order of 6 – 9 W.u. indicate a moderate degree of collectivity in these states, identifying them as collective octupole vibrations. ^{196}Pt is one of the best known examples of an $O(6)$ symmetry nucleus [Ciz78] in the IBM formalism, in which the apparent octupole fragmentation is understood. Similar $^{194,198}\text{Pt}(p, p'\gamma)$ experiments are needed to identify octupole fragmentation in the other even-even Pt isotopes.

Proton scattering is used for the first time to excite the 2_1^+ state in the neutron rich ^{20}O nucleus. In this experiment, however, the proton scattering is performed in inverse kinematics from the radioactive beam ^{20}O at the NSCL at MSU. The RMS quadrupole deformation parameter, β_2 , of the 2_1^+ excitation at 1.674 MeV is extracted with a coupled channels analysis of the measured elastic and inelastic scattered proton angular distributions. Used in combination with the reduced transition probability $B(E2)$ taken from the known γ -ray lifetime [Ram87], the ratio of neutron to proton multipole matrix elements is determined as $M_n/M_p = 2.8 \pm 0.4$.

The result is significantly larger than the isoscalar estimate of $M_n/M_p = N/Z = 1.5$ for ^{20}O , indicating a substantially larger neutron contribution relative to the proton contribution in the $0_{gs}^+ \rightarrow 2_1^+$ transition. An enhanced neutron contribution is consistent with a simple shell model picture where the four valence neutrons outside of a closed shell core ($N = 8$ and $Z = 8$) dominate the excitation. A similar enhanced neutron contribution was observed in ^{18}O [Pet93], which has the same $Z = 8$ closed proton shell. Additional measurements of other singly closed shell nuclei in the $12 \leq A \leq 26$ mass region would allow a systematic determination of the behavior of M_n/M_p for $0_{gs}^+ \rightarrow 2_1^+$ transitions near the neutron and proton drip lines. Systematic studies would also lend insight into the discrepancies observed between pion scattering and nucleon scattering results in this mass region.

BIBLIOGRAPHY

- [Ald56] K. Alder, A. Bohr, T. Huus, B. Mottelson, A. Winther, *Rev. Mod. Phys.* **28**, 432 (1956).
- [Ann95] R. Anne, D. Bazin, R. Bimbot, M.J.G. Borge, J.M. Corre, S. Dogny, S. Emling, D. Guillemaud-Mueller, P.G. Hansen, P. Hornshj, P. Jensen. B. Johnson, M. Lewitowicz, A.C. Mueller, R. Neugart, T. Nilsson, G. Nyman, F. Pougheon, M.G. Saint-Laurent, G. Schreider, O. Sorlin, O. Tengblad. K. Wilhelmsen-Rolander, *Z. Phys.* **A352**, 397 (1995).
- [Ari75] A. Arima, F. Iachello, *Phys. Rev. Lett.* **35**, 1069 (1975).
- [Ari76] A. Arima, F. Iachello, *Ann. Phys.* **99**, 253 (1976).
- [Ari78] A. Arima, F. Iachello, *Ann. Phys.* **111**, 201 (1978).
- [Ari79] A. Arima, F. Iachello, *Ann. Phys.* **123**, 468 (1979).
- [Bal47] G.C. Baldwin, G.S. Klaiber, *Phys. Rev.* **71**, 3 (1947).
- [Bal48] G.C. Baldwin, G.S. Klaiber, *Phys. Rev.* **73**, 1156 (1948).
- [Bar88] A.F. Barfield, B.R. Barrett, J.L. Wood, O. Scholten, *Ann. Phys.* **182**, 344 (1988).
- [Bec69] F.D. Becchetti, Jr., G.W. Greenlees, *Phys. Rev.* **182**, 1190 (1969).
- [Ber69] A.M. Bernstein, in *Advances in Nuclear Physics*, M. Baranger, E. Vogt, ed., Vol. 3, Plenum, New York (1969).

- [Ber75] Z. Berant, C. Broude, G. Engler, M. Hass, R. Levy, B. Richter, Nucl. Phys. **A243**, 519 (1975).
- [Ber79] A.M. Bernstein, V.R. Brown, V.A. Madsen, Phys. Rev. Lett. **42**, 425 (1979).
- [Ber81] A.M. Bernstein, V.R. Brown, V.A. Madsen, Phys. Lett. **103B**, 255 (1981).
- [Ber83] A.M. Bernstein, V.R. Brown, V.A. Madsen, Comments Nucl. Part. Phys. **11**, 203 (1983).
- [Bla79] J.M. Blatt, V.F. Weisskopf, *Theoretical Nuclear Physics*, Springer-Verlag, New York (1979).
- [Boh39] N. Bohr, J.A. Wheeler, Phys. Rev. **56**, 426 (1939).
- [Boh52] A. Bohr, Kgl. Dan. Mat. Fys. Medd. **26** no. 14 (1952).
- [Boh53] A. Bohr, B.R. Mottelson, K. Danske Vidensk. Selsk. Mat.-Fys. Medd. **27** no. 16 (1953).
- [Boh69] A. Bohr, B.R. Mottelson, **Nuclear Structure, Vol. I**, W.A. Benjamin, Inc., Reading, Massachusetts (1969).
- [Boh75] A. Bohr, B.R. Mottelson, **Nuclear Structure, Vol. II**, W.A. Benjamin, Inc., Reading, Massachusetts (1975).
- [Bol81] H.H. Bolotin, A.E. Stuchbery, I. Morrison, D. L. Kennedy, C.G. Ryan, S.H. Sie, Nuc. Phys. **A370**, 146 (1981).
- [Bro59] G.E. Brown, M. Bosterli, Phys. Rev. Lett. **10**, 472 (1959).
- [Bro80] B.A. Brown, B.H. Wildenthal, Phys. Rev. **C21**, 2107 (1980).
- [Bro80b] B.A. Brown, W. Chung, B.H. Wildenthal, Phys. Rev. **C21**, 2600 (1980).

- [Bro82] B.A. Brown, B.H. Wildenthal, W. Chung, S.E. Massen, M. Bernas, A.M. Bernstein, R. Miskimen, V.R. Brown, V.A. Madsen, Phys. Rev. **C26**, 2247 (1982).
- [Bro75] V.R. Brown, V.A. Madsen, Phys. Rev. **C11**, 1298 (1975).
- [Bro61] G.E. Brown, L. Castillejo, J.A. Evans, Nucl. Phys. **22**, 1 (1961).
- [But96] P.A. Butler, W. Nazarewicz, Rev. Mod. Phys. **68**, 349 (1996).
- [Car85a] J.A. Carr, F. Petrovich, R.J. Philpott, M.J. Threapleton, O. Scholten, H. McManus, Phys. Rev. Lett. **54**, 881 (1985).
- [Car85b] J.A. Carr, F. Petrovich, J.J. Kelly, in *Neutron-Nucleus Collisions: A Probe of Nuclear Structure*, AIP Conf. Proc. No. 124, ed. J.Rapaport, R.W.Finlay, S.M.Grimes, and F.S.Dietrich, AIP, New York (1985).
- [Cas78] R.F. Casten, J.A. Cizewski, Nuc. Phys. **A309**, 477 (1978).
- [Cas81] R.F. Casten, D.D. Warner, D.S. Brenner, R.L. Gill, Phys.Rev. Lett. **47**, 1433 (1981).
- [Cas85] R.F. Casten, P. von Brentano, Phys. Lett. **152**, 22 (1985).
- [Ciz78] J.A. Cizewski, R.F. Casten, G.J. Smith, M.L. Stelts, W.R. Krane, H.G. Borner, W.F. Davidson, Phys. Rev. Lett. **40**, 167 (1978).
- [Comf] J.R. Comfort, University of Pittsburgh report (unpublished).
- [Cot88a] P.D. Cottle, V. Huizdo, R.J. Philpott, K.A. Stuckey, K.W. Kemper, Phys. Rev. **C38**, 1619 (1988).
- [Cot88b] P.D. Cottle, K.A. Stuckey, K.W. Kemper, Phys. Rev. **C38**, 2843 (1988).
- [Cot90] P.D. Cottle, M.A. Kennedy, K.A. Stuckey, Phys. Rev. **C42**, 2005 (1990).

- [Cot96] P.D. Cottle, N.V. Zamfir, Phys. Rev. **C54**, 176 (1996).
- [Dan51] M. Danos, H. Steinwedel, Z. Naturforsch **6a**, 23 (1951).
- [Dan58] M. Danos, Nucl. Phys. **5**, 23 (1958).
- [Dea81] P.T. Deason, C.H. King, R.M. Ronningen, T.L. Khoo, F.M. Bernthal, J.A. Nolen, Jr., Phys. Rev. **C23**, 1414 (1981).
- [DeL83] R. De Leo G. D'Erasmus, A. Pantaleo, M.N. Harakeh, E. Cereda, S. Micheletti, M. Pignatelli, Phys. Rev. **28**, 1443 (1983).
- [deS74] R. de Swiniarski, A. Genoux-Lubain, G. Bagieu, J.F. Cavaignac. Can. J. Phys. **52**, 2422 (1974).
- [DiP93] D.P. DiPrete, T. Belgya, E.M. Baum, E.L. Johnson, S.W. Yates, P.D. Cottle, M.A. Kennedy, K.A. Stuckey, Phys. Rev. **C48**, 2603 (1993).
- [Dja85] C. Djalali, N. Marty, M. Morlet, A. Willis, J.C. Jourdain, D. Bohle, U. Hartmann, G. Kuchler, A. Richter, G. Caskey, G.M. Crawley, A. Galonsky, Phys. Lett. **B164**, 269 (1985).
- [Egi96] J.L. Egidio, V. Martin, L. Robledo, Y. Sun, Phys. Rev. **C53**, 2855 (1996).
- [Ell80] J.P. Elliott, A.P. White, Phys. Lett. **B97**, 169 (1980).
- [Eng86] J. Engel, Phys. Lett. **B171**, 148 (1986).
- [Fa:diss] M. Fauerbach, Ph.D. Dissertation, Michigan State University (1997).
- [Fee49] E. Feenberg, Phys. Rev. **75**, 320 (1949).
- [Flu41] S. Flügge, Ann. Phys. **39**, 373 (1941).
- [Fox89] R. Fox, R. Au and A. VanderMolen, IEEE Trans. Nucl. Sci., 1562 (1989).

- [Gam29] G. Gamow, Roy. Soc. Proc. **A123**, 386 (1929).
- [Gei95] H. Geissel, G. Münzenberg, K. Riisager, Ann. Rev. Nucl. Part. Sci., **45**, 163 (1995).
- [Gol48] M. Goldhaber, E. Teller, Phys. Rev. **74**, 1046 (1948).
- [Gor49] W. Gordy, Phys. Rev. **76**, 139 (1949).
- [Gra80] P. Grabmayr, J. Rapaport, R.W. Finlay, Nucl. Phys. **A350**, 167 (1980).
- [Hah96] K.I. Hahn, A. Garcia, E.G. Adelberger, P.V. Magnus, A.D. Bacher. N. Bateman, G.P.A. Berg, J.C. Blackmon, A.E. Champagne, B. Davis, A.J. Howard, J. Liu, B. Lund, Z.Q. Mao, D.M. Markoff, P.D. Parker, M.S. Smith, E.J. Stephenson, K.B. Swartz, S. Utku, R.B. Volegaar, K. Yildiz, Phys. Rev. **C54**, 1999 (1996).
- [Has83] D.K. Hassell, N.E. Davison, T.N. Nasr, B.T. Murdoch, A.M. Sourkes, W.T.H. van Oers, Phys. Rev. **C27**, 482 (1983).
- [Hax49] O. Haxel, J.H.D. Jensen, H.E. Suess, Phys. Rev. **75**, 1766 (1949).
- [Hei32] W. Heisenberg, Z. Phys. **77**, 1 (1932).
- [Hen68] W. Henning, Z. Phys. **217**, 438 (1968).
- [Her77] J.A.J. Hermans, G.A.P. Engelbertink, L.P. Ekstrom, H.H. Eggenhuisen, M.A. Van Driel, Nucl. Phys. **A284**, 307 (1977).
- [Iac74] F. Iachello, A. Arima, Phys. Lett. **53B**, 309 (1974).
- [Iac84] F. Iachello, Phys. Rev. Lett. **53**, 1427 (1984).
- [Jen52] J.H.D. Jensen, M.G. Mayer, Phys. Rev. **85**, 1040 (1952).

- [Kel97] J.H. Kelley, T Suomijärvi, S.E. Hirzebruch, A. Azhari, D. Bazin, Y. Blumenfeld, J.A. Brown, P.D. Cottle, S. Danczyk, M. Fauerbach, T. Glasmacher, J.K. Jewell, K.W. Kemper, F. Maréchal, D.J. Morrissey, S. Ottini, J.A. Scarpaci, P. Thirolf, submitted to Phys. Rev Lett. (1997).
- [Ken56] H. Kendall, L. Grodzius, Bull. Am. Phys. Soc. **1**, (1956).
- [Ken92] M.A. Kennedy, P.D. Cottle, K.W. Kemper, Phys. Rev. **C46**, 1811 (1992).
- [Kha84] A. Khan, S.W. Yates, Phys. Rev. **C29**, 1081 (1984).
- [Kno79] G.F. Knoll, Radiation Detection and Measurement, John Wiley and Sons, New York (1979).
- [Kra94] G. Kraus, P. Egelhof, C. Fischer, H. Geissel, A. Himmler, F. Nickel, G. Münzenberg, W. Schwab, A. Weiss, J. Friese, A. Gillitzer, H.J. Körner, M. Peter, W.F. Henning, J.P. Schiffer, J.V. Kratz, L. Chulkov, M. Golovkov, A. Ogloblin, B.A. Brown, Phys. Rev. Lett. **73**, 1773 (1994).
- [Kunz] P.D. Kunz, University of Colorado report (unpublished).
- [Mad75] V.A. Madsen, V.R. Brown, J.D. Anderson, Phys. Rev. **C12**, 1205 (1975).
- [Mad77] V.A. Madssen, Phys. Lett. **B71**, 48 (1977).
- [Mad84] V.A. Madsen, V.R. Brown, Phys. Rev. Lett. **52**, 176 (1984).
- [May48] M.G. Mayer, Phys. Rev. **74**, 235 (1948).
- [May49] M.G. Mayer, Phys. Rev. **75**, 1969 (1949).
- [May50] M.G. Mayer, Phys. Rev. **78**, 22 (1950).
- [May55] M.G. Mayer, J.H.D. Jensen, *Elementary Theory of Nuclear Shell Structure*, Wiley, New York (1955).

- [McD76] A.B. McDonald, T.K. Alexander, C. Broude, J.S. Forster, O. Häuser, F.C. Khanna, I.V. Mitchell, Nucl. Phys. **A258**, 152 (1976).
- [Mor87] C.L. Morris, S.J. Seestrom-Morris, D. Dehnhard, C.L. Blilie, R. Gilman, G.P. Gilfoyle, J.D. Zumbro, M.G. Burlein, S. Mordechai, H.T. Fortune, L.C. Bland, M. Brown, D.P. Saunders, P.A. Seidl, C. Fred Moore, K. Maeda, G.S. Blanpied, B.A. Brown, Phys. Rev. **C35**, 1388 (1987).
- [Mot95] T. Motobayashi, Y. Ikeda, Y. Ando, K. Ieki, M. Inoue, N. Iwasa, T. Kikuchi, M. Kurokawa, S. Moriya, S. Ogawa, H. Murakami, S. Shimoura, Y. Yanagisawa, T. Nakamura, Y. Watanabe, M. Ishihara, T. Teranishi, H. Okuno, R.F. Casten, Phys. Lett. **B346**, 9 (1995).
- [Mue93] A.C. Mueller, B.M. Sherrill, Ann. Rev. Nucl. Part. Sci., **43**, 529 (1993).
- [Nat56] O. Nathan, M.A. Waggoner, Nucl. Phys. **2**, 548 (1956).
- [Nee70] K. Neergard, P. Vogel, Nucl. Phys. **A145**, 33 (1970).
- [Nil55] S.G. Nilsson, Kgl. Danske Videnskab. Selskab Mat. Fys. Medd., **29**, (1955).
- [Nor49] L.W. Nordheim, Phys. Rev. **75**, 1894 (1949).
- [Oka58] K. Okamoto, Phys. Rev. **110**, 143 (1958).
- [Ols89] N. Olsson, B. Trostell, E. Ramström, Nucl. Phys. **A496**, 505 (1989).
- [Ols90] N. Olsson, E. Ramström, B. Trostell, Nucl. Phys. **A513**, 205 (1990).
- [Ost79] F. Osterfeld, J. Wambach, H. Lenske, J. Speth, Nucl. Phys. **A318**, 45 (1979).
- [Pet86] F. Petrovich, J.A. Carr, H. Mcmanus, Ann. Rev. Nucl. Sci. **36**, 29 (1986).
- [Pet93] R.J. Peterson, Phys. Rev. **C48**, 1128 (1993).

- [Pon92] V.Yu. Ponomarev, W.T.A. Borghols, S.A. Fayans, M.N. Harakeh, C.W. de Jager, J.B. van der Laan, A.P. Platonov, H. de Vries, S.Y. van der Werf, *Nuc. Phys* **A549**, 180 (1992).
- [Rai50] J. Rainwater, *Phys. Rev.* **79**, 432 (1950).
- [Ram87] S. Raman, C.H. Malarkey, W.T. Milner, C.W. Nestor, Jr., P.H. Stelson, *Atomic Data and Nuclear Data Tables* **36**, 1 (1987).
- [Ril:diss] L.A. Riley, Ph.D. dissertation, Florida State University (1997).
- [Ron77] R.M. Ronningen, R. B. Piercy, A.V. Ramayya, J.H. Hamilton, S. Raman, P.H. Stelson, W.K. Dagenhart, *Phys. Rev.* **C16**, 571 (1977).
- [Rut80] A.J. Rutten, A. Holthuisen, J.A.G. De Raedt, W.A. Sterrenburg, G. Van Middelkoop, *Nucl. Phys.* **A344**, 294 (1980).
- [Sat64] G.D. Satchler, R.M. Drisko, R.H. Bassel, *Phys. Rev.* **136B**, 637 (1964).
- [Sat83] G.R. Satchler, *Direct Nuclear Reactions*, Oxford University Press, New York (1983).
- [Sch55] G. Scharff-Goldhaber, J. Weneser, *Phys. Rev.* **98**, 212 (1948).
- [Sch96] H. Scheit, T. Glasmacher, B.A. Brown, J.A. Brown, P.D. Cottle, P.G. Hansen, R. Harkewicz, M. Hellstrom, R.W. Ibbotson, J.K. Jewell, K.W. Kemper, D.J. Morrissey, M. Steiner, P. Thirolf, M. Thoennessen, *Phys. Rev. Lett.* **77**, 3967 (1996).
- [Set90] A. Sethi, F.T. Baker, G.T. Emery, W.P. Jones, M.A. Grimm, Jr., *Nuc. Phys.* **A518**, 536 (1990).
- [Set91] A. Sethi, N.M. Hintz, D.N. Mihailidis, A.M. Mack, M. Gazzaly, K.W. Jones, G. Pauletta, L. Santi, D. Goutte, *Phys. Rev.* **C44**, 700 (1991).

- [She91] B.M. Sherrill, D.J. Morrissey, J.A. Nolen Jr., N. Orr, J.A. Winger, Nucl. Inst. Meth. **B56/57**, 1106 (1991).
- [Spe88] R.H. Spear, At. Data Nucl. Data Tables, **42**, 55 (1988).
- [Ste50] H. Steinwendel, J.H.D. Jensen, Z. Naturforsch. **5a**, 413 (1950).
- [Ste54] F. Stephens, Jr., F. Asaro, I. Perlman, Phys. Rev. **96**, 1568 (1954).
- [Swa94] D. Swan, J. Yurkon, D.J. Morrissey, Nucl. Inst. Meth. **A348**, 314 (1994).
- [Tab93] S.L. Tabor, M.A. Riley, J. Döring, P.D. Cottle, T. Glasmacher, J.W. Holcomb, J. Hutchins, G.D. Johns, T.D. Johnson, T. Petters, O. Tekyi-Mensah, P.C. Womble, L. Wright, J.X. Saladin, Nucl. Instrum. Methods **B79**, 821 (1993).
- [Til95] D.R. Tilley, H.R. Weller, C.M. Cheves, R.M. Chasteler, Nucl. Phys. **A595**, 1 (1995).
- [Tow49] C.H. Townes, H.M. Foley, W. Low, Phys. Rev. **76**, 1415 (1949).
- [vonBre96] P. von Brentano, J. Eberth, J. Enders, L. Esser, R.D. Herzberg, N. Huxel, H. Meise, P. von Neumann-Cosel, N. Nicolay, N. Pietralla, H. Prade, J. Reif, A. Richter, C. Schlegel, R. Schwengner, S. Skoda, H.G. Thomas, I. Wiedenhöver, G. Winter, A. Zilges, Phys. Rev. Lett. **76**, 2029 (1996).
- [Wam79] J. Wambach, F. Osterfeld, J. Speth, V.A. Madsen, Nucl. Phys. **A324**, 77 (1979).
- [War82] D.D. Warner, R.F. Casten, Phys. Rev. Lett. **48**, 1385 (1982).
- [War83] D.D. Warner, R.F. Casten, Phys. Rev. **C28**, 1798 (1983).
- [Wei35] C.F. von Weizsäcker, Z. Phys. **96**, 461 (1935).

- [Win92] J.A. Winger, B.M. Sherill, D.J. Morrissey, Nucl. Instr. Meth. **B70**, 380 (1992).
- [Yat83] S.W. Yates, A. Khan, A.J. Filo, M.C. Mirzaa, J.L. Weil, M.T. McEllistrem, Nuc. Phys. **A406**, 519 (1983).
- [Yat88] S.W. Yates, R. Julin, J. Kumpulainen, E. Verho, Phys. Rev. **C37**, 2877 (1988).
- [Zam93a] N.V. Zamfir, R.F. Casten, Phys. Lett. **B305**, 317 (1993).
- [Zam93b] N.V. Zamfir, P.D. Cottle, J.L. Johnson, R.F. Casten, Phys. Rev. **C48**, 1745 (1993).
- [Zuc68] A.P. Zucker, B. Buck, J.B. McGroary, Phys. Rev. **C21**, 39 (1968).
- [Zwi83] B. Zwięgliński, G.M. Crawley, J.A. Nolen, Jr., R.M. Ronningen, Phys. Rev. **C28**, 542 (1983).

BIOGRAPHICAL SKETCH

The author was born on July 23, 1970 in Northeast Ohio. He graduated with honors from Kent State University in 1992 with a B.S. in Physics. The author began his graduate studies at Florida State University in the Fall of 1992, fulfilling the requirements for a Ph.D. in Nuclear Physics in the Fall of 1997. He will begin work immediately at the Idaho Falls National Engineering and Environmental Laboratory in Idaho Falls, Idaho.